

9<sup>th</sup> International Conference on

# ADVANCED VIBRATIONAL SPECTROSCOPY

I C A V S 9



## Victoria, BC

June 11 – 16, 2017

Victoria Conference Centre



@icavs9 / #icavs9



[www.icavs.org](http://www.icavs.org)



Thursday June 15 2017

Poster Session 3

## **Elucidation of the Chemical Composition of Ancient Adhesives present in Lithic Artefacts by Means of FTIR Spectroscopy**

C. Araujo-Andrade<sup>1</sup>, M. Marro<sup>1</sup>, Andreu Ollé<sup>2,3</sup>, Lena Asryan<sup>2,3</sup>, Behrouz Bazgir<sup>2,3</sup>, Juan Luis Fernández-Marchena<sup>2,3</sup>, Antonella Pedernana<sup>2,3</sup>, Laxmi Tumung<sup>2,3</sup>, P. Loza-Alvarez<sup>1,\*</sup>

<sup>1</sup> *ICFO-Institut de Ciències Fòniques, The Barcelona Institute of Science and Technology, Castelldefels (Barcelona), 08902 Spain.*

<sup>2</sup> *IPHES, Institut Català de Paleoecologia Humana i Evolució Social, Zona educacional 4 (Edifici W3), Campus Sescelades URV, 43007 Tarragona, Spain / Àrea de Prehistòria, Universitat Rovira i Virgili, Fac. de Lletres, Av. Catalunya 35, 43002 Tarragona, Spain*  
<sup>3</sup> *Àrea de Prehistòria, Universitat Rovira i Virgili, Fac. de Lletres, Av. Catalunya 35, 43002 Tarragona, Spain / IPHES, Institut Català de Paleoecologia Humana i Evolució Social, Zona educacional 4 (Edifici W3), Campus Sescelades URV, 43007 Tarragona, Spain.*

\**Pablo.loza@icfo.eu*

Though the debate continues regarding whether the organic material on ancient lithic artefacts can survive and be microscopically identified, the study of residues is in fact already one of the key components of functional analysis. Indeed, the study of different kind of organic residues (e.g. bone, wood, plants, blood cells, starch granules etc.) on the archaeological lithic artefacts is currently being carried out by many authors.

Here we focus on a particular type of residue, the “black spots” observed in some archaeological lithic artefacts from different sites (e.g. Umm El Tel and Hummal in Syria, Campitello in Italy, les Vachons in France, Königsau and Inden-Altdorf in Germany, Diepkloof Rock Shelter in south Africa, some sites in the Yukon Territory, Canada, etc.) and interpreted most commonly by researchers as being residues of bitumen, tar or bark birch pitch, pine or other plants resin, used for hafting the lithic artefacts [1,2]. The most commonly employed methods for identification of these residues have been through use of optical and scanning electron microscopy to determine morphological features, and energy dispersive spectrometry (EDX) and the chromatography-mass spectrometry (GC-MS) for identification of chemical composition. However, all these techniques are considered as destructive and cannot provide information of the molecular composition and structure of the sample.

On the other side, vibrational spectroscopies such as FTIR allow to obtain the molecular identity of materials in a reliable, reagent free and non-destructive way. Here we present the results obtained of the spectroscopic characterization of diverse organic residues (black spots) present on some lithic artefacts apparently related to projectile hafting. Samples were obtained from different Palaeolithic sites such as; Azokh Cave, in Nagorno Karabagh, Gilvaran and Kaldar, in Iran, and Cova Eirós, in Spain.

Residues considered here are brownish black stains that appear as isolated drops of dried liquid material that can have the appearance of cracks on their surface. The residues occur on both faces, in many cases (but not all) distributed around those parts of the tool which were likely grasped or hafted. Although most of the hafting adhesives that are published, appear more conspicuous residues, their distribution on the artefacts suggest hafting residues.

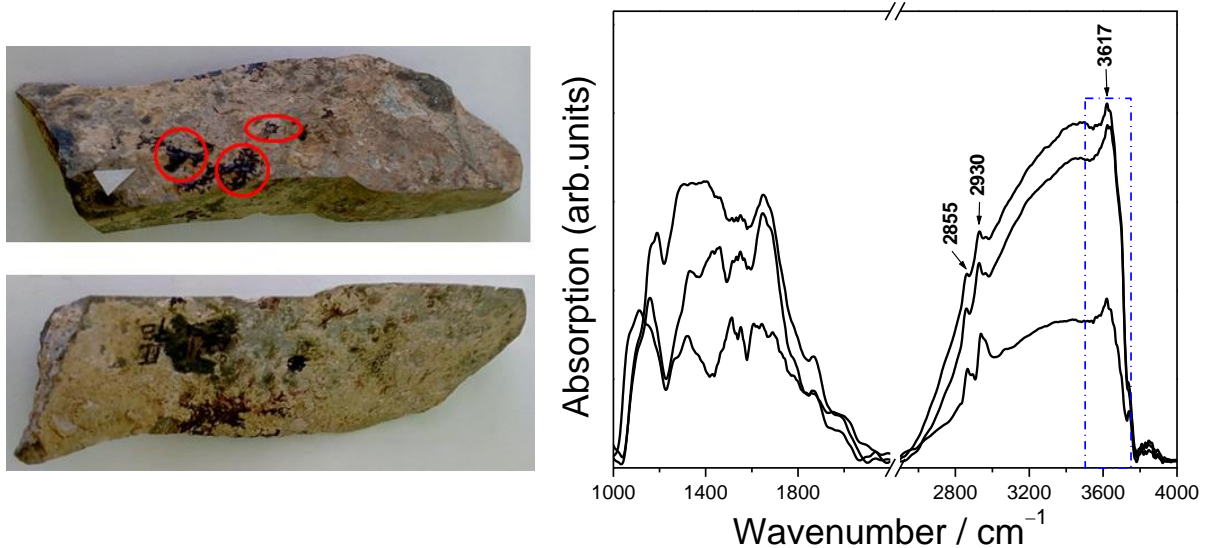


**Figure 1.** (Left) Sample obtained from Kaldar cave which is situated in the north of Khorramabad Valley, western Iran. Red circles show the zones with “black spots” analyzed by FTIR. (Right) Representative spectra recorded of each “black spot” showed in the red circles.

Results obtained of the analysis of the FTIR spectra recorded from the lithic artefacts here studied, suggest that one of the major components of the “black spots” is of bituminous origin, showing spectral signatures similar to lignite [3]. According with the reported in the literature, the band located at *ca.* 3617  $\text{cm}^{-1}$ , ascribed to stretching mode of free OH, it is a distinctive band of these organic substances [3].

[1] Boëda, É., Connan, J., Ressort, D., Muhesen, S., Mercier, N., Valladas, H. & Tisnérat, N. Bitumen as a hafting material on Middle Palaeolithic artefacts. *Nature*. **1996**, 380, 336-338.

[2] Cârciumar, M., Ion, R.-M., Nitu, E.-C. & Stefanescu, R. *J. Archaeol. Sci.* **2012**, 39, 1942–1950.

[3] Weiqing Zhang , Shuguang Jiang , Kai Wang , Lanyun Wang , Yongliang Xu , Zhengyan Wu , Hao Shao , Yunhang Wang & Menglu Miao, *Int. J. Coal. Prep. Util.* **2015**, 35, 39–50.

## **Infrared Orange: a new powerful tool for hyperspectral data analysis.**

Marko Toplak<sup>1</sup>, Giovanni Birarda<sup>2,\*</sup>, Ferenc Borondics<sup>3</sup>, Christophe Sandt<sup>3</sup>, Lisa Vaccari<sup>2</sup>, Janez Demsar<sup>1\*</sup>

<sup>1</sup> *Faculty of Computer and Information Science University of Ljubljana, Vecna pot 113, SI-1000 Ljubljana, Slovenia*

<sup>2</sup> *Elettra Sincrotrone Trieste, S.S. 14 Km 163.5 34149 Trieste, Italy*

<sup>3</sup> *Synchrotron SOLEIL, L'Orme des Merisiers, BP48 Saint Aubin, 91192 Gif-sur-Yvette Cedex, France*

*\*[giovanni.birarda@elettra.eu](mailto:giovanni.birarda@elettra.eu) and [janez.demsar@fri.uni-lj.si](mailto:janez.demsar@fri.uni-lj.si)*

Multitechnique approaches in science can provide a broader and better understanding of research questions. Today, spectroscopic techniques such as infrared spectroscopy and spectromicroscopy are widely used by a great variety of scientists from diverse backgrounds. Unfortunately, hyperspectral data handling workflows can involve multiple steps, usually requiring the use of several software environments. From data acquisition through data analysis to data representation the steps include the use of proprietary codes not commonly available to everyone due to license fees. Although spectroscopy experts often develop their own processing algorithms, there are multitudes of compatibility and usability issues that hinder the transferability of the code to other users with no or little programming experience.

To answer to the vibrational spectroscopy community's need of a common, open-source, user-friendly yet powerful platform for data analysis we developed Infrared Orange: an add-on for analysis of FTIR spectroscopy and hyperspectral data sets.[1] The package is based on the Orange Canvas,[2] a user-friendly platform for data analysis and machine learning through visual programming in which the user constructs a data processing workflow.[3]

Infrared Orange can be used by both advanced users that can carry out more rapidly their analyses, and eventually implement it by coding their own procedures into widgets, or by casual users, that can have a visual and easy way to perform the analysis of their data. At its current stage, the package can import spectral data into the Orange canvas, which already contains a number of data-analytic methods. We have added functions for spectral-specific basic preprocessing, such as baseline correction, normalization, derivation, integration, etc. (Figure 1) As well as importing, visualization and analysis of hyperspectral data cubes and advanced machine learning analyses and classifiers, like clustering, regression, principal component analysis, etc.

Since the software is open-source, anyone can contribute to its development and implement additional functions. By starting this project, we wanted to provide a solid base on which more and more users can build upon. Although our initial goal is vibrational spectroscopy, the software can be easily utilized for other (hyper)spectral techniques. We hope that in the future our tool will grow and surpass these boundaries, becoming used by other spectroscopic and imaging techniques, constituting a bridge and a common interchange platform between different analytical methods.



**Figure 1.** : Example of a simple Infrared Orange workflow showing the building blocks (widgets) of the processing scheme and a plot for spectral data.

#### REFERENCES:

- [1] <https://github.com/markotoplak/orange-infrared>
- [2] <http://orange.biolab.si>
- [3] J. Demšar *et al.*, “Orange: Data Mining Toolbox in Python,” *J. Mach. Learn. Res.*, vol. 14, no. 1, pp. 2349–2353, Jan. 2013.

## **Online Raman Measurement of Polymer Changeover Time In a Twin-Screw Extruder**

Jin Wang, Christopher Thurber, Xiaoyun Chen, Michael Read, Nicholas Horstman, Calvin Pavlicek, Jamie Stanley, and Michael Bishop\*

*The Dow Chemical Company, Midland MI, USA, 48667*

*\*[mmbishop@dow.com](mailto:mmbishop@dow.com)*

Reliable knowledge of the changeover time between polymer feeds with different physical and processing properties in twin-screw extruders is important for transient operations in the polymer-processing industry. In this work, we examine the changeover kinetics of polyethylene and polystyrene in a twin-screw extruder using an online Raman spectroscopy system and a classical least-squares analysis method. This Raman method was able to display changeover kinetics in real-time, and subsequent fitting of these data with a simple kinetic model was used to extract changeover times. The changeover times were measured to be generally longer than the residence times, where the residence times were measured using analogous “pulsed” tracer experiments. The viscosity ratio between the ending and starting materials and the throughput were found to have a significant effect on changeover time, whereas screw speed did not.

# Deep Ultra-Violet Raman Spectroscopy for Eyesafe Standoff Chemical Threat Detection

Justin T. Cooper<sup>1,\*</sup>, Adam J. Hopkins<sup>2</sup>, Luisa T.M. Profeta<sup>2</sup>, Alan R. Ford<sup>2</sup>

<sup>1</sup>Andor Technology, 300 Baker Avenue, Suite 150, Concord, MA 01742

<sup>2</sup>Alakai Defense Systems, 8285 Bryan Dairy Rd, Ste 125, Seminole, FL 33777

\*j.cooper@andor.com

Under the growing threat of foreign and homegrown terrorism, illegal drug manufacture and environmental contamination, the demand for rapid, portable and most importantly standoff chemical threat (explosives, narcotics, toxic industrial chemicals, etc.) detection capabilities has increased dramatically[1]. While offering excellent limits of detection, traditional analytical laboratory techniques such as high-performance liquid chromatography or gas chromatography coupled with mass spectrometry often lack the portability necessary for remote on-site interrogation. Furthermore, samples must be physically collected by a handler and brought to a laboratory for analysis, putting the user at risk if samples are of a potentially threatening nature. Spectroscopic techniques are inherently standoff, as emitted or scattered photons are collected at some distance from the sample and vibrational spectroscopy such as IR absorption or Raman scattering offer the chemical identification capabilities required.

Alakai Defense Systems, in conjunction with Andor Technologies, has developed a portable standoff chemical threat detection instrument, dubbed as the Portable Raman Improvised Explosive Detector (PRIED). PRIED employs laser based excitation and collection of spontaneous Raman scattering for chemical detection and identification. The PRIED instrument consists of a hand-held wand which contains the excitation laser, guiding laser, IR LIDAR emitter, and focusing and collection optics. The wand is connected via umbilical to a backpack which contains the spectrograph, detector, computer, chiller and power supply. The spectrograph design is based on a fixed-grating Czerny-Turner arrangement similar to the Andor Shamrock 163 shown in figure 1. The detector is an Andor iStar intensified-CCD camera which allows for high rep-rate high time resolution gating that is used for fluorescence rejection.

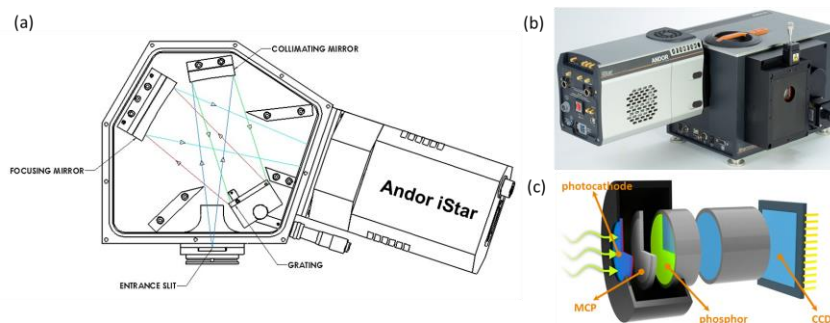


**Figure 1.** (a) Fixed grating Czerny-turner spectrograph (Andor SR-163). (b) Andor iStar ICCD. (c) Internals diagram of intensified-CCD detector.

Standoff detection of Raman scattering has traditionally been a challenge due to the inherently low scattering cross sections exhibited by most compounds. To address this challenge, PRIED incorporates the use of deep ultra-violet excitation (DUV) of a  $\lambda =$

262 nm frequency quadrupled neodymium-doped yttrium lithium fluoride (Nd:YLF) laser, pulsing in the low kHz regime. This is in contrast to currently commercially available hand-held Raman instruments which typically employ either 785 nm or 1064 nm excitation sources. As the Raman scattering cross sections increase with  $1/\lambda^4$ , DUV excitation provides an 80-fold and 272-fold increase in Raman signal over a 785 or 1064 nm instrument respectively. Furthermore, 785 excitation has been shown to be plagued by fluorescent backgrounds which can obstruct the Raman signal[2]. This is particularly relevant to the detection of narcotics as is demonstrated in Figure 2.

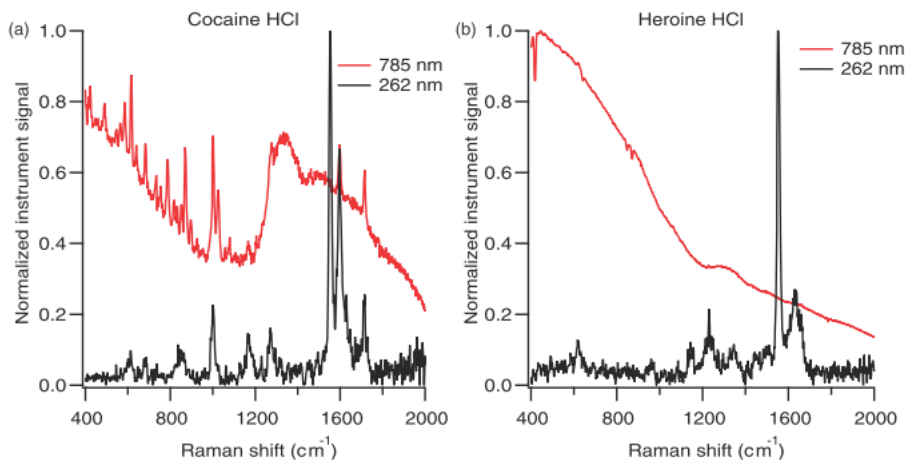


**Figure 2.** Comparison of a commercially available 785 Raman hand-held instrument to PRIED for the detection of (a) cocaine and (b) heroine.

In this work we demonstrate the capabilities of DUV Raman spectroscopy for standoff chemical detection and its incorporation into a novel instrument dubbed PRIED. We discuss the optical design also report on PRIED's ability to detect chemical threats at larger standoff distances (up to 5 m), its ability to detect trace amounts of material as well as resolve constituents in simple mixtures. Furthermore, we find the detection capabilities of PRIED compare favorably or in many cases exceed those of current commercially available hand-held Raman instruments when taking into account the  $>1$  m operational distance of PRIED vs.  $<1$  in. for the commercial instrument. Future directions will include the application of electron -multiplied CCDs which will allow for faster readout times while maintaining high signal-to-noise through the use of EM amplification. We will also test the feasibility of NIR standoff Raman through use of a CCD with deep-depletion technology which extends the QE range of silicon based detectors into the NIR[3].

[1] V. Otieno-Alego, N. Speers. "Counter Terrorism and Homeland Security". In: J.M. Chalmers, H.G.M. Edwards, M.D. Hargreaves (eds) *Infrared and Raman Spectroscopy in Forensic Science*. Chichester, UK: John Wiley & Sons, Ltd, 2012.

[2] Hopkins, A. J.; Cooper, J. T.; Profeta, L. T. M.; Ford, A. B. *Appl. Spec* **2016**, 70, 861-873.

[3] Varagnat, A. "EMCCDs for Spectroscopy", Webinar, <http://www.andor.com/learning-academy/emccds-for-spectroscopy-discover-the-benefits-of-emccd-in-spectroscopy>

## Highly accurate refractive index determination at different wavenumbers using high-resolution FTIR spectroscopy

D. Czurlok<sup>1</sup>, S. Shilov<sup>2</sup>, W. Theiss<sup>3</sup>, M. Joerger<sup>1,\*</sup>

<sup>1</sup>*Bruker Optik GmbH, Rudolf-Plank-Str., 76175 Ettlingen, Germany*

<sup>2</sup>*Bruker Optics Inc., 19 Fortune Drive, Billerica MA 01821, USA*

<sup>3</sup>*W. Theiss Hard- and Software, Dr.-Bernhard-Klein-Str. 110, 52078 Aachen, Germany*

*\*michael.joerger@bruker.com*

The refractive index of IR transparent optical materials is an important parameter for the quality and performance of optical components. Its very accurate determination usually requires complex and expensive ellipsometers.

In this study, we present an alternative approach using conventional FTIR spectroscopy and basing on the evaluation of interference fringes caused by multiple internal reflections in single crystal germanium samples. For highest accuracy, thick samples (up to 10 or even 15mm) were used and thereby high-resolution experiments ( $\leq 0.06\text{cm}^{-1}$  resolution) had to be carried out to resolve the fringe pattern properly. For these challenging spectroscopic measurements, a VERTEX80 FTIR spectrometer with optimized parallel beam and high-resolution option was used (see figure 1). One measured transmission spectrum of a 10 mm Germanium sample is exemplarily shown in figure 2. A comparison of the transmission spectra for different sample thicknesses is shown in figure 3. After the measurements, the evaluation of the fringe patterns were realized fully automatically using a dedicated software model for the material of interest.

With this new approach the refractive index of different plane-parallel germanium samples was determined within an impressive reproducibility of 0.02% at six different representative positions within the mid-infrared spectral range.

Thereby, the new method basing on conventional FTIR spectroscopy can in principle be applied to many other IR transparent materials in future projects.



**Figure 1.** VERTEX80 spectrometer (left) and parallel beam unit (middle), that was used for investigations of the multiple internal reflection fringe pattern in plane-parallel Germanium samples. Beampath of the unit (right) is also illustrated.

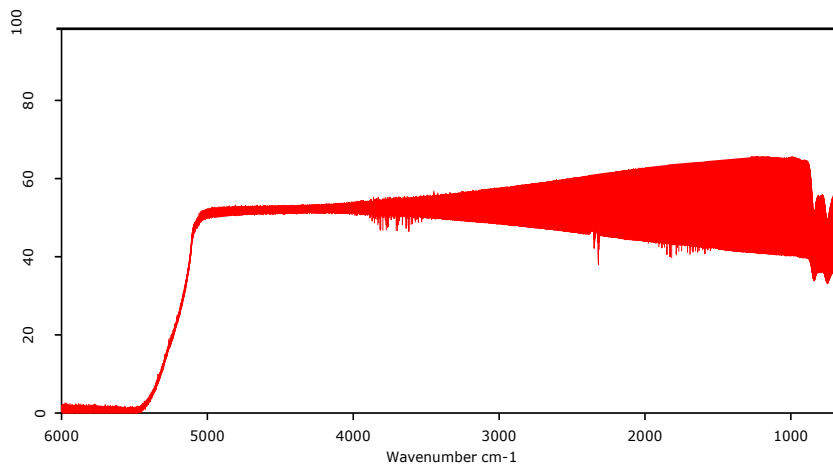


**Figure 2.** Mid-Infrared transmission spectrum of a 10 mm plane-parallel Germanium sample. A strong fringe pattern is visible due to multiple internal reflections.

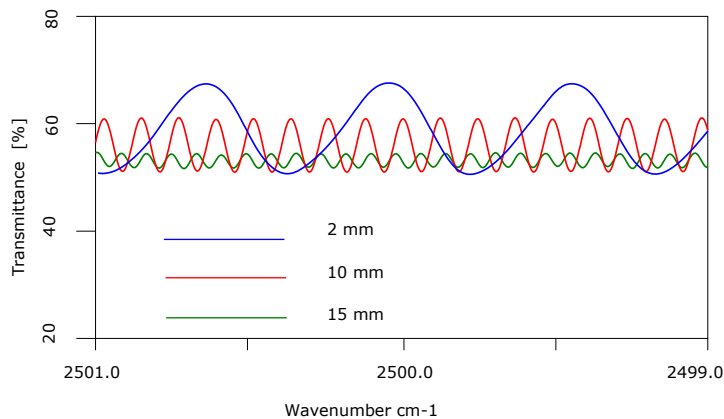


**Figure 3.** Comparison of the fringe pattern of Germanium samples with different thicknesses at a wavelength of 4  $\mu\text{m}$ . Note the resolution that is needed to resolve the fringe pattern, especially in case of thicker samples.

## Quantification of soil quality parameters using vis-NIR spectroscopy and random forest

Santana F. B<sup>1\*</sup>, Souza A. M<sup>2</sup>, Poppi R. J<sup>1</sup>

<sup>1</sup>*Institute of Chemistry, University of Campinas (UNICAMP), P.O. Box 6154, 13084-971  
Campinas, SP, Brazil.*

<sup>2</sup>*Brazilian Agricultural Research Corporation (Embrapa Soils), 22460-000, Rio de  
Janeiro – RJ – Brazil.*

*\*felipebachion@gmail.com*

Most of the native Brazilian soils present limitations for use in agriculture due to their high acidity and low content of organic matter, impacting the development of systems required for efficient production of crops. To increase the productivity and carry out maintenance on the soil, several quality parameters are determined as: cation exchange capacity (CEC), sum of exchange bases (SB), sand, clay and organic matter. Since organic matter is one of the main indicators of soil fertility, in conjunction to the values of sand and clay is used to define the soil texture and in conjunction to the values of CEC and SB is used to calculate the liming recommended for soil acidity correction.

Current methods for evaluation of these and other soil parameters are laborious, timely and some of them require various wet analytical methods. In this sense, they are not adequate for use in precision agriculture, where faster and automatic responses for the soil quality parameters are need for a large number of samples. There are in the literature several papers dealing with alternative methodologies to quantify some soil parameters, mainly organic matter and total organic carbon. Among these methodologies we can highlight the use of vis-NIR spectroscopy because the analysis are non-destructive, requires minimal or no sample treatments, does not involve the use of toxic or expensive reagents and the equipment can be used in the field, producing a response in real time. [1,2].

Several studies found in the literature related to soil analysis by vis-NIRS use the partial least squares (PLS) regression method, that can be considered a standard procedure for multivariate calibration in spectroscopy.

However, due to the complex nature of the soil samples, including heterogeneous nonlinear behavior, other regression methods should be tested, such as random forest regression, because the algorithm can incorporate complex, linear or non-linear relationships and interactions, while PLS regression is based on linear relationships between the spectra and the target variable of interest. Other advantages that we can highlight are: random forest dampens the influence of noise and outlier values, because only a small number of variables are used in each tree and a large number of trees with different variables reduces the chance of overfitting the model [3], while PLS models can easily overfit if a rigorous outlier detection criteria is not followed [4].

Based on this, this study evaluates the use of visible and near infrared spectroscopy (vis - NIRS) combined with multivariate regression based on random forest to quantify: CEC, SB, sand, clay and organic matter in soils from several regions of Brazil.

Firstly, the samples were dried at 40°C for 48 hours, a rubber mallet was used to break the soil clusters, and the granulometry was controlled by passing the sample through a sieve, with the sample ground to a size fraction <2 mm (10 mesh), then the vis-NIR spectra were collected in a dispersive Vis-NIRS spectrophotometer in the range of 400 to 2500 nm, with spectral resolution of 4 cm<sup>-1</sup>, 64 scans, in the percentage of reflectance mode.

All quality parameters studied were determined by wet standard procedures for all soil samples in IBRA, Sumaré-SP Brazil, a laboratory with certification of International Organization for Standardization (ISO) 17025, following the recommendations of EMBRAPA [5]. Spectra were preprocessed with first derivative, follow by smoothing procedure (Savitzky-Golay). Then, two thirds of samples were selected for calibration and the other one third was used in validation set. Random forest parameters were tuned using Bayesian optimization and a procedure for outlier removal was implemented. PLS models were developed following the recommendations of ASTM E1655-05 [4]. Results for PLS and Random forest (RF) models are organized in Table 1, where RMSEC and RMSEP are the root mean square error of calibration and prediction respectively.

**Table 1.** Results of Random forest and PLS models. Units of measurement are (HMFS + NaOH) g/kg for sand and clay, (mmolc/dm<sup>3</sup>) for CEC and SB and (g/dm<sup>3</sup>) for organic matter.

Soil parameter	Initial number of samples	Range of parameters	Total Number of samples after outlier removal		RMSEC		RMSEP	
			RF	PLS	RF	PLS	RF	PLS
CEC	3818	17–200	3818	3263	13.46	12.95	13.25	14.30
SB	3803	5–198	3803	3496	13.99	11.96	13.28	13.62
Sand	625	106 - 923	625	590	99	105	89	107
Clay	603	51 - 649	603	585	77.25	79.80	78.38	87.32
Organic matter	3843	5 – 79	3843	3232	6.18	5.50	5.75	6.25

It is observed in Table 1 that the errors for random forest with tuning parameters were similar to PLS. However, when comparing the total number of samples in the models, it is noted that PLS model excludes a significant number of outliers, while in the random forest models no samples were excluded. These results indicate that the Random forest method is more robust to deal with heterogeneous samples, and indicated to be used for complex and large data sets as soil.

- [1] A.M. Souza,; P. Filgueiras,; M. Coelho,; A. Fontana,; T. Winkler,; P. Valderrama,; R. Jesus Poppi. *J. Near Infrared Spectrosc* **2016**, 24 293.
- [2] K.K. Beltrame,; A.M. Souza,; T.C.B. Winkler,; W.E. Souza,; P. Valderrama. *J. Braz. Chem. Soc* **2016**, 27 1–6.
- [3] L. Breiman, *Machine Learning* **2001**, 45 1–33.
- [4] ASTM E1655-05 Standard Practices for Infrared Multivariate Quantitative Analysis, **2012**.
- [5] M. Elisabeth,; C. Claessen. *Manual Embrapa Solos* **1997**.

## Detection of Cocaine in Oral Fluid by Ultraviolet Resonance Raman Spectroscopies

D'Elia, V.<sup>1,\*</sup>, Montalvo, G.<sup>1</sup>, García Ruiz, C.<sup>1</sup>, Ermolenkov, V. V.<sup>2</sup>, Lednev, I. K.<sup>2</sup>

<sup>1</sup> *Department of Analytical Chemistry, Physical Chemistry and Chemical Engineering and University Institute of Research in Police Sciences (IUICP), University of Alcalá, Ctra. Madrid-Barcelona Km. 33.6, 28871, Alcalá de Henares (Madrid) Spain.*

<sup>2</sup> *Department of Chemistry, University at Albany, SUNY, 1400 Washington Avenue, Albany, NY, 12222, USA.*

*\*Corresponding author: valentina.d@uah.es*

According to the international statistics, cocaine is the second most commonly consumed drug overall, after cannabis, and one of the most dangerous drugs known to man. It can be sniffed as powder, ingested or rubbed into gums, inhaled as vapor or smoke, or directly injected and, therefore, it can be detected in almost all biological fluids.

In this case, oral fluid was chosen, because it is a matrix that presents multiple advantages, above all in the forensic field. In fact, it can be collected in a simple, inexpensive, and noninvasive manner by non-medical personnel, and sampling can be closely supervised without invasion of privacy, to prevent substitution, adulteration, or dilution of the sample.

This work was focused on the study of the performance of Ultraviolet Resonance Raman spectroscopy (UVRRS) for the detection of cocaine in oral fluid. Considering that cocaine shows two electronic transitions at about 200 nm and about 230 nm, we utilized UVRRS employing a laser with an excitation wavelength of 239 nm for detecting the drug in the oral fluid.

Results obtained showed that, with UVRRS, analyses can be easily carried out on non-pretreated liquid oral fluid samples. However, the rough spectra obtained did not allow to directly detect the presence of cocaine. For this reason, the signal of the undoped oral fluid was subtracted from the spectra of cocaine-doped oral fluid samples with a simple spectral treatment, and a limit of detection of 10 µg/mL was achieved. Further studies based on the employment of an UV laser emitting at about 200 nm are currently underway in our laboratory. The easiness and rapidity of the analyses here shown, could allow, in the future, to perform quick and confirmatory analyses, which also could imply the possibility to perform on-site controls.

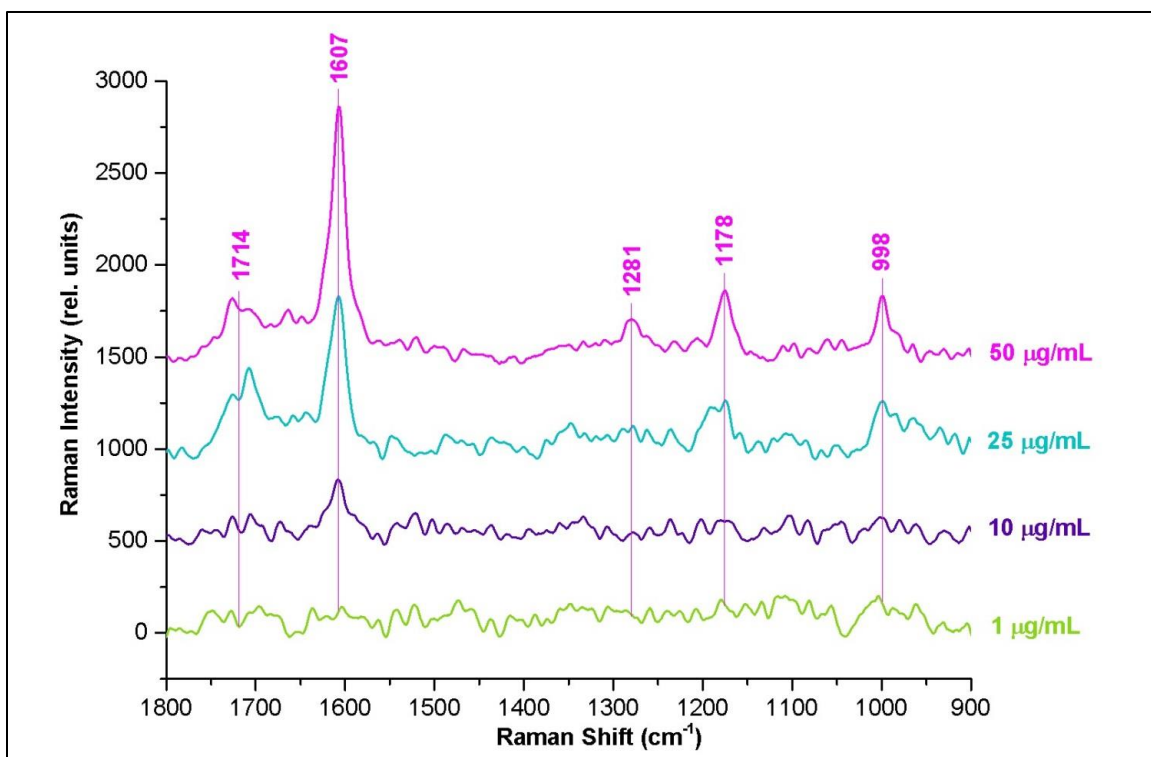


**Figure 1.** Resonance Raman spectra obtained after the subtraction of the oral fluid spectrum from the spectra of the oral fluid samples doped with cocaine at the indicated concentrations. Excitation wavelength 239 nm, excitation power 10 mW.

## Use of NIR Hyperspectral Imaging and Multivariate Curve Resolution (MCR) for detection and quantification of soy protein in beef burgers

Débora. A. P. Forchetti<sup>1\*</sup>, Ronei J. Poppi<sup>1</sup>

<sup>1</sup>*Department of Analytical Chemistry, University of Campinas (UNICAMP), Campinas, P. Box 6154, 13083-970, Brazil*

\**debora.forchetti@iqm.unicamp.br*

The quality of food is related to a set of pre-established information about appropriate conditions for its consumption and in conformity with standards values of measures/weights. However, even with the regulatory agencies of quality, numerous cases of adulteration in beef burgers are reported.

The problem is that in many cases, to cheapen the cost of the product, are added to the beef burger other meats (chicken, pork, nerves, guts, kids) or even high concentrations of ingredients susceptible to cause food intolerances or allergies, such as soy, not providing this information on the label and therefore featuring adulteration [1,2]. For beef burgers, the legislation allows a content of up to 4% the soy protein, and its presence gives the product greater juiciness due to its ability to retain water and emulsify fat.

In this work, is proposed a methodology for the detection and quantification of soy in beef burgers, based on the combination of NIR Hyperspectral Imaging and chemometric data analysis. Among the main advantages of this application we can cite the fact that hyperspectral images can provide information about the distribution and quantification with low limits of detection of the components of the samples, with little or no sample preparation [3]. Besides that, by using the multivariate curve resolution method, are obtained the pure spectra of the compounds, making possible their identification.

The analysis was conducted by a Spotlight 400N FT-NIR Imaging System from Perkin\_Elmer. The samples were placed between two glass slides to ensure a homogeneity in the surface and put on a support for microscopy and thereafter they were accommodated on the positioned for diffuse reflectance measurements. By using a joystick, the focus and the area to be analyzed were adjusted. The conditions of the measurements were 32 scans per spectra in the range of 4000 to 7800  $\text{cm}^{-1}$ , pixel size of 50  $\mu\text{m}^2$  and monitored of 80 x 80 pixels.

Multivariate curve resolution calculations were performed using the MCR-ALS GUI 2.0 for Matlab. The spectra were first converted to absorbance ( $\log 1/R$ , where R is the reflectance) to ensure a proportional relationship with the concentration of the components. After that, to remove the light scattering, that is usual in diffuse reflectance of powder samples, multiplicative signal correction (MSC) was applied in all spectra of the mapped area, using the average spectra as reference.

The analysis began with homemade burgers made from mixing ground beef with spices (garlic, onion and salt) and adulterated with different concentrations of soy protein. Analyzing these samples by the proposed method, the results obtained for quantification of soy may not have surpassed a 3% error, as can be seen in table 1.

**Table 1:** Results for protein soy in homemade beef burger

Actual Values (%)	Predicted Values (%)	Error (%)
5.0	5.1	0.1
10.0	7.1	2.9
15.0	14.2	0.8
25.0	25.0	0.0

The results for four commercial samples beef burger are in figure 1.

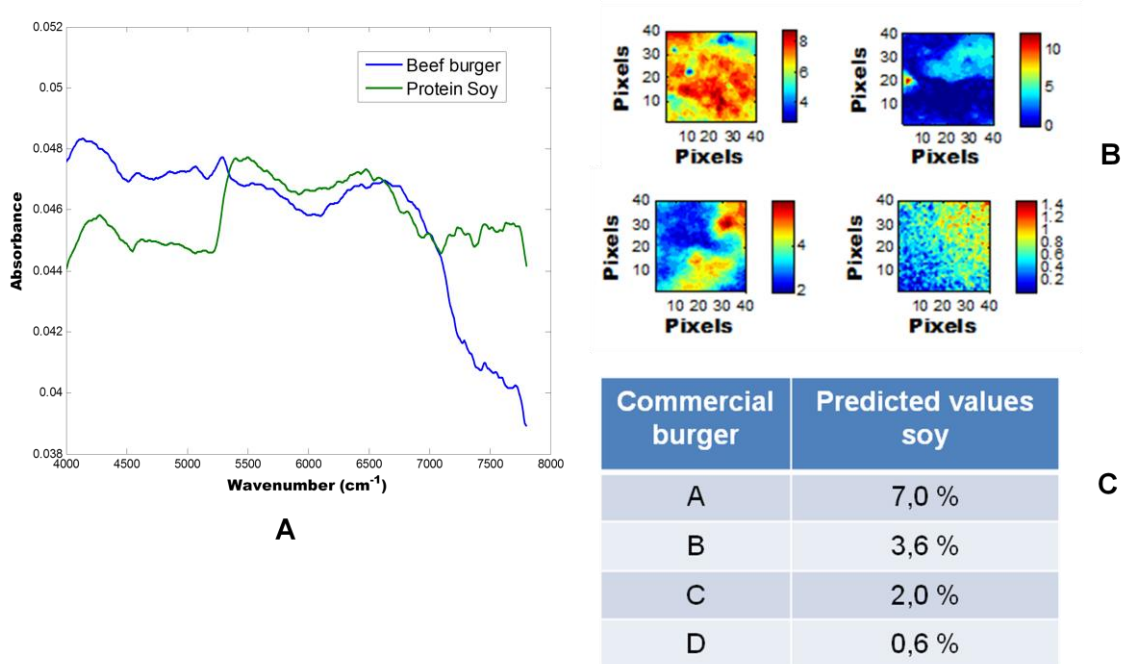


**Figure 1:** (A) Recovered spectrum for soy protein and beef burger; (B) chemical maps for commercial beef burgers; (C) predicted values for protein soy.

The use of NIR Hyperspectral Imaging in conjunction with multivariate curve resolution made possible the detection and quantification of protein soy in beef burger samples. Among the four commercial beef burgers analyzed, only one presented values that exceeded the allowed limit of 4% for soy, but if we consider the error associated with the method, it could be acceptable.

As a major advantage of this methodology is the possibility of detection of adulterant even in heterogeneous samples, where a small adulterant amount can be concentrated on a specific point of the mapped area. Also, from the obtained spectra is possible to identify the adulterant.

- [1] Perderson, H. E. ; Fleischwirtschaft **1995**, 75, 798-802.
- [2] Fontan,R. C. I.; Rebouças,K. H.; Veríssimo, L. A. A.; Machado, A. P. F.; Fontan, G. C. R.; Bonomo, R. C. F; Alim. Nutr. **2011**, 22,429-434.
- [3] Schweitzer, R. C.; Bangalone, A. S.; Treado, P.; Managing the Lab. **2000**, 5, 7-13.

# Non-destructive Analysis of Carotenoid in Leaf Vegetables Using Raman Spectroscopy

Takuma Genkawa<sup>1,\*</sup>, Masato Tanakaka<sup>1</sup>, Risa Hara<sup>1</sup>, Mika Ishigaki<sup>2</sup>, Yukihiro Ozaki<sup>2</sup>

<sup>1</sup> Faculty of Life and Environmental Sciences, University of Tsukuba, 1-1-1 Tennodai,  
Tsukuba, Ibaraki, Japan

<sup>2</sup> School of Science and Technology, Kwansai Gakuin University, 2-1 Gakuen, Sanda,  
Hyogo, Japan

\* genkawa.takuma.fm@u.tsukuba.ac.jp

## **Introduction**

Lutein is a typical carotenoid contained in spinach leaf, and has been interested recently because of its health promoting effect on human eyes. Therefore, non-destructive analysis of lutein content in spinach leaf is required.

Lutein shows absorption peaks in the visible light region, for example 443 and 470nm, but it is not straightforward to measure these peaks in visible spectrum of spinach leaf. Due to strong absorption of chlorophyll in the spinach leaf, lutein peaks in the visible region are difficult to be detected. In addition, lutein concentration in spinach is a few milligram per 100 g fresh weight and thinness of leaf is about 1 mm, therefore absorption spectroscopy is not acceptable.

In the present study, Raman spectroscopy is employed for non-destructive analysis of lutein in spinach leaves. Resonance or Pre-resonance Raman effects emphasize peak intensity of carotenoids, thus use of Raman spectroscopy will overcome above problems in low-concentration analyte in thin leaf sample. The objective of the present study was to confirm feasibility of non-destructive analysis of lutein in spinach leaves using Raman spectroscopy.

## **Methods**

Raman spectra of fresh spinach leaves with different lutein concentration were measured with 532, 785, and 1064 nm excited Raman spectrometers. The measurement points were three points of a leaf of spinach. Baseline corrected spectra are investigated.

## **Results and Discussion**

In Raman spectra of spinach leaves, intense bands at 1520 cm<sup>-1</sup> and 1160 cm<sup>-1</sup> assigned to carotenoids are observed, as same as Raman spectrum of tomatoes (Figure 1). In Raman spectrum of lutein reagent also shows intense bands at 1520 cm<sup>-1</sup> and 1160 cm<sup>-1</sup>, while many intense bands were observed in the spectrum of chlorophyll. These results indicate peaks of carotenoid, including lutein, were detected in Raman spectrum of spinach leaves specifically even though concentration of chlorophyll is much higher than lutein.

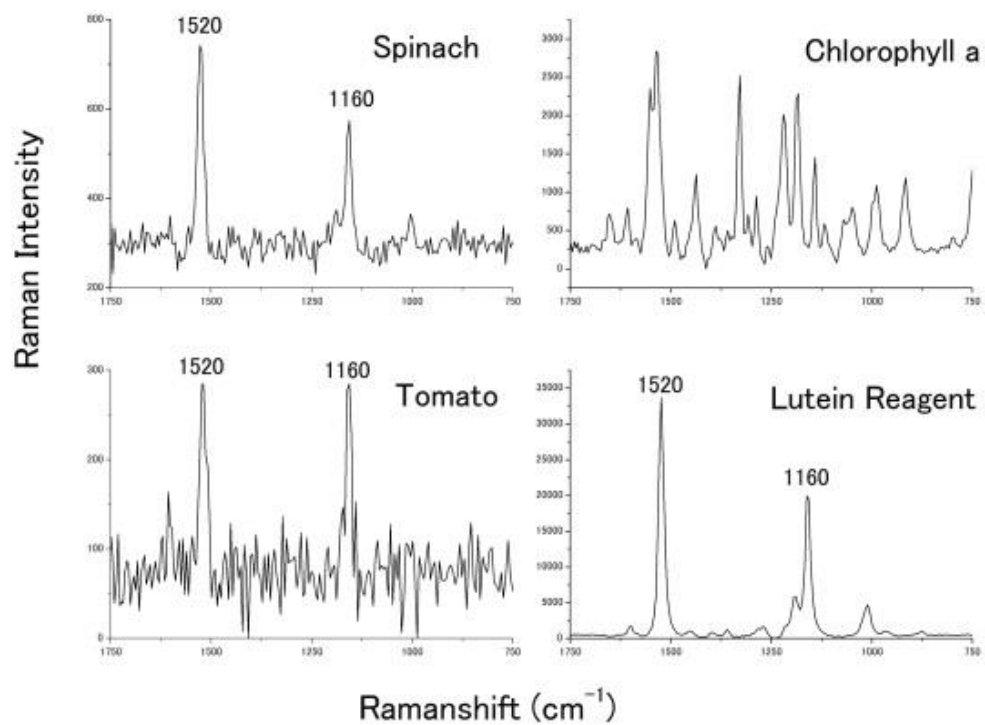


**Figure 1.** Raman spectra of spinach, tomato, chlorophyll, and lutein

***Acknowledgement***

This research was supported by grants from the Project of the NARO Bio-oriented Technology Research Advancement Institution (the special scheme project on regional developing strategy)

[1] Baranska, M.; Schulz, H.; Siuda, R.; Strehle, M. A.; Roesch, P.; Popp, J.; Joubert, E.; Manley, M; *Biopolymers* **2005**, 77 (1), 1–8.

[2] Ozaki, Y.; Cho, R.; Ikegaya, K.; Muraishi, S.; Kawauchi, K., *Applied spectroscopy* **1992**, 46 (10), 1503–1507.

## Discriminant Analysis of Carotenoid-rich Tomatoes Using Raman Spectroscopy and PMIR

Risa Hara<sup>1</sup>, Mika Ishigaki<sup>2</sup>, Yasutaka Kitahama<sup>2</sup>, Leilei Zhang<sup>2,3</sup>,  
Yukihiro Ozaki<sup>2</sup>, Takuma Genkawa<sup>1,\*</sup>

<sup>1</sup> Faculty of Life and Environmental Sciences, University of Tsukuba, 1-1-1 Tennodai,  
Tsukuba, Ibaraki, Japan

<sup>2</sup> School of Science and Technology, Kwansei Gakuin University, 2-1 Gakuen, Sanda,  
Hyogo, Japan

<sup>3</sup> College of Life Sciences, China Jiliang University, Hangzhou 310018, China  
\* genkawa.takuma.fm@u.tsukuba.ac.jp

### Introduction

Raman spectroscopy is a powerful tool for analysis of carotenoids in healthy food products. However, Raman spectroscopy has a challenging subject of obtaining inefficient reproducibility in Raman intensity especially for food samples due to reabsorption. Therefore, there are still few practical applications of Raman spectroscopy in food science, and new measurement and analysis methods are required. In the present study, we developed discriminant analysis of carotenoid-rich tomatoes using Raman spectroscopy combined with a new analysis method, Product of mean intensity ratio (PMIR). In PMIR analysis, Raman spectrum is measured with a short exposure time with which peaks of carotenoid are confirmed. Because the peaks are observed only in the carotenoid-rich tomatoes, therefore PMIR values can distinguish carotenoid-rich samples. In the present study, the feasibility of discriminant analysis of carotenoid-rich tomatoes was evaluated using intact tomatoes in different mature stages. In addition, suitable excitation wavelength was investigated.

### Methods

Raman spectra of intact tomatoes in different mature stages (green, breaker, turning, pink, red) were measured with 532, 785, and 1064 nm excited Raman spectrometers. The measurement points were four points at even intervals around the equator of a tomato.

A new analysis method, PMIR was developed for distinction of the peak's existence by calculation instead of the naked eye. In the present study a peak which has following two characteristics, is defined as "peak existence". Assume that peak intensity is twice stronger than baseline area intensity and the peak has more than three point's width. PMIR value was calculated by following formula.

$$\text{PMIR} = \frac{I_{L1} * I_{L2}}{I_B^2}$$

where, L1 and L2 are the regions of carotenoid peaks (the regions of 1523–1513 and 1161–1151 cm<sup>-1</sup>), and B is the range of baseline (1500–1200 cm<sup>-1</sup>). I<sub>L1</sub>, I<sub>L2</sub>, and I<sub>B</sub> are the mean intensities of L1, L2, and B.

## Results and Discussion

Intensity of carotenoid peak increase with increase in carotenoid concentration, and signal to noise ratio (SNR) of Raman spectra depends on the excitation wavelength (Figure 1). Because the absorption band of carotenoid exists in the 350–500 nm region, highest SNR was obtained in the spectra obtained with 532 nm excitation (Figure 1A).

On the other hand, discriminant analysis by PMIR succeeded using Raman spectra measured with 785 nm and 1064 nm excitation. In the measurement with the conditions of the limitation of peak existence, peaks exist only in red tomatoes, but do not in relatively low carotenoid concentration samples (Figure 1B, 1C). The threshold level of peak existence could be adjusted by changing exposure time.

Clear and strong peaks were observed in the spectra of carotenoid-rich tomatoes, whereas, no strong peak was observed for tomatoes having relatively low carotenoid concentration. Tomatoes with high carotenoid concentration could be distinguished successfully with 95% hit ratio based on the PMIR value. As a conclusion, the feasibility of discriminant analysis of carotenoid-rich products was confirmed using a combination of Raman spectroscopy and PMIR.

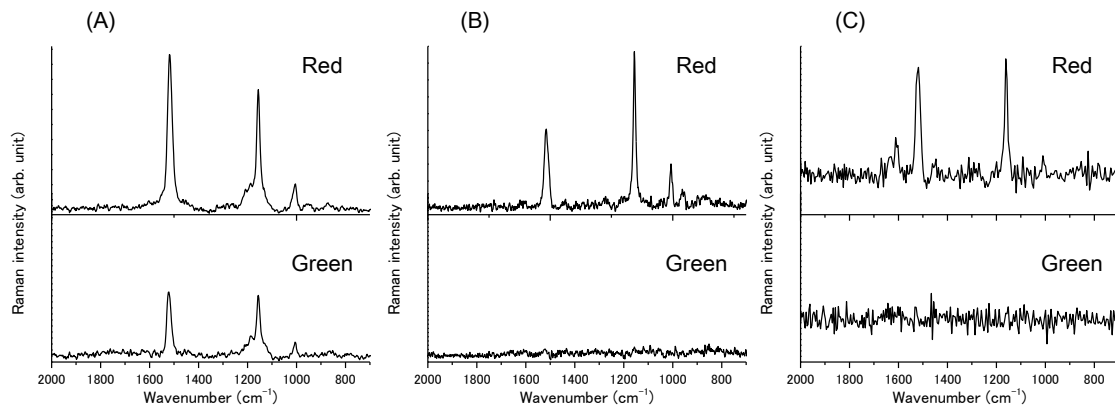


**Figure 1.** Baseline-corrected Raman spectra of red and green tomatoes (excitation wavelength: (A) 532 nm, (B) 785 nm, (C) 1064 nm)

## Acknowledgement

This research was supported by grants from the Project of the NARO Bio-oriented Technology Research Advancement Institution (the special scheme project on regional developing strategy)

- [1] Baranska, M.; Schulz, H.; Siuda, R.; Strehle, M. A.; Roesch, P.; Popp, J.; Joubert, E.; Manley, M.; *Biopolymers* **2005**, *77* (1), 1–8.
- [2] Ozaki, Y.; Cho, R.; Ikegaya, K.; Muraishi, S.; Kawauchi, K., *Applied spectroscopy* **1992**, *46* (10), 1503–1507.

## Visible Light Tomography as a Tool for identifying Edges in FTIR Tomography

Nick M. Walter, Carol J. Hirschmugl\*

*Department of Physics, University of Wisconsin-Milwaukee, Milwaukee WI, USA, 53201*

*\* e-mail: [cjhirsch@uwm.edu](mailto:cjhirsch@uwm.edu)*

Using Fourier transform infrared (FTIR) spectro-microtomography, we can visualize how chemical bands are distributed throughout a biological or materials sample. In FTIR tomography, a series of two-dimensional (2D) FTIR absorption images are taken while a sample is rotated. By applying computational tomography algorithms, 3D reconstructions of the sample are created at each wavelength.<sup>1</sup>

Visually displaying these reconstructions can be problematic for weak chemical bands and spectral regions with high levels of noise, as distinguishing the edge of the sample from the background noise may be difficult. Previously, we corrected for this by implementing visible light tomography to create a 3D mask, which can then be multiplied with our reconstructions to remove all voxels (3D pixels) that fall outside our mask, as shown in Fig. 1.

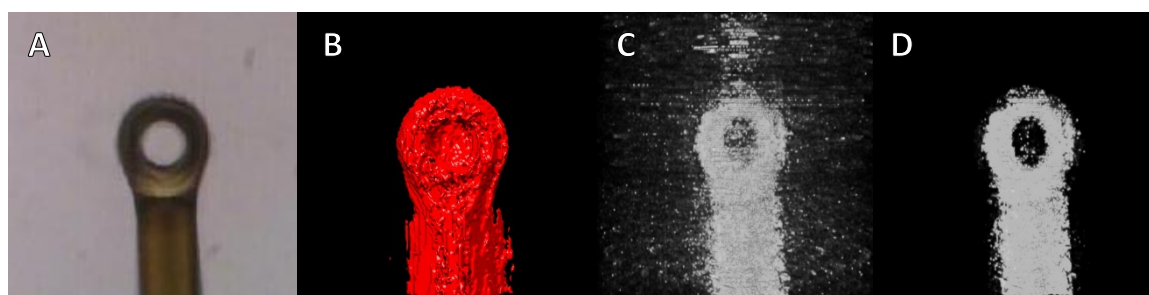


**Figure 1.** (A) A visible image of an empty 20 $\mu\text{m}$  microloop. (B) A 3D mask of the 20 $\mu\text{m}$  microloop generated using visible light tomography. All red voxels have a value of one, while all black voxels have a value of zero. (C) An FTIR tomographic reconstruction of a weak chemical band (1543-1647 $\text{cm}^{-1}$ ). (D) The resulting image after multiplying the mask in part B with the reconstruction in part C. Notice the noise surrounding the microloop has been significantly reduced, and it is easier to see the shape of the loop itself.

We implement visible light tomography using the same experimental setup as FTIR tomography. While a sample is rotated, a series of visible images are taken. Since the visible light camera has a larger detector area and a smaller pixel size than the infrared detector, these visible light images must be cropped and resized. The same computational tomography algorithms used to create FTIR tomographic reconstructions are used for these visible light images, giving visible light reconstructions, which were previously used to create masks, as in Fig. 1.

Recently, FLIR Systems, Inc. has developed a line of cameras which allow the user to take both visible and IR images. When set to collect IR images, the camera uses the visible light images to define hard edges, which are then displayed concurrently with the IR images, as shown in Fig. 2. These edges help to identify sources of infrared radiation.



**Figure 2.** An IR image of a laptop taken using a FLIR C2 camera. Notice the clearly defined edges, which come from the visible light information.

In this poster, we will demonstrate a similar approach for FTIR tomography, using visible light tomography. Just like the FLIR camera uses 2D visible light images to create 2D edge images, we plan on creating 3D mesh reconstructions from visible light tomography. These mesh reconstructions will be overlaid with the FTIR solid tomographic reconstructions, defining the edges and outlining the boundaries of the sample. This will provide a greater understanding of exactly how chemical signatures are spatially distributed within a sample.

This work was supported by the UWM Physics department and NSF grants CHE-1508240 and CHE-1112433.

[1] M. Martin *et al.*, *Nature Methods*, **2013**, 10, 9, 861-864.

## **Spectrally Resolved Infrared Microscopy And Chemometric Tools To Reveal The Interaction Between Blue Light (470 Nm) And Methicillin-Resistant *Staphylococcus Aureus* (MRSA)**

Ebrahim Aboualizadeh<sup>1</sup>, Violet V. Bumah<sup>2</sup>, Daniela S. Masson-Meyers<sup>2</sup>, Janis T. Eells<sup>2</sup>,  
Chukuka S. Enwemeka<sup>3</sup>, Carol J. Hirschmugl<sup>1\*</sup>

<sup>1</sup>*Physics Department, University of Wisconsin-Milwaukee, Milwaukee, USA*

<sup>2</sup>*Department of Biomedical Sciences, University of Wisconsin-Milwaukee, Milwaukee, USA*

<sup>3</sup>*Office of provost, San Diego State University, San Diego, USA*

\**cjhirsch@uwm.edu*

Blue light inactivates methicillin-resistant *Staphylococcus aureus* (MRSA), a Gram-positive antibiotic resistant bacterium that leads to fatal infections [1]; however, the mechanism of bacterial death remains unclear. In this study, to uncover the mechanism underlying the bactericidal effect of blue light, a combination of Fourier transform infrared (FTIR) spectroscopy and chemometric tools is employed to detect the photoreactivity of MRSA and its distinctive pathway toward apoptosis after treatment [2].

The mechanism of action of UV light and vancomycin against MRSA is also investigated to support the findings. Principal component analysis followed by linear discriminant analysis (PCA- LDA) is employed to reveal clustering of five groups of MRSA samples, namely untreated (control I), untreated and incubated at ambient air (control II), irradiated with 470 nm blue light, irradiated with 253.5 UV light, and vancomycin-treated MRSA. Loadings plot from PCA-LDA analysis reveals important functional groups in proteins (1683, 1656, 1596, 1542  $\text{cm}^{-1}$ ), lipids (1743, 1409  $\text{cm}^{-1}$ ), and nucleic acids region of the spectrum (1060, 1087  $\text{cm}^{-1}$ ) that are responsible for the classification of blue light irradiated spectra and control spectra (Fig. 1). Cluster vector plots and scores plot reveals that UV light-irradiated spectra are the most biochemically similar to blue light- irradiated spectra; however, some wavenumbers experience a shift. The shifts between blue light and UV light irradiated loadings plot at vasym PO2- band (from 1228 to 1238  $\text{cm}^{-1}$ ), DNA backbone (from 970 to 966  $\text{cm}^{-1}$ ) and base pairing vibration of DNA (from 1717 to 1712  $\text{cm}^{-1}$ ) suggest distinctive changes in DNA conformation in response to irradiation (Fig. 1).

Our findings indicate that irradiation of MRSA with 470 nm light induces A-DNA cleavage and that B-DNA is more resistant to damage by blue light. Blue light and UV light treatment of MRSA are complementary and distinct from the known antimicrobial effect of vancomycin. Moreover, it is known that UV-induced cleavage of DNA predominantly targets B-DNA, which is in agreement with the FTIR findings.

This work was supported by the UWM Physics department and NSF grants CHE-1508240 and CHE-1112433.

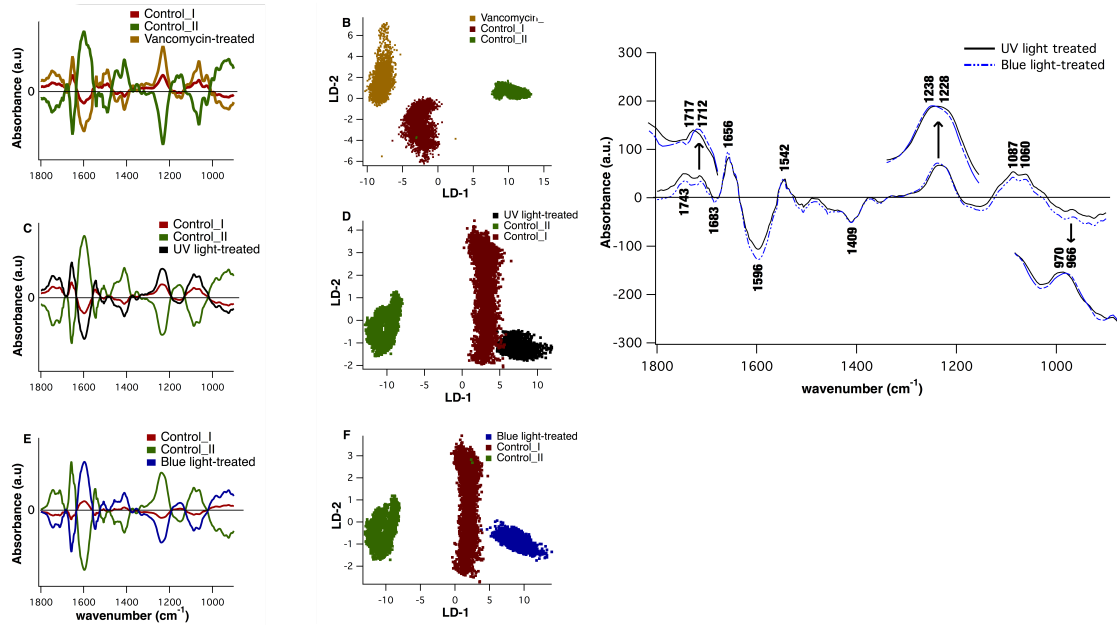


**Figure 1.** Left: Cluster vector plots and corresponding 2D scores plot (LD2 vs. LD1) from PCA-LDA analysis. A,B) Comparison between control groups and vancomycin-treated spectra, C,D) Comparison between control groups and UV-light irradiated spectra, and E,F) Comparison between control groups and blue light-irradiated spectra. In PCA-LDA plots, red (control I), green (control II), blue (blue light irradiated), black (UV-light irradiated), and yellow (vancomycin-treated) colors are used. Right: Cluster vector plots derived from the comparison of control groups vs. blue-light irradiated spectra (blue dashed line) and control groups vs. UV light-irradiated (black solid line) spectra are overlaid. The FTIR bands that are indicative of blue-light and UV light-induced damage to MRSA are highlighted. Clear shifts in the loadings plot from 966, 1238, 1712  $\text{cm}^{-1}$  (blue light-irradiated) to 970, 1228, 1717  $\text{cm}^{-1}$  (UV light-irradiated) are shown.

[1] Enwemeka, C. S.; Williams, D.; Enwemeka, S. K.; Hollosi, S.; Yens, D. *Photomed Laser Surg.* **2009**, *27*(2), 221-226.

[2] Bumah, V. V.; Aboualzadeh, E.; Masson-Meyers, D. S.; Eells, J. T.; Enwemeka, C. S.; Hirschmugl, C. J. *Journal of Photochemistry and Photobiology B: Biology*, **2017**, *167*, 150-157.

# Enhancement of Hyperspectral Data Applied to Localizing Chemically Distinct Macromolecules

Ghazal Azarfar<sup>1,2</sup>, Ebrahim Aboualizadeh<sup>1</sup>, Carol J Hirschmugl<sup>1\*</sup>

<sup>1</sup>*Department of Physics, University of Wisconsin Milwaukee, Milwaukee WI, 53211*

<sup>2</sup>*Department of Electrical Engineering, University of Wisconsin Milwaukee, Milwaukee WI, 53211*

\* *cjhirsch@uwm.edu*

Fringes arise in infrared spectra and images of thin films due to multiple internal reflection (similar to that encountered with soap bubbles or oil slick on water for visible wavelengths) and hinder the quality of the measured hyperspectral data. Employing a bright synchrotron source, a microscope coupled to a FTIR spectrometer, and replacing a single detector with an array of detectors (128 x 128 detectors) enables collecting combined spectral and spatial infrared data simultaneously. A measured spectrum can be simulated as the summation of a standard spectrum and a fringe spectrum, as shown in Fig. 1. Thus, raw spectra with fringes (before) can be "corrected" by removing a fringe spectrum (after).

In this work, an extended multiplicative signal correction method based on Fourier analysis [1] of the raw spectrum (before) can be employed to identify and remove the fringes in the spectral domain. The fringe estimation algorithm is demonstrated in Fig.2 A to Fig.2 C. A Fourier transform of the spectrum in the absorption free region reveals frequencies of sinusoidal waves. By selecting the dominant frequencies, a fringe spectrum is simulated. This approach is applied to 24800 spectra of the hyperspectral cube with fringes that are up to 50% of the intensity. Spectra are extracted from 1037 images covering spectral range between  $950\text{ cm}^{-1}$  to  $2950\text{ cm}^{-1}$  ( $3.4\text{ }\mu\text{m}$  to  $10\text{ }\mu\text{m}$ ) from a live algal cell ( $\sim 10 \times 20\text{ }\mu\text{m}^2$ ) maintained in a liquid flow cell.

Two cases are demonstrated. The first case contains fringes that are dominant in the images. The second case contains fringes that are dominant in the spectra. The results shown in Fig. 2 D to G illustrate that the algorithm is effective in both cases.

Next, the dimension of the improved hyperspectral data is reduced using multidimensional Principal Component Analysis to extract the most important components (spectrally and spatially) [2]. Comparing of the first three principal components (before and after correction) one can see a high degree of improvement in visualization of spatial distribution of macromolecules after the correction, better localizing the biochemical constituents.

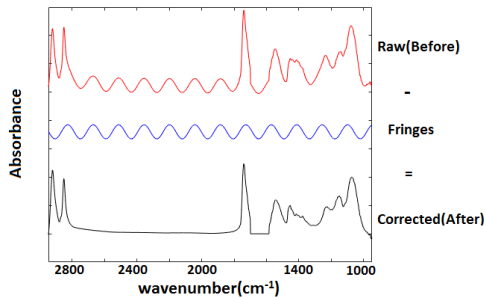


**Figure 1.** A raw spectrum (top), can be constructed from a summation of a fringe pattern (middle), and a reference spectrum (bottom). Thus, an estimated fringe spectrum can be subtracted from a raw spectrum (Before) to recover a corrected spectrum (After).

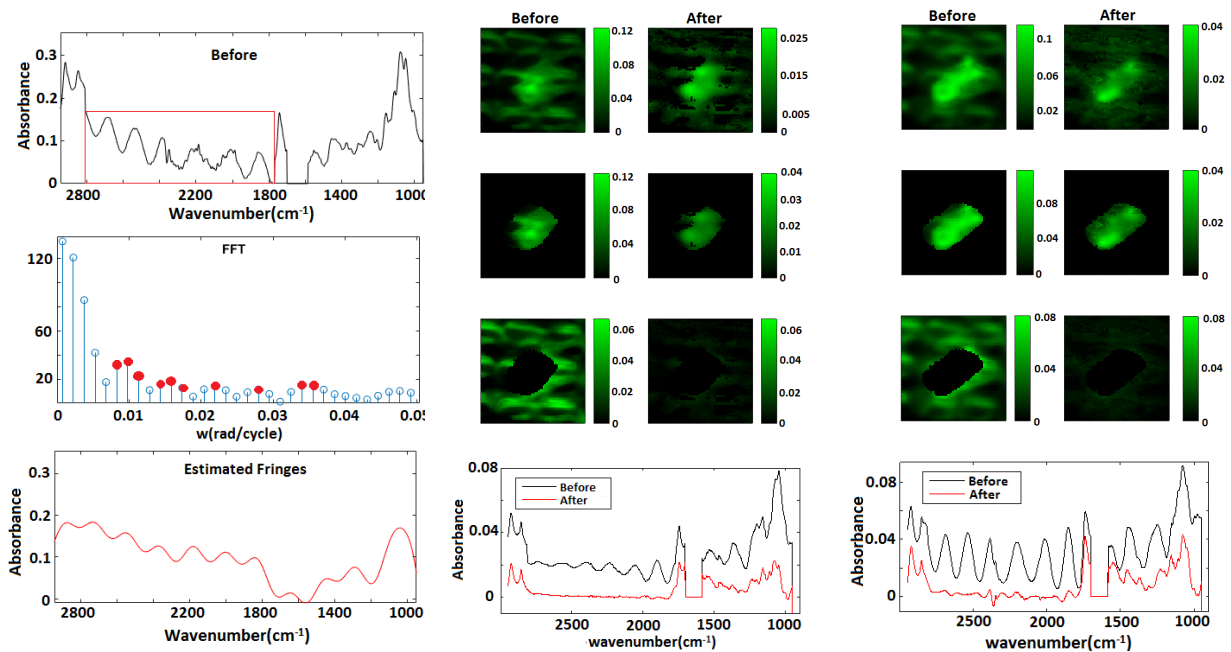


**Figure 2.** Left: An example raw spectrum (Before) is distorted by fringes before any corrections, the red box shows the region that is selected for fringe estimation. Fourier transform (FFT) of the red box in A, dominant frequencies are highlighted with red circles. Estimated fringe spectrum (After) based on dominant frequencies. Right: Two cases for fringes (see text). Images with corresponding average spectrum of the hyperspectral cube from data above, before and after correction.

[1] Konveskikh, T.; Ponossov, A.; Blumel, R.; Lukacs, R.; Kohler, A. *Analyst* 2015, 140, 3969–3980  
 [2] Hobro, A. J.; Pavillon, N.; Fujita K.; Ozkan, M.; Coban, C.; Smith, N. I. *Analyst* 2015, 140, 2350-2359,  
 [3] Mattson, E. C.; Aboualizadeh, E.; Barabas, M. E.; Stucky C. L.; Hirschmugl, C. J.; *International Journal of Molecular Sciences* 2013, 14, 22753-22781.  
 [4] Bannon, D. *Nature Photonics* 2009, 3, 627-629,.

# Fundamental Studies on Graphene-based Surface-Enhanced Infrared Absorption Spectroscopy

Yuan Hu<sup>1</sup>, Boris Mizaikoff<sup>1,\*</sup>

<sup>1</sup>*Institute of Analytical and Bioanalytical Chemistry, Ulm University, 89081 Ulm, Germany*

\**boris.mizaikoff@uni-um.de*

Surface enhanced infrared absorption spectroscopy (SEIRA) promises significantly improved sensitivity in comparison to conventional infrared spectroscopy, and enables in-situ, real-time characterization of adsorption/desorption and reaction processes at the solution interphase. Coincidentally, highly discriminatory chemical, structural and compositional information on molecules in direct vicinity of substrate surfaces is provided [1–3]. Diverse geometries of plasmonic nanostructures have been engineered as SEIRA substrates, most of which are based on noble metals. To provide reproducible and reliable SEIRA signals, the reproducibility of nanostructures formation is essential, however, remains challenging [4]. Graphene is a two-dimensional semi-metallic material, which has been proposed as promising alternative material in SEIRA [5], due to its electrical conductivity, spatial plasmon confinement, and unprecedented electrical/optical tuning properties, which distinguishes graphene from conventional metals [6].

Here, we report a graphene-based SEIRA strategy for analyzing a variety of molecules at a sample surface via enhanced vibrational signatures. High-quality graphene sheets were obtained by chemical vapor deposition (CVD), structured, and transferred to an IR waveguide surface for subsequent measurements. The influence of the graphene properties and experimental conditions were investigated in detail. After optimization, the investigated molecules revealed a significant infrared absorption signal amplification in the presence of graphene with excellent reproducibility and stability. Furthermore, potential enhancement mechanism were studied in detail thereby facilitating an effective graphene-based SEIRA platform for various analytical applications.

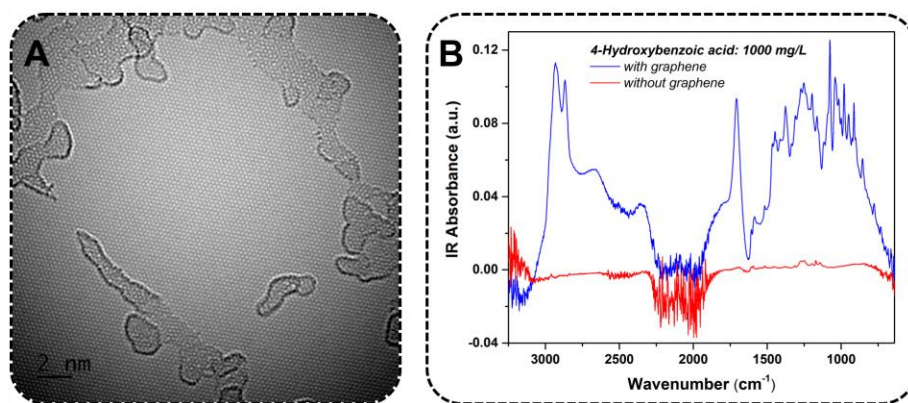


**Figure 1.** (A) Representative high-resolution TEM image of CVD graphene used in the present study: large area graphene monolayers displayed defect-free atomic structures

accompanied by smaller graphene flakes; (B) Unprocessed mid-infrared spectra of a tested molecule, i.e., 4-hydroxybenzoic acid at a concentration of 1000 mg/L (in water) revealing strongly enhanced infrared absorption signatures when using graphene-modified IR waveguide substrates.

- [1] Wu, L.; Zeng, L.; Jiang, X. *J. Am. Chem. Soc.* **2015**, *137*, 10052–10055.
- [2] Kellner, R.; Mizaikoff, B.; Jakusch, M.; Wanzenböck, H. D.; Weissenbacher, N. *Appl. Spectrosc.* **1997**, *51*, 495–503.
- [3] López-Lorente, Á. I.; Wang, P.; Mizaikoff, B. *Microchim Acta* **2017**, *184*, 453–462.
- [4] Le, F.; Brandl, D. W.; Urzhumov, Y. A.; Wang, H.; Kundu, J.; Halas, N. J.; Aizpurua, J.; Nordlander, P. *ACS Nano* **2008**, *2*, 707–718.
- [5] Rodrigo, D.; Limaj, O.; Janner, D.; Etezadi, D.; García de Abajo, F. J.; Pruneri, V.; Altug, H. *Science* **2015**, *349*, 165–168.
- [6] Low, T.; Avouris, P. *ACS Nano* **2014**, *8*, 1086–1101.

## Wavelength Selection for Multiple Linear Regression Modeling using SRSNV.

Yuto Ishizumi<sup>1</sup>, Mika Ishigaki<sup>2</sup>, Yukihiro Ozaki<sup>2</sup>, Takuma Genkawa<sup>1,\*</sup>

<sup>1</sup>*Faculty of Life and Environmental Sciences, University of Tsukuba, 1-1-1 Tennodai, Tsukuba, Ibaraki, Japan*

<sup>2</sup>*School of Science and Technology, Kwansai Gakuin University, 2-1 Gakuen, Sanda, Hyogo, Japan*

\* *genkawa.takuma.fm@u.tsukuba.ac.jp*

There is an increasing demand for non-destructive measurement technology using spectroscopic analysis as on-site analysis, because of its rapidness and convenience. For the on-site analysis, small size, low cost, and good prediction accuracy are required for the spectrometer. Filter-based spectrometer is a candidate of such one, but selection of wavelength for the filter is time-consuming and prediction accuracy depends on experience of analyst. In the present study, a wavelength selection method, points selection multiple linear regression (PSMLR), was proposed for selecting wavelength for MLR modeling using searching region standard normal variate (SRSNV)<sup>1</sup>.

PSMLR is comprised of the following operation (Figure 1A). First, 2 spectral channels where the maximum and minimum absorbance were obtained ( $\mathbf{x}_{Amax}$ ,  $\mathbf{x}_{Amin}$ ) are chosen among spectra  $\mathbf{X}$ . Next, a spectral window, a submatrix  $\mathbf{X}_i$  of the size of  $ws$  spectral channels, is constructed, then, SNV is performed ( $\mathbf{X}_i^{SNV}$ ) followed by calculating PLS regression model for an analyte concentration  $\mathbf{y}$ . From the first latent variable (LV) loading of the PLSR model, 3 spectral channels of maximum and minimum loading values ( $\mathbf{x}_{Lmax}$  and  $\mathbf{x}_{Lmin}$ ) and near-zero loading value ( $\mathbf{x}_{L0}$ ) between  $\mathbf{x}_{Lmax}$  and  $\mathbf{x}_{Lmin}$  are chosen. Thus, 5 spectral channels are chosen, and 4 type of MLR models are developed using absorbance at these 5 spectral channels. The window is moved over the full spectral region. Using absorbance at 5 spectral channels a series of MLR models is constructed, and the root mean square error (RMSE) is calculated. In a plot of the RMSE versus the position of the window, the spectral window showing the minimum RMSE is selected as the optimal spectral region for PSMLR, and 3 spectral channels for MLR modeling are determined.

In the present study, PSMLR was performed using the in-house programs coded in R statistical software. To evaluate the performance of PSMLR, near-infrared spectral data set of mixture samples consisting wheat flour and granular glucose was used. The mixed samples contained 0–100% glucose at 5% intervals (Figure 1B). The prediction accuracy of the MLR model for glucose concentration based on PSMLR at a window size of 150 spectral channels was compared with those of PLSR models using original and SNV spectra in the full spectral region. To validate these regression models, the leave-one-out cross-validation method was employed, and coefficient of determination ( $R^2$ ) and RMSE values were compared.

Based on a result of PSMLR calculation, the spectral channels at 8880, 8724, 8512  $\text{cm}^{-1}$  were selected as  $\mathbf{x}_{L\max}$ ,  $\mathbf{x}_{L0}$ , and  $\mathbf{x}_{L\min}$ . As shown in Table 1, PLMLR of model 3 showed a  $R^2$  of 0.989 and a RMSE of 3.1% without any spectral pretreatment. In conclusion, it was possible to select the optimal spectral channels for MLR modeling using PSMLR.

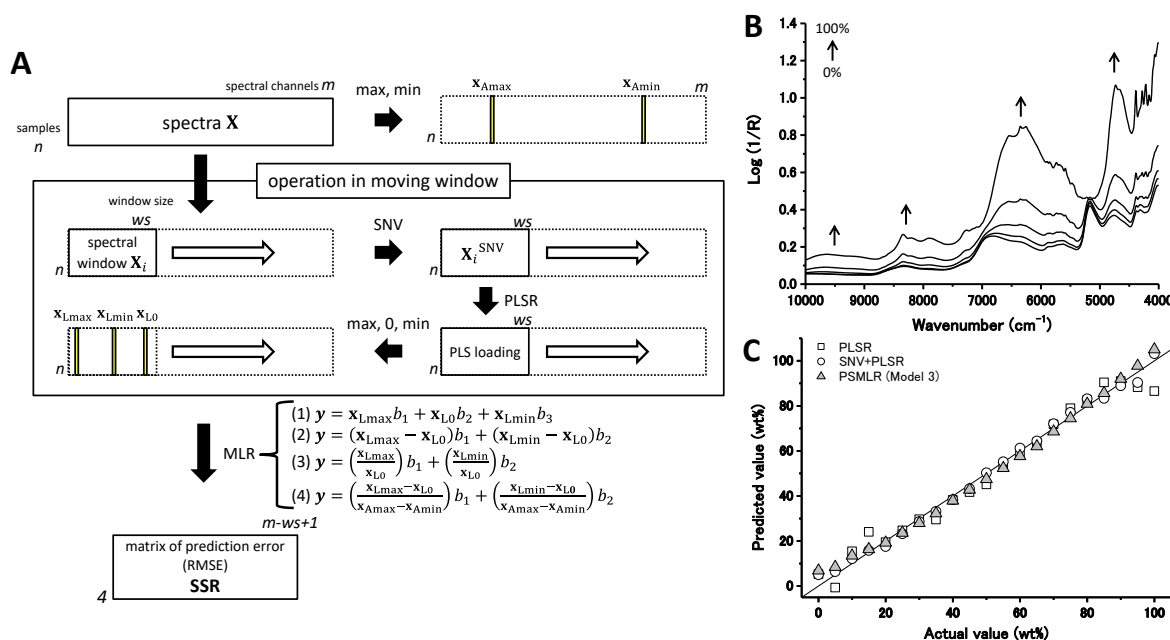


**Figure 1.** (A) Schema of PSMLR, (B) Original spectra of glucose-flour mixture samples (0, 25, 50, 75 and 100% glucose), (C) Comparison between 3 regression models.

Table 1. Analysis conditions and cross-validation results of regression models for a mixture of granular glucose and wheat flour.

Regression model	Pretreatment	Spectral region, <sup>a</sup> $\text{cm}^{-1}$	$R^2$	RMSECV, wt%	No.LVs
PLSR	—	10000–4000 (1501)	0.975	5.0	4
SNV+PLSR	SNV	10000–4000 (1501)	0.995	2.3	3
PSMLR (Model 3)	—	8880, 8724, 8512 (3)	0.989	3.1	—

<sup>a</sup> Figures in parentheses indicate the number of spectral channels.

### Acknowledgement

This research was supported by grants from the Project of the NARO Bio-oriented Technology Research Advancement Institution (the special scheme project on regional developing strategy).

[1] Genkawa, T.; Shinzawa, H.; Kato, H.; Ishikawa, D.; Murayama, K.; Komiyama, M.; Ozaki, Y. *Appl. Spectrosc.* **2015**, 69, 1432–1441.

## Identification and Quantification of Bacteria Based on SERS

Sila Jin<sup>1</sup>, Joohee Oh<sup>1</sup>, Yeonju Park<sup>1</sup>, Young Mee Jung<sup>1,\*</sup>

<sup>1</sup>*Department of Chemistry, Kangwon National University, Chuncheon 24341, Korea*

*\*ymjung@kangwon.ac.kr*

Bacteria can be beneficial or harmful to humans depending on the species. Therefore, fast and accurate determination and identification of bacteria should be performed to prevent damages caused by disease, food safety, even bio-terror threats.

Detection methods such as polymerase chain reactions (PCR), enzyme-linked immunosorbent assays (ELISA) have been developed to identify bacteria. However, it takes a long time to amplify the amount of bacteria, and there is a limit to know information about bacteria to be detected in advance.[1,2]

Surface-enhanced Raman scattering (SERS) is a powerful technique to detect biological reagent because it provides rapid and ultra-sensitive detection with a large amount of fingerprint information for the identification of biological materials without culturing in step. SERS-based chip techniques and related materials are widely used in biological analyses.[3-5]

In this study, identification and quantification of bacteria are performed by SERS with Ag nanoparticles. The negative charge of the bacterial cell wall was attractive to stably adsorb Ag nanoparticles, which were reduced to hydroxylamine, on the cell wall as shown in Figure 1.

SERS spectra of various Gram-positive bacteria were obtained from the adsorbed Ag nanoparticles as shown in Figure 2. Each bacteria can be identified from the SERS spectra through the relative intensity of the bands at around 660 and 730  $\text{cm}^{-1}$ . Details on analysis of bacteria based on SERS will be discussed in this presentation.

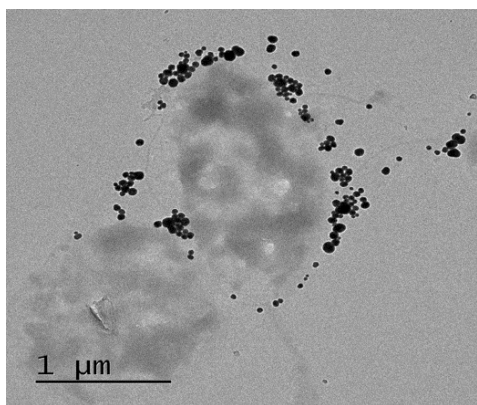


**Figure 1.** FE-TEM image of Ag nanoparticles absorbed on the *Bacillus cereus* cell wall.

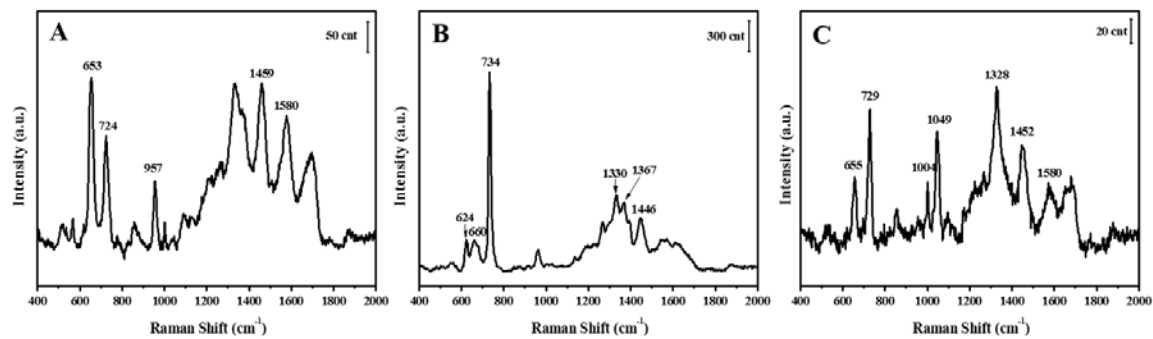


**Figure 2.** SERS spectra of *Bacillus subtilis* (A), *Bacillus cereus* (B) and *Bacillus thuringiensis* (C).

- [1] Ivnitski, D.; Abdel-Hamid, I.; Atanasov, P.; Wilkins, E. *Biosens. Bioelectron.* **1999**, *14*, 599-624.
- [2] Thiramanas, R.; Laocharoensuk, R.; *Microchim. Acta*, **2016**, *183*, 389-396.
- [3] Mahajan, S.; Richardson, J.; Brown, T.; Bartlett, P. N. *J. Am. Chem. Soc.* **2008**, *130*, 15589-15601.
- [4] Jarvis, R. M.; Goodacre, R. *Anal. Chem.* **2004**, *76*, 40-47.
- [5] Cui, L.; Yao, M.; Ren, B.; Zhang, K. S. *Anal. Chem.* **2011**, *83*, 1709-12716.

# Development of Quantitative Analysis for Monitoring Saccharification Process Using Raman Spectroscopy

Anggara Mahardika<sup>1,2</sup>, Bibin B. Andriana<sup>1</sup>, Hiroko Matsuyoshi<sup>1</sup>, AB Susanto<sup>3</sup>, Hidetoshi Sato<sup>1\*</sup>

<sup>1</sup>*Department of Biomedical Chemistry, School of Science and Technology, Kwansei Gakuin University, Japan*

<sup>2</sup>*Department of Electrical Engineering, Harapan Bersama Polytechnic, Indonesia*

<sup>3</sup>*Department of marine science, School of Fishery and Marine Science, Diponegoro University, Indonesia*

\* *hidesato@kwansei.ac.jp*

**Summary:** The main Purpose of this study is to develop a quantitative analysis for monitoring saccharification process using Raman spectroscopy. The result, Raman spectroscopy and PLS analysis was succeeded to estimate the concentration of every enzymatic reaction component (starch, maltose, and glucose) with high regression model ( $R^2$ ) up to 0.9.

**Introduction:** Enzyme plays an important role for a catalytic tool in many industrial productions, such as liquor, vinegar, soy sauce, etc. Sugar production through enzymatic reaction has a large segment of the food and beverage industry (1). Hence, a quantitative analysis which has fast, accurate and economic become high demand in industrial for monitoring their production. Conventional methods which generally analyze reducing sugar are difficult to determine glucose and maltose independently. In this study, a method to monitor the reaction quantitatively was developed based on Raman spectroscopy.

**Methods:** Enzyme  $\alpha$ -amylase (EC 3.2.1.1) from *Aspergillus oryzae* purchased from Sigma-Aldrich were uses to make enzymatic reaction model. The enzymatic reaction was conducted at room temperature in the phosphate buffer pH 7.0. The samples were taken every 15 minutes and were then analyzed using dinitrosalicylic acid (DNSA) reagent (Miller method) and Raman Spectroscopy. Homemade confocal Raman microscope Olympus IX73 with 785nm excitation laser were employed to monitoring the enzymatic reaction.

**Results and Discussion:** The starch is dissolved into smaller sugar by hydrolytic cleavage with  $\alpha$ -amylase. The enzymatic reaction takes place randomly on starch, polysaccharide and produces oligosaccharide, maltose, and glucose. Raman spectra of aqueous solutions of phosphate buffer (a), starch (b), D-glucose (c), and maltose (d) are shown in Figure 1. The spectra of saccharides similarly have no band in the frequency region higher than  $1500\text{ cm}^{-1}$  because they do not have any carbonyl group nor double bond. Stefan et al (2) suggested that range at  $500\text{-}600\text{ cm}^{-1}$  is well described of sugar species. The bands below  $600\text{ cm}^{-1}$  are especially characteristic to identify these saccharide species; bands at  $519$  and  $554\text{ cm}^{-1}$  in maltose, those at  $519$  and  $541\text{ cm}^{-1}$  in D-glucose, and a band at  $479\text{ cm}^{-1}$  in starch. PLS analysis of model calibration curve mixing known concentration of starch, glucose, and maltose could be determining of each concentration with predicted R-square up to 0,88 for starch and maltose, those 0,9 for glucose. The concentration of each enzymatic components was successfully estimated through this model calibration curve. Figure 2 show the estimation of each component measured by Raman spectroscopy. For the comparison, reducing sugar measured by DNSA reagent is show in figure 3. In both result show similar curves in the reaction rate, suggesting that the prediction models work correctly in the real  $\alpha$ -amylase reaction. The value of sugar concentration gets increasing at fist 15 min while starch was decreased dramatically.

**Conclusion.** The results in this study was demonstrated that the PLSR analysis with Raman spectroscopy is a powerful method for quantitative analysis of saccharides.

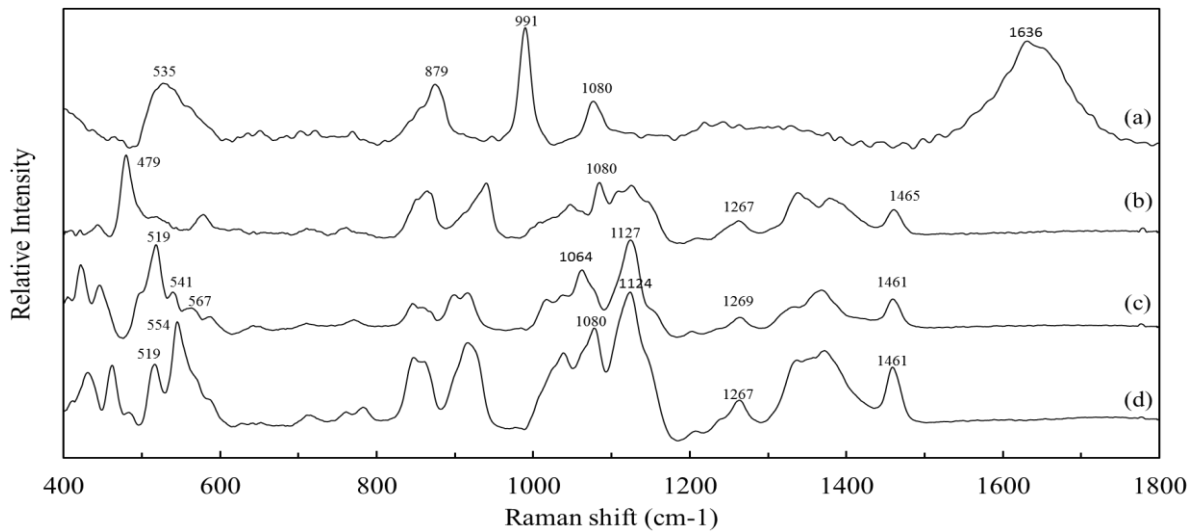


Figure 1. Raman spectra of aqueous solutions of phosphate buffer (a), starch (b), D-glucose (c), and maltose (d).

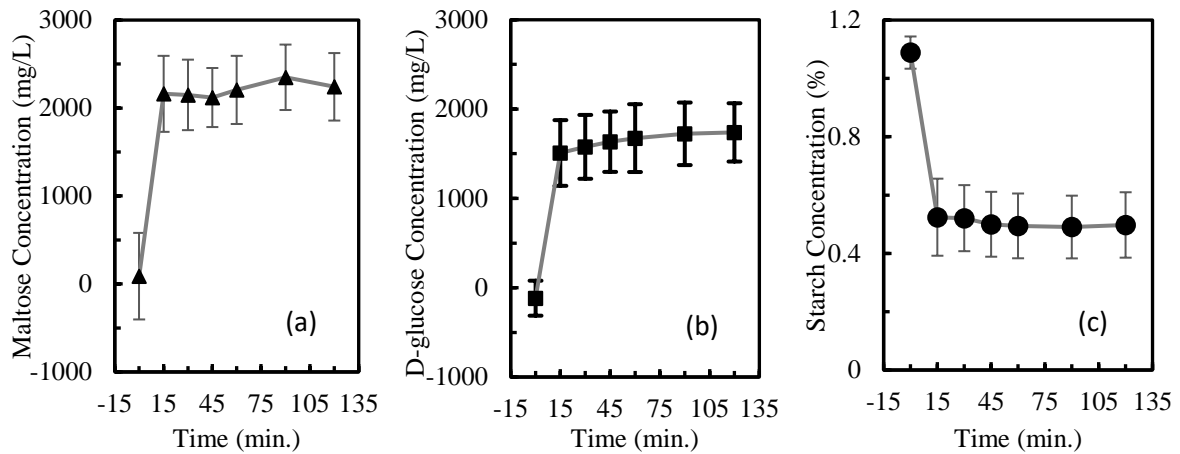


Figure 2. Predicted concentration of maltose (a), glucose (b) and starch (c) by Raman Spectroscopy.

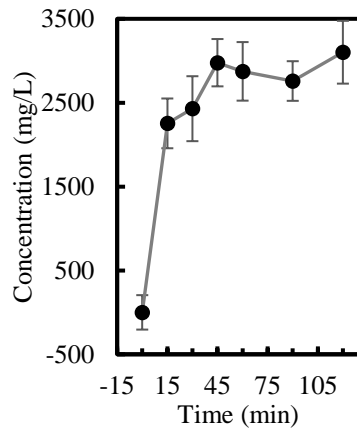


Figure 3. Sugar concentration measured by DNSA reagent.

## References

- (1) Jan Šugar and Petr Bouř. 2016. Quantitative analysis of sugar composition in Honey using 532-nm excitation Raman and Raman optical activity spectra. *J. Raman Spectrosc.*
- (2) Stefan Söderholm et al. 2016. Raman Spectra of Fructose and Glucose in the Amorphous and Crystalline States. *J. Raman Spectrosc.*

## Trace detection of isotopic CH<sub>4</sub> in ambient air using cavity ring-down spectroscopy coupled with an external-cavity quantum cascade laser

Abhijit Maity<sup>1</sup>, Mithun Pal<sup>1</sup>, Manik Pradhan<sup>1,\*</sup>

<sup>1</sup> *Department of Chemical, Biological and Macro-molecular Sciences, S. N. Bose National Centre for Basic Sciences, Block-JD, Sector-III, Salt Lake, Kolkata-700106*

\*corresponding: [manik.pradhan@bose.res.in](mailto:manik.pradhan@bose.res.in)

A high-resolution cavity ring-down spectroscopic (CRDS) system based on a continuous wave (cw) mode-hop-free (MHF) external-cavity quantum cascade laser (EC-QCL) operating at  $\lambda \sim 7.5 \mu\text{m}$  has been developed for ultrasensitive detection of isotopes of methane (CH<sub>4</sub>). We report the performance of the high-resolution EC-QCL based CRDS instrument by probing the fundamental vibrational lines, arising from symmetric bending, of CH<sub>4</sub> isotopes at around 7.5  $\mu\text{m}$ . A noise-equivalent absorption coefficient of  $2.50 \times 10^{-9} \text{ cm}^{-1} \text{ Hz}^{-1/2}$  was achieved based on an empty cavity ring-down time of  $\tau_0 \sim 14 \mu\text{s}$  and standard deviation of  $\sim 1\%$  with averaging of ten ring-down times. The CRDS sensor demonstrates the advantages of measuring parts per billion (ppb) concentrations of CH<sub>4</sub> isotopes in any ambient air samples with ultrahigh sensitivity and specificity. The CRDS system could also be generalized to measure simultaneously many other trace molecular species for medical diagnostics (Human breath analysis) purposes, as well as for monitoring the atmospheric phenomena within the broad tuning range of the cw EC-QCL.

# Chemical Composition of Archeological Materials Collected from a Maya Royal Burial and the Cemetery of the Chancay culture. FTIR and Raman Spectroscopy Studies.

Agnieszka Garbacz<sup>1,2</sup>, Lukasz Majchrzak<sup>2</sup>, Pieter van Dalen Luna<sup>3</sup>, Jarosław Żrałka<sup>2</sup>,  
Kamilla Malek<sup>1\*</sup>

<sup>1</sup>*Faculty of Chemistry, Jagiellonian University, Ingardena 3, 30-060 Krakow, Poland*

<sup>2</sup>*Institute of Archeology, Jagiellonian University, Golebia 11, Krakow, Poland*

<sup>3</sup>*Museo de Arqueología y Antropología, Universidad Nacional Mayor de San Marcos, Lima, Peru*

\**kamilla.malek@uj.edu.pl*

Infrared and Raman spectroscopy is in many ways a very attractive analytical method for archeology due to its non-destructive nature, rapid collection time as well as the ability of the identification of chemical composition on micro-samples. This work was focused on a spectroscopic analysis of unidentified materials collected from a royal burial at Nakum, Guatemala (from the Classic period of the Maya culture, 6th century AD) and samples of mummified human bodies from the Central Andean region in Peru (the Chancay culture, ca. 900 - 1572 AD).

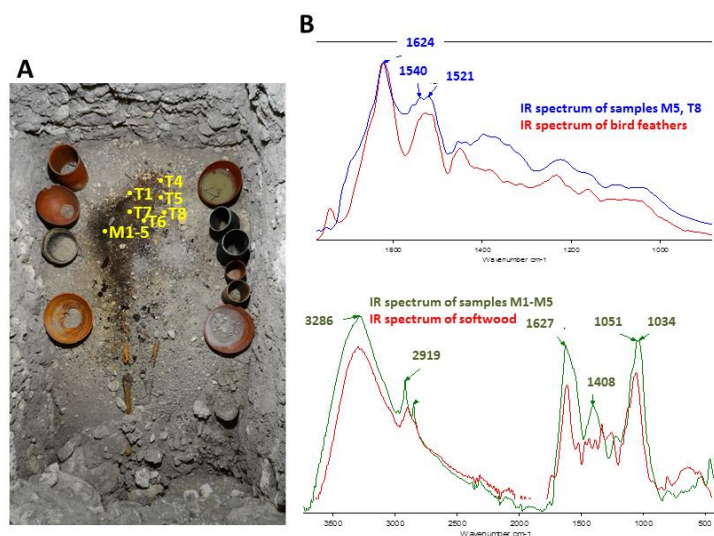


**Figure 1.** (A) A photograph of the Nakum tomb with marked locations of sampling and exemplary ATR FTIR spectra (B) collected from samples marked in (A).

The Nakum tomb can be dated to the beginning of the 6th century A.D. and it likely represents a resting place for one of the local kings (Fig. 1A). Despite the fact that the skeleton remains and grave goods (excluding ceramics) survived badly, ATR FTIR spectra exhibited a plethora of information that confirmed some indications from other archeological investigations of the Maya culture. For instance, the presence of a protein material of spectral signature typical for bird features suggested that the ruler was buried

in a magnificent costume decorated with bird feathers (Fig. 2B). In addition, we identified the material rich in cellulose and lignins which proved the presence of wooden elements in the inventory grave, probably in the form of wooden statuettes.

The second group of samples was archeological materials collected from mummies of the Chancay culture in Peru, Fig. 2B. Here, we investigated methods of the body treatment and the preparation of tattoos practiced by the Chancay society. We observed that significant difference in the color and structure of mummified bodies correlates well with the chemical composition revealed from FTIR spectra. First of all, we found IR markers of the process of the skin degradation which depends on the type of skin treatment, Fig. 2B. We suggested that two types of mummification were used by the Chancay societies, including the drying process and the use of balsamic products. Raman analysis of tattooed skin suggested the use of soak mixed with oil base.

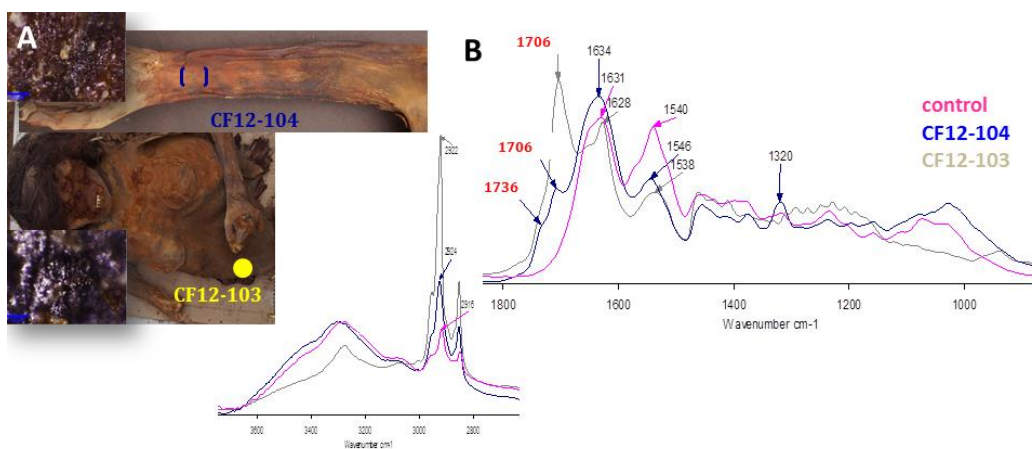


**Figure 2.** (A) A photograph of the Peruvian mummified human bodies with marked locations of sampling (insets illustrate skin surface, magnification 100×) and comparison of FTIR spectra (B) collected from samples marked in (A) with control.

The vibrational analysis of the archaeological samples studied here provided extremely useful guidelines for further archeological interpretation. Proven fact that FTIR and Raman microscopy is an excellent tool to study the composition of archaeological materials, regardless of its size and state of preservation as shown in Fig. 1A and Fig. 2A. In spite of these important factors in any physico-chemical analysis of archeological artefacts, in both cases vibrational spectroscopy perfectly proved itself as a support for a goal-oriented analysis and expanded our knowledge about the past.

Materials from the Nakum tomb were collected during archaeological excavations carried out in the frame of the Nakum Archaeological Project directed by J. Žralka and Wiesław Koszkuł (Jagiellonian University) and co-directed by Juan Luis Velásquez (Guatemala) while mummified human bodies originated from excavations conducted by Dr. Pieter Van Dalen (Universidad Nacional Mayor de San Marcos) in collaboration with L. Majchrzak (Jagiellonian University).

# Recent developments in vibrational spectroscopic analysis of aligned semiconducting single-walled carbon nanotubes

Matthew Meyer<sup>1</sup>, Amir Mashal<sup>1</sup>, Nathaniel S. Safron<sup>1</sup>, Katherine Jinkins<sup>2</sup>, Michael S. Arnold<sup>2</sup>

<sup>1</sup>ThermoFisher Scientific, Madison, WI

<sup>2</sup>Department of Materials Science and Engineering, University of Wisconsin-Madison

Semiconducting single walled carbon nanotubes (s-SWCNTs) are cylinder-shaped molecular wires with distinct electrical properties. Due to these electrical properties, s-SWCNTs are viewed as a critical technology for the future of materials science research. Greater use of vibrational spectroscopies is proving beneficial for efficient characterization of carbon nanotube films. We present the results of how polarized Raman imaging, UV-VIS-NIR absorption and advanced Fourier transform infrared spectroscopy can be used to effectively advance research in high performing electronic devices.

The s-SWCNT films studied were prepared via a form of floating evaporative self-assembly (FESA).<sup>1</sup> Vibrational spectroscopy was conducted on the FESA fabricated s-SWCNTs. One of the most promising techniques for analysis of FESA fabricated s-SWCNT films is polarized Raman imaging.<sup>2</sup> Polarized Raman imaging analysis produced an average optical anisotropy of up to 54, signifying well-aligned s-SWCNT films.<sup>3</sup> An orientation Raman image, based on the optical anisotropy values, produces a visual representation for the spatial distribution of the alignment in the s-SWCNT film. This polarized Raman imaging technique represents an important step towards efficiently characterizing large area alignment in aligned CNT films.

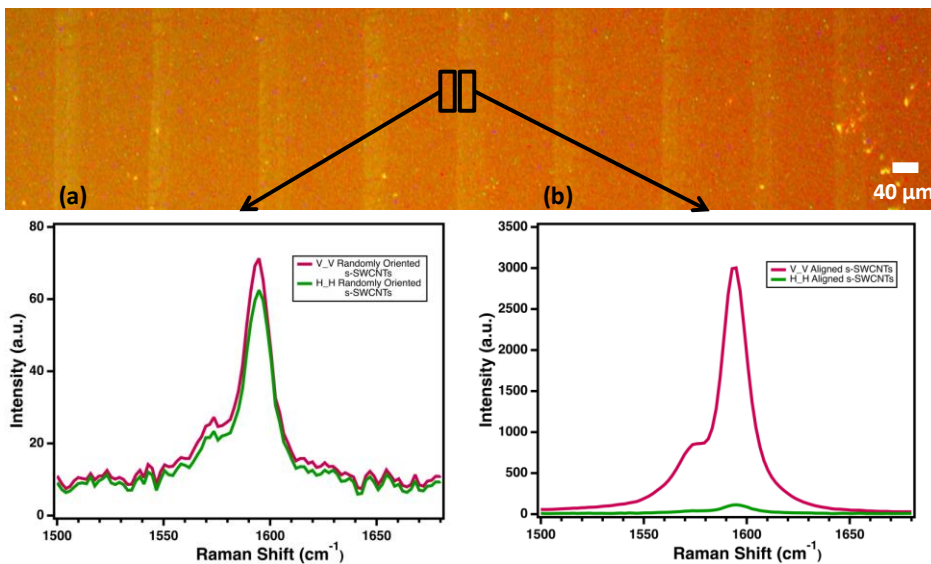


**Figure 1.** Polarization Raman spectrum of the G-band intensity as a function of s-SWCNT orientation and polarization orientation (V\_V or H\_H) utilizing automated

polarization. (a) G-band intensity of randomly oriented s-SWCNTs with V\_V and H\_H polarization orientations. The weak overall intensity and optical anisotropy indicates random alignment. (b) G-band intensity of aligned s-SWCNTs with V\_V and H\_H polarization orientations. The strong signal and high optical anisotropy ( $\sim 22$ ) indicate exceptional alignment in the s-SWCNTs.

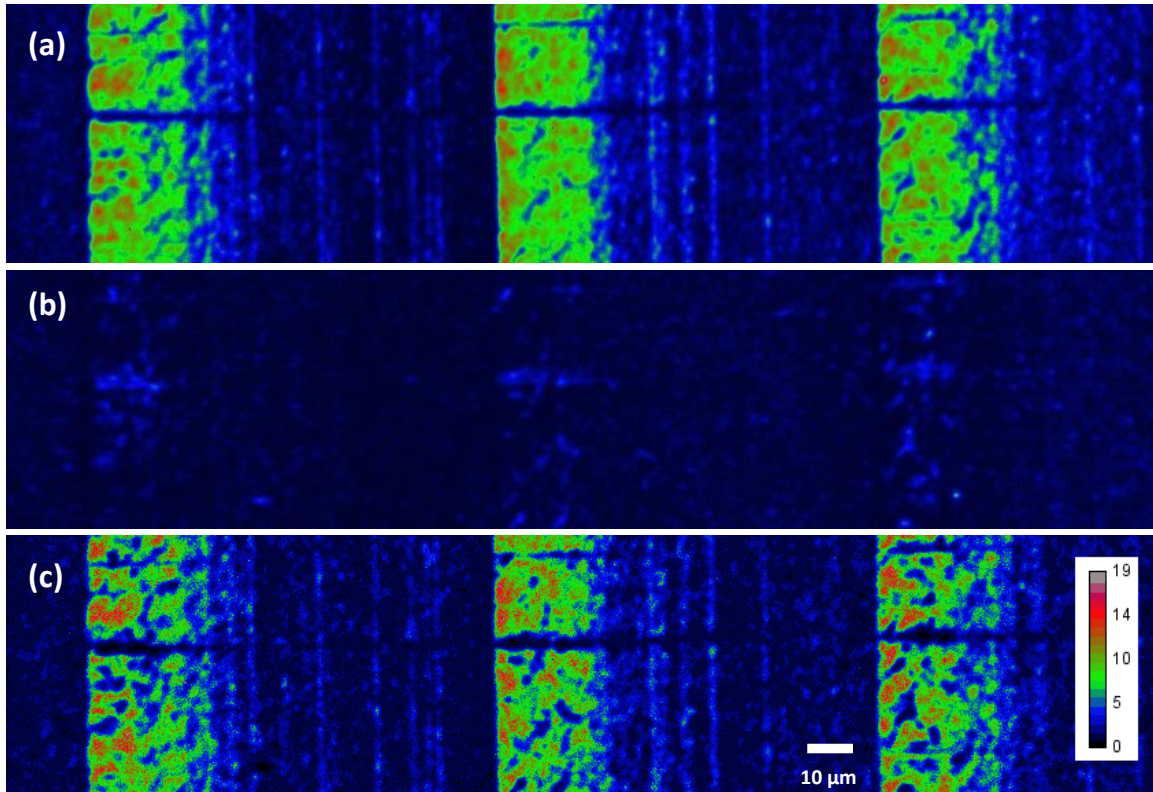


**Figure 2.** Polarized Raman imaging on arrays of s-SWCNTs with various polarization orientations. (a) Laser polarization aligned with s-SWCNT axis (V\_V). (b) Laser polarization perpendicular to s-SWCNT axis (H\_H). (c) Orientation image produced by dividing the spectroscopic arrays from (a) and (b) polarization images. The areas of higher intensity represent areas of well aligned s-SWCNTs whereas areas of low intensity represent areas of randomly oriented s-SWCNTs.

- [1] Joo, Y.; Brady, G.; Arnold, M.; Gopalan, P. *Langmuir*, 2014, 30, 3460-3466.
- [2] Mashal, A.; Wieboldt, D.; Jinkins, K.; Arnold, M. *Spectroscopy Now*, 2016, 31, 36-44.
- [3] Cao, Q.; Han, S. J.; Tulevski, G. S.; Zhu, Y.; Lu, D. D.; Haensch, W. *Nature Nanotechnology*, 2013, 8, 180-186.

## Evaluation of Different Chemometrics Methods associated with Raman Mapping to Study Miscibility of Excipients in Lipid-Based Pharmaceutical Formulations

Mitsutake, Hery<sup>1,\*</sup>, Castro, Simone R. de<sup>2</sup>, Paula, Eneida de<sup>2</sup>, Poppi, Ronei J.<sup>1</sup>, Rutledge, Douglas N.<sup>3</sup>, Breitzkreitz, Márcia C.<sup>1</sup>

<sup>1</sup> *Chemistry Institute, State University of Campinas (UNICAMP), Campinas SP, Brazil.  
Zip code 13083-970*

<sup>2</sup> *Institute of Biology, State University of Campinas (UNICAMP), Campinas SP, Brazil,  
Zip Code 13083-862*

<sup>3</sup> *UMR Genial, AgroParisTech, INRA, Université Paris-Saclay, 91300 Massy, France  
\*herymitsutake@gmail.com*

It is estimated nowadays that 40 to 70% of active pharmaceutical ingredients (API) are poorly water-soluble, which may result in erratic bioavailability. In order to overcome this problem, lipid-based formulations are becoming more widely used, since they improve *in vitro* solubility and *in vivo* bioavailability. Solid, semi-solid and liquid lipids, surfactants and solvents can be used for pharmaceutical development of many different types of lipid-based formulations. However, formulations that seem promising during preparation often present stability issues over the time, with eventual phase separation during the stability study. In this context, hyperspectral Raman imaging for evaluating microscopic miscibility of the excipients during pre-formulation can be very helpful and may allow early identification of situations that could lead to later stability problems. Multivariate chemometrics methods can facilitate the extraction of all of the information in the hyperspectral images and therefore provide more accurate chemical images than univariate approach. There are several different chemometrics methods available for this spectral treatment, however, for pre-formulation screening purposes, it is interesting to select a fast method that does not require many samples for calibration. Some methods that fulfil this criterion are: Principal Components Analysis (PCA), Classical Least Squares (CLS), Multivariate Curve Resolution (MCR), Independent Components Analysis (ICA) and Common Components Analysis (CCA), each of them with different principles and outcomes.

The aim of this work is to understand and compare the outcomes of the five abovementioned chemometrics methods when applied to Raman spectral images of two lipid-based formulations: Cetyl Palmitate/Transcutol<sup>®</sup> and poly(ethylene glycol - PEG 6000)/Tween 80<sup>®</sup> both in the proportions of 70:30 (%w/w). These samples were selected for this study based on the spatial distribution of the compounds (the first is very heterogeneous and the latter is very homogeneous) and also because they present significant differences in the pure spectra of the compounds, which will allow the evaluation of loadings/signals extracted by each of the chemometrics methods. The mixtures were prepared by heating the solid excipients above their melting point and adding the liquid excipients while stirring until visually homogeneous mixtures were obtained. The samples were cooled to room temperature in an aluminum cell and an area of  $1.95 \times 1.95 \text{ mm}^2$  was mapped using a Raman Station 400 spectrometer (Perkin Elmer). The exposition time was 3s/pixel, 2 expositions, pixel size was 50  $\mu\text{m}$  and spectral range

3200-600  $\text{cm}^{-1}$ , with a resolution of 4  $\text{cm}^{-1}$ . The data matrix was augmented with 40 spectra of each pure excipient for all the methods. Spectra were corrected by smoothing, weighted least squares baseline and unit length normalization and the final spectral range chosen was set at 1804-724  $\text{cm}^{-1}$ . The criteria for the performance evaluation of the models were the absolute error of the predicted average concentrations of excipients, the complementarity of the maps and the recovered spectra. Calculations were carried out in Matlab environment (version 8.3.0, MathWorks), the JADE and 'ComDim' algorithms were used for ICA and CCA, respectively. For MCR calculations, MCR\_toolbox version 2.0 was used. For comparison of the concentration maps, the scores and predicted values were normalized between 1 and 100. Data were mean centered for PCA calculations. The first method evaluated was PCA. The variance captured by the first PC was 94.82 and 85.72% for Cetyl Palmitate/Transcutol<sup>®</sup> and PEG 6000/Tween 80<sup>®</sup>, respectively. The loadings in the first PC described the difference between the two excipient spectra and not the spectrum of either of the pure compounds, i.e., PCA provides a *contrast* image and not a separate image for each of compounds. The CLS method is supposed to provide accurate results in the absence of interactions between the compounds, however in the case of interactions, MCR or ICA are more suitable and therefore might be preferable. In order to fairly compare the performance of MCR with ICA, MCR was used as a "blind source method" and the 'Pure' function of the MCR\_toolbox 2.0 was used to estimate the pure spectra in the data matrix. MCR recovered well the spectra in the heterogeneous sample, however, in the homogeneous sample the rotational ambiguity problem was clearly observed. On the other hand, ICA recovered the spectrum of each excipient in both samples, using 2 ICs, without rotational ambiguity. The CCA method recovered the average spectrum of the sample in the first CC, and the difference between the spectra of the excipients in the second component, in a similar manner for the two mixtures. This implies that it recovers the most common signal in the pixels (the average) as the first component while the second component is the contrast between the excipients, which provides the desired chemical information similarly to PCA. Figure 1 shows the maps of two mixtures obtained by the ICA method.

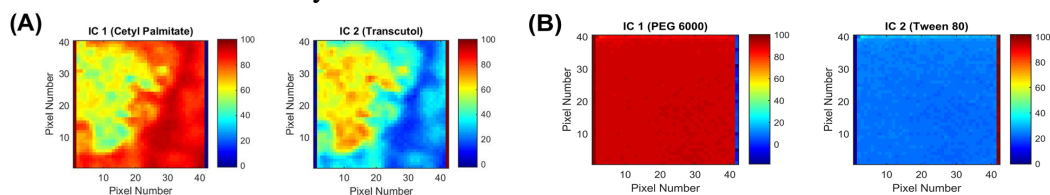


**Figure 1.** Concentration maps of (A) Cetyl Palmitate/Transcutol<sup>®</sup> and (B) PEG 6000/Tween 80<sup>®</sup> obtained using the ICA method.

The heterogeneous formulation was instable and exhibited phase separation after 60 days, and the homogeneous formulation was stable for more than one year. All methods showed to be adequate for the miscibility pre-formulation screening study, however different information is obtained by each method. The heterogeneous sample is easier to deal with, but difficulties appeared for the homogeneous sample due to the lack of variability among the pixels. In this case, ICA was superior to MCR because it does not present rotational ambiguity. Additional studies are being conducted using systems that present different spatial variabilities and higher similarity in the pure spectra of the compounds.

## Study of Hydrogen-bonding Structure in Deep Eutectic Solvents composed of Li salt and Acetamide by Near Infrared Spectroscopy.

Yusuke Morisawa<sup>1</sup>, Kazutaka Nishikido<sup>1</sup>, Ichimaru Morita<sup>1,\*</sup>

<sup>1</sup> School of Science and Engineering, Kindai University, 3-4-1 Kowakae, Higashi-Osaka, Osaka, 577-8502, Japan

\* [morisawa@chem.kindai.ac.jp](mailto:morisawa@chem.kindai.ac.jp)

Deep eutectic solvents (DESs) are liquid mixtures between an electrolyte salt and a neutral molecule which plays as hydrogen bonding donor. For example, a mixture of lithium nitrate and acetamide in a ratio of 1:4 become a liquid in the room temperature although both components are solid in the room temperature. In this case, concentration of the electrolyte, [LiNO<sub>3</sub>], is about 4 mol dm<sup>-3</sup> which is same as those of ionic liquids. Thus, properties of DESs are similar to ionic liquids such as high viscosity, low volatility, and incombustibility. Hydrogen-bonding (HB) in ionic liquids got keen interest since it plays an important role of properties of the liquid. Thus an investigation of HB structure in the DES is needed to know how the electrolyte and HB donor interact in the liquids. Few researches studied traditional vibrational spectra, such as FT-IR, and Raman spectra, for the DES composed of Li salt, although these spectra often used for investigation of intermolecular interaction in HB system. As to these DES, deep overlap between several HB states and fermi resonance with 1<sup>st</sup> overtone of amide I makes hard to analyze the IR spectra in the X-H stretching region. Additionally, intensity enhancement by HB interaction for fundamental N-H stretching obstructs estimation of the ratio of the HB states. To resolve these we analyzed NIR spectra. In the present study, composition-ratio and temperature dependences of NIR and MIR spectra were measured for DES composed of Li salt and acetamide.

As to DES of acetamide and LiNO<sub>3</sub>, absorption bands for 1<sup>st</sup> overtone of CH<sub>3</sub> were observed in 6100-5700 cm<sup>-1</sup> (Figure 1). In the fundamental region, bands for CH<sub>3</sub> stretching are obscured by a HB component of NH<sub>2</sub> stretching. Thanks to removal of intensity enhancement by HB interaction in NH<sub>2</sub> stretching in 1<sup>st</sup> overtone, CH<sub>3</sub> band can be successfully observed. Since the CH<sub>3</sub> bands were shifted by composition ratio but not by temperature from 25 to 85 °C, the shift may originated from not HB with the anion but from strong interaction such as Li---O=C coordination .

For the 1<sup>st</sup> overtone of NH<sub>2</sub>, broad features were observed in the region of 6100 to 7100 cm<sup>-1</sup> (Figure 2). As shown in Fig. 2(b) the 1<sup>st</sup> overtone of NH<sub>2</sub> of DESs (molar fraction  $x_{\text{LiNO}_3} = 10, 20, 25 \%$ ) is similar to the neat acetamide at 85 °C which is in the liquid state. Broad tail observed in the region of 6100 to 6500 cm<sup>-1</sup> can be assigned to NH<sub>2</sub> in the HB between acetamides. The two major band observed in 6600 and 6700 cm<sup>-1</sup> were shifted by temperature from 25 to 85 °C significantly but little by composition ratio. Intensity ratio of these band changed by temperature. A shoulder band seen in 6900 cm<sup>-1</sup> shifts both temperature and composition ratio. As the result, there are at least 3 components in the region of 6500 to 7100 cm<sup>-1</sup>. We have investigated for the DES involved different electrolytes such as LiCF<sub>3</sub>SO<sub>3</sub>, LiBF<sub>4</sub>. Peak position and band width of the bands in NH<sub>2</sub>

are changed among different anion. We will discuss the difference of HB state among these DESs.

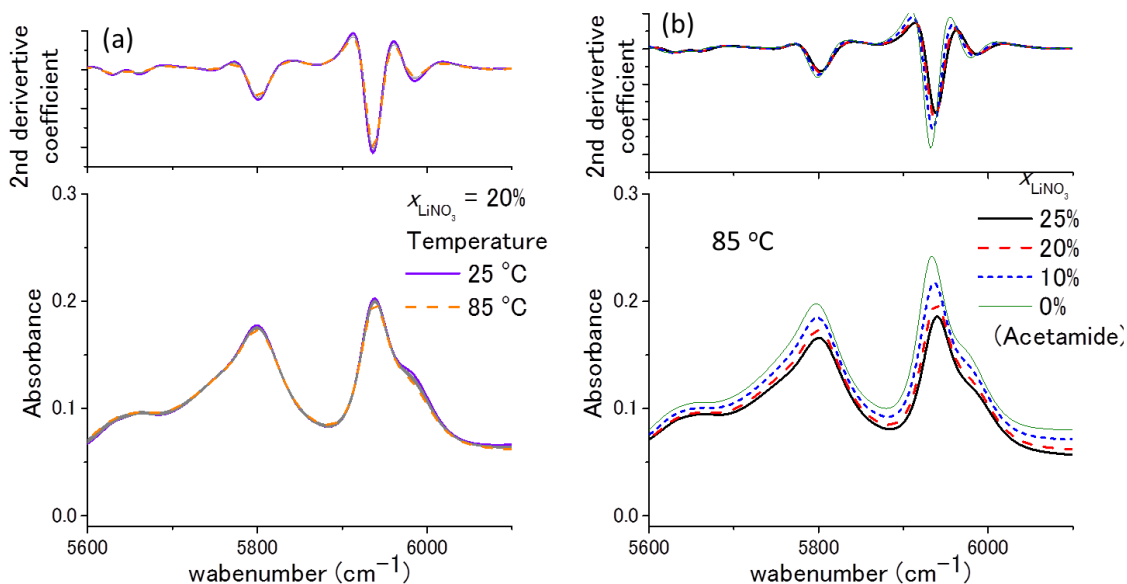


**Figure 1.** Absorption spectra for 1<sup>st</sup> overtone of CH<sub>3</sub> in the region of 6100-5700 cm<sup>-1</sup> with regard to (a) temperature dependence for the DES of molar fraction,  $x_{\text{LiNO}_3}=20\%$  from 25 to 85 °C, and (b) composition dependence at 85 °C from neat acetamide to  $x_{\text{LiNO}_3}=25\%$ .

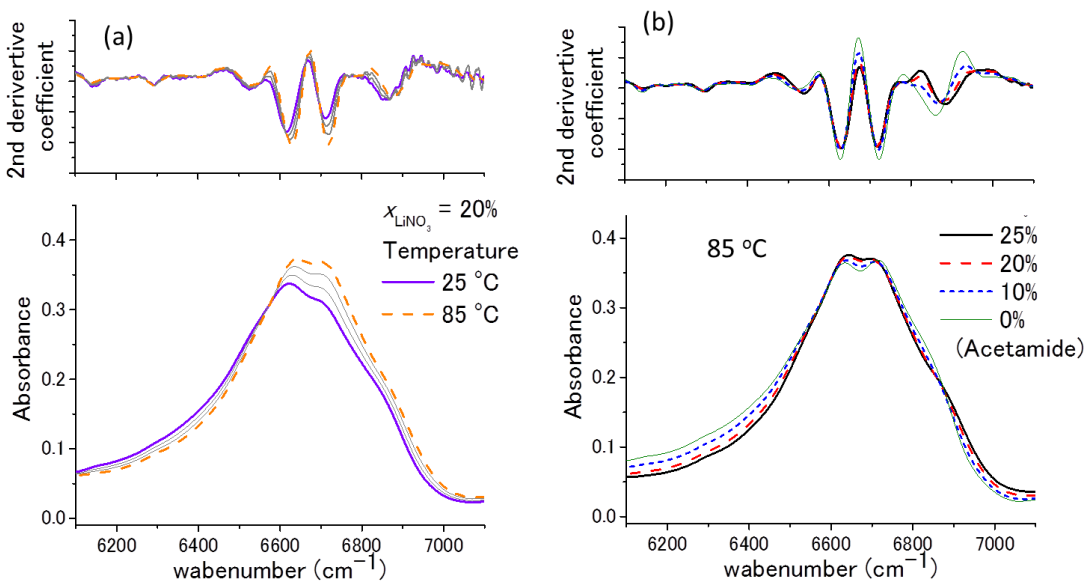


**Figure 2.** Absorption spectra for 1<sup>st</sup> overtone of NH<sub>2</sub> in the region of 6100-7100 cm<sup>-1</sup> with regard to (a) temperature dependence for the DES of molar fraction,  $x_{\text{LiNO}_3}=20\%$  from 25 to 85 °C, and (b) composition dependence at 85 °C from neat acetamide to  $x_{\text{LiNO}_3}=25\%$ .

## Detection and quantification of adulterants in coconut oil using Raman spectroscopy and Multivariate Curve Resolution.

Marina D. G. Neves<sup>1,\*</sup>, Ronei J. Poppi<sup>1</sup>

<sup>1</sup>*Institute of Chemistry, University of Campinas, P.O. BOX 6154, 13081-970, Campinas, Brazil*

*\*marina.de.gea.n@gmail.com*

Fats and oils have been target to adulteration since long time ago. The adulteration may cause unfair competition between oils [1]. Coconut oils are widely used in food and factory, presenting a potential functional food, since it is saturated and rich in small and medium chain fatty acids opposed to other saturated fats like animal's fat [2]. Small and medium chain triglycerides, after ingested, are readily burned and this process leaves fatty deposits in the tissues [3]. Coconut oil has also biologic activist like nutraceutical/health benefits. In the Market, your price is about 10-20 times higher than common plant oils like sunflower, soybean, corn or palm. Several analytical methods have been developed for detection of adulteration in oils such as DSC (differential scanning calorimetry), chromatography, and others, but some methods may spend a lot of solvents and destruct the samples. In this way, is of outmost importance the development of analytical methodologies for detection and quantification of such frauds. Raman spectroscopy is a nondestructive method, without use of solvents for analysis. In this work, Raman spectroscopy in conjunction to multivariate curve resolution was applied to detection and quantification of adulterants in coconut oil. The spectra were obtained using a dispersive spectrometer Raman Station 400F, from Perkin Elmer, equipped with a charge-coupled-device (CCD) detector operated at -50 °C and a diode laser of 785 nm and 250 mW (in source). The data acquisitions were accomplished with 30 seconds of laser exposition and 8 scans for each sample. The spectra were obtained in the range of 3200 to 200  $\text{cm}^{-1}$  with a resolution of 2  $\text{cm}^{-1}$ . The spectra were obtained directly in glass vials. After this, the spectra were smoothed and normalized and the MCR-ALS (multivariate curve resolution with alternating least squares) was used to detect and quantify adulteration in coconut oil. In MCR calculations it was used the constraints: nonnegativity, both in concentration in the spectral profile, and correlation. Control chart was built from MCR results for identification of pure and adulterated coconut oils. It was used 17 coconut reference samples and 135 coconut adulterated oils. Soybean, sunflower, corn, palm, mineral oil, and others, had been used as adulterants in this work. For quantification studies, it was built calibration curve models, with 6 samples, for coconut oil with each adulterant. The pure coconut oil was adulterated increased by 2% in the range of 2-30% for each oil. Nine validations samples were used in each regression model. The predicted values for concentrations showed absolute error generally less than 2%. The Figure 1 shows a scheme of the procedure, initializing with different samples, the spectra of all samples and the MCR models developed.

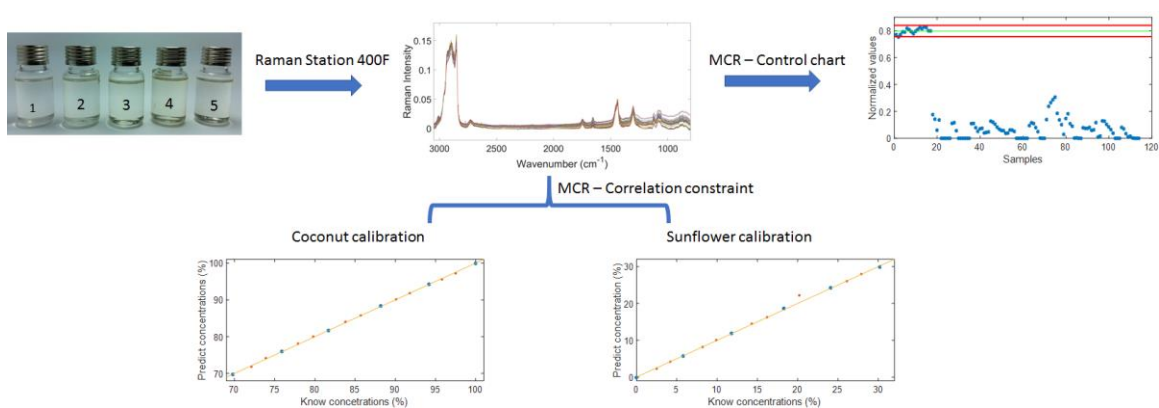


**Figure 1.** Representative scheme for the samples analyzed by Raman spectroscopy and the control chart and calibration models for quantify purity of coconut oil and adulteration (sunflower adulteration in this case). Calibrations samples are showed in blue and validation in red.

The red lines on the control chart in Figure 1 indicates the range of confidence that a sample should be to be denominated pure. Outside this range, samples are considered non-pure. Pure coconut oil samples, used in the control chart, appear inside the red lines, the other adulterated oils are out of this range. The spectra were cut from 800-1800 cm<sup>-1</sup> for developing the calibration models. It was quantified the percentage of coconut in coconut oil, that is, the percentage of purity, and also the percentage of adulterant mixed with coconut oil. The fit for regression was 0.99 for both calibrations. The use of Raman spectroscopy in conjunction to MCR proved to be a suitable tool to rapid detection and quantification adulteration in coconut oils.

[1] Rohman, A.; Che Man, Y. B. *Food Chemistry*. **2011**, *129*, 583–588.

[2] Marina, A.M.; Che Man, Y. B.; Amin, I. *Trends Food Sci Tech*. **2009**, *20*, 481–487.

[3] Marten, B.; Pfeuffer, M.; Schrezenmeir, J. *Int Dairy J*. **2006**, *16*, 1374–1382.

## **Determination of mebendazole polymorphs in pharmaceutical raw materials using portable and benchtop Raman spectrometers.**

Eduardo M. Paiva<sup>1\*</sup>, Vitor H. da Silva<sup>1</sup>, Ronei J. Poppi<sup>2</sup>, Jarbas J. R. Rohwedder<sup>2</sup>,  
Claudete F. Pereira<sup>1</sup>

<sup>1</sup>*Department of Fundamental Chemistry, Federal University of Pernambuco, Recife, PE, Brazil.*

<sup>2</sup>*Institute of Chemistry, State University of Campinas, Campinas, SP, Brazil.*  
*\*[eduardomaiapaiva@hotmail.com](mailto:eduardomaiapaiva@hotmail.com)*

Mebendazole (MBZ) is an anthelmintic drug, essential to human health. The World Health Organization estimates one quarter of the world population has parasitic infestations, addressed by this drug. This medicine is easy to administer, has a low cost and wide spectrum. MBZ exists in three polymorphic forms (A, B and C). Among these polymorphs, Form C is preferred by the pharmaceutical industry for the production of drugs, since it does not have the disadvantages of Form A, which is ineffective when it corresponds to more than 30% of the formulation; or Form B which has the highest toxicity. Although Forms B and C are metastable, all three polymorphs of MBZ are found at room temperature. For this reason, scientific studies have recorded the existence of the three polymorphs in the marketed drug [1]. Therefore, it is important to develop analytical methods to identify and quantify MBZ polymorphs in raw materials used to produce the commercial drugs.

The main technique used for polymorphs analysis is X-Ray powder diffraction (XRPD). Alternatively, vibrational spectroscopic techniques have been used to identify the different polymorphs in an indirect way. This is because many active pharmaceutical ingredients (API) present hydrogen bonds which have different environments in each crystalline form, presenting an energy displacement of the band on a spectrum [1-2]. Among these techniques, Raman spectroscopy has been increasingly used since it is more suitable for quality control analysis than XRPD due such things as employment of in-line probes, portable instruments, few or no requirements for sample preparation, and no sample destruction. We have developed a quantitative multivariate method for determination of MBZ polymorphs in raw materials, employing both portable and benchtop Raman spectrometers.

Powder mixtures were prepared, based on a mixture design, containing polymorphs A and C in concentrations ranging from 0 to 100% (w/w) and polymorph B from 0 to 30% (w/w). Tablets of the powder mixtures were prepared. Two Raman spectrometers were employed: (1) a portable B&W Tek TacticID-GP, which uses a 785 nm diode laser with 300 mW, 9 cm<sup>-1</sup> of resolution, spectral range from 176 to 1900 cm<sup>-1</sup> and 80 μm of spot size; (2) a benchtop Perkin-Elmer RamanStation 400F, with a 785 nm diode laser, 350 mW, 4 cm<sup>-1</sup> of resolution, spectral range of 176 to 1900 cm<sup>-1</sup>, and 100 μm of spot size. Measurements were acquired as triplicates from different regions of the samples. Different pre-processing methods were evaluated to correct the slope and additive baseline variations in the raw spectra. The best performance was obtained using 2<sup>nd</sup> derivative with a Savitzky–Golay filter and a window size of the 15 points method. The SPXY method was used to separate the calibration (21 mixtures) and external validation

(9 mixtures) sets. Partial Least Squares Regression (PLS) models were developed and the regressions performances were evaluated using the Root Mean Square Error of Cross validation (RMSECV), of Prediction (RMSEP),  $R^2$  and Limit of Detection (LOD) values. The LOD values were calculated employing the MVC1 method, which is based on net analytical signal (NAS) [3].

Figure 1 shows the raw spectra of the mixtures acquired with the portable Raman spectrometer and the reference versus predicted plots for the calibration and external validation sets. Table 1 summarizes the parameters obtained for the PLS regression models. The results obtained, which are similar to those described in the literature [4], show a suitable performance for both instruments for the quantitative analysis of the MBZ polymorphs in the pharmaceutical raw materials. It is worth noting that the similar performance of the portable instrument to the benchtop, providing an easier and faster way for quality control of pharmaceutical materials.

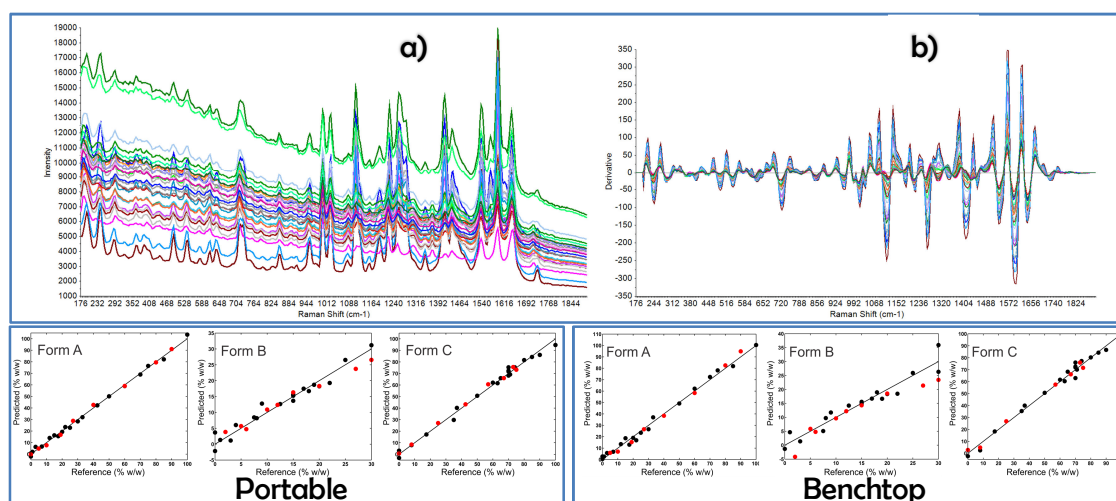


**Figure 1.** (a) Raw and (b) pre-processed spectrum for all mixtures acquired with portable Raman spectrometer. The reference versus predicted plots for the calibration (●) and external validation (●) sets for the three polymorphs of MBZ and for both spectrometers.

**Table 1.** General results for the PLS models for the polymorphs A, B and C of MBZ.

Instr.	Model	Form A			Form B			Form C		
		$R^2$	RMSE <sup>d</sup> (% w/w)	LOD <sup>e</sup> (% w/w)	$R^2$	RMSE <sup>d</sup> (% w/w)	LOD <sup>e</sup> (% w/w)	$R^2$	RMSE <sup>d</sup> (% w/w)	LOD <sup>e</sup> (% w/w)
Portable	Cross Val. <sup>a</sup>	0.99	1.76 (3) <sup>c</sup>	1.54-2.92	0.96	1.77 (5) <sup>c</sup>	1.28-2.05	0.99	2.80 (4) <sup>c</sup>	2.69-4.79
	Ext. Val. <sup>b</sup>	0.99	1.59		0.95	1.93		0.99	1.92	
Benchtop	Cross Val. <sup>a</sup>	0.99	2.72 (4) <sup>c</sup>	2.08-5.14	0.92	2.45 (3) <sup>c</sup>	2.63-4.30	0.98	3.57 (3) <sup>c</sup>	5.15-8.38
	Ext. Val. <sup>b</sup>	0.99	2.73		0.84	3.61		0.99	2.47	

a. Full Cross Validation; b. External Validation; c. Latent Variables; d. Root Mean Square Error; e. Limit of Detection

- [1] Ayala, A. P.; Siesler, H. W.; Cuffini, S.L. *J. Raman Spectrosc.* **2008**, *39*, 1150-1157.  
 [2] Silva, V. H.; Gonçalves, J. L.; Vasconcelos, F. V. C.; Pimentel, M. F.; Pereira, C. F. J. *Pharm. Biomed. Anal.* **2015**, *115*, 587–593.  
 [3] Olivieri, A. C.; Goicoechea, H. C.; Iñón, F. A. *Chemometrics and Intelligent laboratory Systems.* **2004**, *73*, 189–197.  
 [4] Silva, V. H.; Silva, J. J.; Pereira, C. F. *J. Pharm. Biomed. Anal.* **2017**, *134*, 287–294.

# Investigation for pH-induced Formation Mechanism of Alpha-Lactalbumin/Oleic Acid Complex by Using 2D Correlation Analysis

Yeonju Park<sup>1</sup>, Yujeong Park<sup>1</sup>, Hoeil Chung<sup>2</sup>, Young Mee Jung<sup>1,\*</sup>

<sup>1</sup>Department of Chemistry, Kangwon National University, Chuncheon 24341, Korea

<sup>2</sup>Department of Chemistry, Hanyang University, Seoul 04763, Korea

\*ymjung@kangwon.ac.kr

Human  $\alpha$ -lactalbumin made lethal to tumor cell (HAMLET) have cytotoxic activity with respect to tumor[1,2]. HAMLET consists of partially unfolded  $\alpha$ -lactalbumin (ALA) and oleic acid (OA). As ALA is partially unfolded by removing the calcium ion with acid and then OA is bound to the protein, HAMLET is formed. Molar ratio between ALA and OA is important to be formed stable HAMLET structure.

Changes of secondary and tertiary structures and amino acid residues of protein can be explored by using Raman spectroscopy, because their spectra are rich in signatures coming from side chain vibrations and from vibrations of the polypeptide backbone[3]. However the interpretation is not easy due to the Raman spectra of protein are very complicated. Two-dimensional (2D) correlation spectroscopy is a powerful method to solve this problem. 2D correlation spectroscopy provides the understanding the inter- or intra-molecular interactions, obtaining better resolved spectral information of highly overlapped bands and determining the sequential order of the events[4].

In this study, we investigated the formation mechanism of two ALA/OA complexes having different molar ratio with various pH by using Raman spectroscopy, principal component analysis (PCA), and 2D correlation spectroscopy. The results of Raman spectroscopy are shown in Figure 1. We observed changes of secondary structure and amino acid residues. From the Raman spectra, we caught that its variation has differences with ALA/OA complexes of different molar ratio. PCA and 2D correlation spectroscopy were applied to the pH-induced Raman spectra of ALA/OA complex to deeper understand the conformational changes and determine the formation mechanism of ALA/OA complex. The results of this study will be discussed in this presentation.

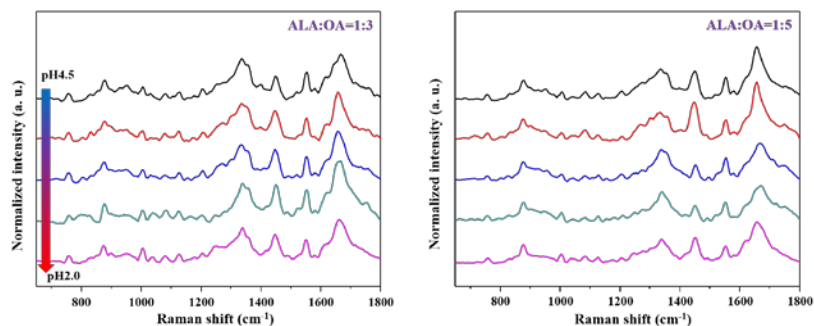


**Figure 1.** Raman spectra of ALA/OA complexes with pH variation.

- [1] Casbarra, A.; Birolo, L.; Infusini, G.; Dal Piaz, F.; Svensson, M.; Pucci, P.; Svanborg, C.; Marino, G. *Protein Science*, **2004**, *13*, 1322–1330.
- [2] Jøhnke, M.; Petersen, T. E. *The Alpha-Lactalbumin/Oleic Acid Complex and Its Cytotoxic Activity*; in Milk Protein, Hurley, W. L.(Ed), InTech, Croatia, 2012.
- [3] Tuma, R. *J. Raman Spectrosc.* **2005**, *36*, 307–319.
- [4] Czarnik-Matusiewicz, B.; Jung, Y.M. *Two-Dimensional Mid-Infrared Correlation Spectroscopy in Protein Research*, in Optical Spectroscopy and Computational Methods; in Biology and Medicine, Baranska, M. (Ed.), Springer, Berlin, 2014.

## Photodegradation of Benzidine-*p*-aminothiophenolate on TiO<sub>2</sub>: Correlation of Surface Enhanced Resonance Raman Spectroscopy and Photoreaction Kinetics

Christine Joy U. Querebillo<sup>1,2</sup>, Ibrahim Halil Öner<sup>3</sup>, Hoang Khoa Ly<sup>4</sup>, Robert Götz<sup>3</sup>,  
Ulrich Gernert<sup>5</sup>, Peter Hildebrandt<sup>1</sup>, Inez Weidinger<sup>3,\*</sup>

<sup>1</sup>*Institut für Chemie, PC 14, Technische Universität Berlin, Straße des 17. Juni 135, 10623 Berlin, Germany*

<sup>2</sup>*School of Analytical Sciences Adlershof, Humboldt-Universität zu Berlin, Unter den Linden 6, 10099, Berlin, Germany*

<sup>3</sup>*Technische Universität Dresden, Fachrichtung Chemie und Lebensmittelchemie, Elektrochemie, 01062 Dresden*

<sup>4</sup>*Department of Chemistry, University of Cambridge, Lensfield Road, CB2 1EW, Cambridge, United Kingdom*

<sup>5</sup>*Zentraleinrichtung Elektronenmikroskopie (ZELMI), Technische Universität Berlin, Straße des 17. Juni 135, 10623 Berlin, Germany*

\**inez.weidinger@tu-dresden.de*

Surface Enhanced Resonance Raman Spectroscopy (SERRS) was used to study the photodegradation of the dye pollutant Benzidine-*p*-aminothiophenolate (BD-PATP) on Titanium dioxide (TiO<sub>2</sub>) nanotubes. Unlike many degradation studies on TiO<sub>2</sub> which makes use of UV excitation, here, we used laser light at 413 nm to photodegrade BD-PATP on TiO<sub>2</sub> based on the photosensitized oxidation mechanism [1]. TiO<sub>2</sub> nanotubes were created via electrochemical anodization with subsequent heat-treatment at 300 or 475 °C. These two temperatures were chosen as the latter temperature was found to give significant higher electromagnetic field enhancement at the TiO<sub>2</sub> surface upon light illumination [2–3]. The aim of the present work is to study the effect of this surface enhancement on photocatalytic efficiency.

Performing diazonium reaction on PATP on TiO<sub>2</sub> with benzidine yields the diazo dye BD-PATP on TiO<sub>2</sub> as confirmed by SERRS (Fig. 1A, methods adapted from [4]). The photodegradation of the dye on TiO<sub>2</sub> (immersed in water which served as a heat sink) was then monitored by measuring its time-dependent SERRS spectral changes. A decrease in intensity of up to ~60 % of the initial intensity was observed for most of the prominent BD-PATP peaks (e. g. ~1450, ~1600 cm<sup>-1</sup>; peaks similar to values in [4]) after around 4 ms of (molecular) exposure to a (cw) laser source with a power of 1 mW (Fig. 1B). The peak at ~1084 cm<sup>-1</sup>, which was assigned to C-S stretch,  $\nu_{CS}$  [5–6], however, did not have a clear trend of decay over time or had slower decay rate compared to those of the other peaks. This indicates minimal desorption (or possible re-adsorption upon desorption) due to laser exposure because the PATP ring component remained close to the surface as seen in SERRS. Hence, we attribute the decrease in intensity of most BD-PATP peaks mainly to the dye photodegradation which decreased the amount of groups contributing to the respective normal modes observed in SERRS. By plotting the normalized intensities against the exposure time and fitting with an exponential decay model, we obtained a rate constant for the process (Fig. 2). Based on the peak at ~1600 cm<sup>-1</sup>, we found that the

photodegradation was faster by up to  $\sim 1.7\times$  for those on the  $475\text{ }^{\circ}\text{C}$  ( $k_{\text{AVE}} \sim 5\text{ s}^{-1}$ ) vs. on those at  $300\text{ }^{\circ}\text{C}$  ( $k_{\text{AVE}} \sim 3\text{ s}^{-1}$ ) annealed-TiO<sub>2</sub>. This observation supports our hypothesis that surface enhancement is correlated to the photoreaction kinetics of the system.

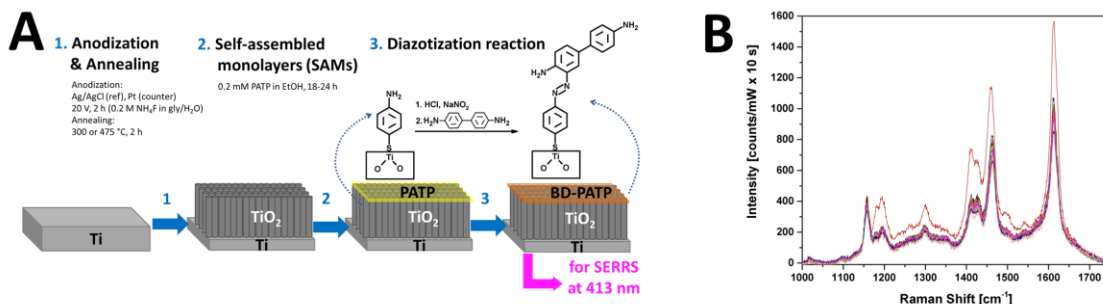


**Figure 1.** (A) Schematic diagram showing the formation of BD-PATP on TiO<sub>2</sub>. The general steps needed for this are: 1. Anodization and Annealing to form TiO<sub>2</sub> nanotubes from Ti, 2. Formation of PATP SAMs on TiO<sub>2</sub> nanotubes, and 3. Formation of BD-PATP on TiO<sub>2</sub> via a diazotization reaction of benzidine with PATP SAMs. (B) BD-PATP spectra showing decrease in peak intensities over time. This was taken for BD-PATP on TiO<sub>2</sub> annealed at  $475\text{ }^{\circ}\text{C}$  for up to 4 ms molecular exposure time.

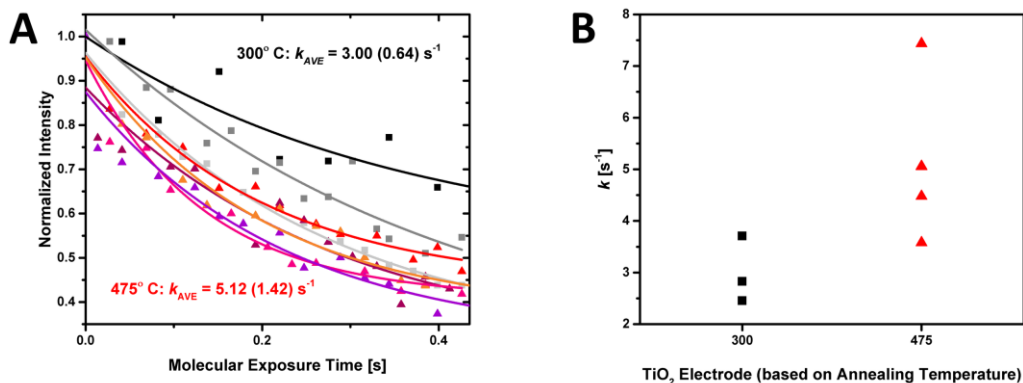


**Figure 2.** (A) Exponential decay of the photodegradation of BD-PATP on TiO<sub>2</sub> annealed at  $300\text{ }^{\circ}\text{C}$  (grayscale) and  $475\text{ }^{\circ}\text{C}$  (colored). The measured  $k$  values are more clearly shown in (B) which has some points being an overlap of two points with similar values.

[1] Konstantinou, I. K.; Albanis, T. A. *Applied Catalysis B: Environmental* **2004**, *49*, 1–14.

[2] Han, X. X.; Köhler, C.; Kozuch, J.; Kuhlmann, U.; Paasche, L.; Sivanesan, A.; Weidinger, I. M.; Hildebrandt, P. *Small* **2013**, *9*, 4175–4181.

[3] Öner, I. H.; Weidinger, I. M. *M.S. Thesis (Unpublished work)* **2016**.

[4] Han, X. X.; Chen, L.; Kuhlmann, U.; Schulz, C.; Weidinger, I. M.; Hildebrandt, P. *Angew. Chem. Int. Ed.* **2014**, *53*, 2481–2484.

[5] Kim, K.; Lee, H. S. *J. Phys. Chem. B.* **2005**, *109*, 18929–18934.

[6] Hu, X.; Wang, T.; Wang, L.; Dong, S. *J. Phys. Chem. C* **2007**, *111*, 6962–6969.

## Mild shearing deformation in graphite - reliability of the Raman graphite geothermometer

Martina Kirilova<sup>1</sup>, Virginia Toy<sup>1</sup>, Carolina Giorgetti<sup>3</sup>, Keith C. Gordon<sup>2</sup>, Jeremy S. Rooney<sup>2\*</sup>

<sup>1</sup> *Department of Geology, University of Otago, PO Box 56, Dunedin 9056, New Zealand*

<sup>2</sup> *Department of Chemistry, University of Otago, PO Box 56, Dunedin 9056, New Zealand*

<sup>3</sup> *Dipartimento di Scienze della Terra, Università degli Studi La Sapienza, Rome, Italy*

\**rooje841@student.otago.ac.nz*

The transformation of carbonaceous material into graphite occurs during diagenesis and metamorphism. This complete transformation is irreversible and is characterised by numerous physical and chemical changes such as a decrease in the interplanar distance, a shrinking H/C ratio, an increase in crystallite size and a large increase in reflectivity [1]. In the geological discipline, determination of the peak temperature at which this metamorphism occurs and its extension to neighboring rocks is highly valued. It is widely accepted that graphite's crystallinity, as measured by Raman spectroscopy or X-ray diffraction, is a reliable measure for determining the peak temperature during metamorphism [2-3]. One of the assumptions of the graphite geothermometer is that temperature is the sole factor contributing to graphite's crystallinity as shown by the relative area of the G-band [2]. Several researchers have noted discrepancies in the graphite geothermometer and it has led to attempts to standardise the peak fitting protocol [4-5]. Nonetheless inconsistencies remain and it has been suggested that shear strain should be taken into account especially due to graphite's lubricant nature (coefficient of friction  $\sim 0.1$ ) and its presence in fault zones [2, 6-7].

Consequently, we performed a series of deformation experiments whereby we gently sheared highly crystalline graphite powder (160  $\mu\text{m}$ ) at room temperature with normal stresses of 5 MPa and 25 MPa. The sliding velocities were 1, 10 and 100  $\mu\text{m s}^{-1}$  while the total displacement was 5, 10 and 20 mm. These gentle shearing parameters completely removed temperature as a factor in our results. We observed a consistent layer of deformed graphite over crystalline graphite. The resulting Raman microscopic measurements (Witec microscope, 532 nm at 2 mW with a 50 $\times$  objective) showed that the sheared graphite was significantly less crystalline than the unsheared starting material. We found systematic decreases in graphite crystallinity with increased displacement, increased pressure and increased velocities. We conclude: graphite thermometers are unreliable in brittlely deformed rocks (i.e. cataclasites) and adequate shear strain calibration of the graphite geothermometer is needed.

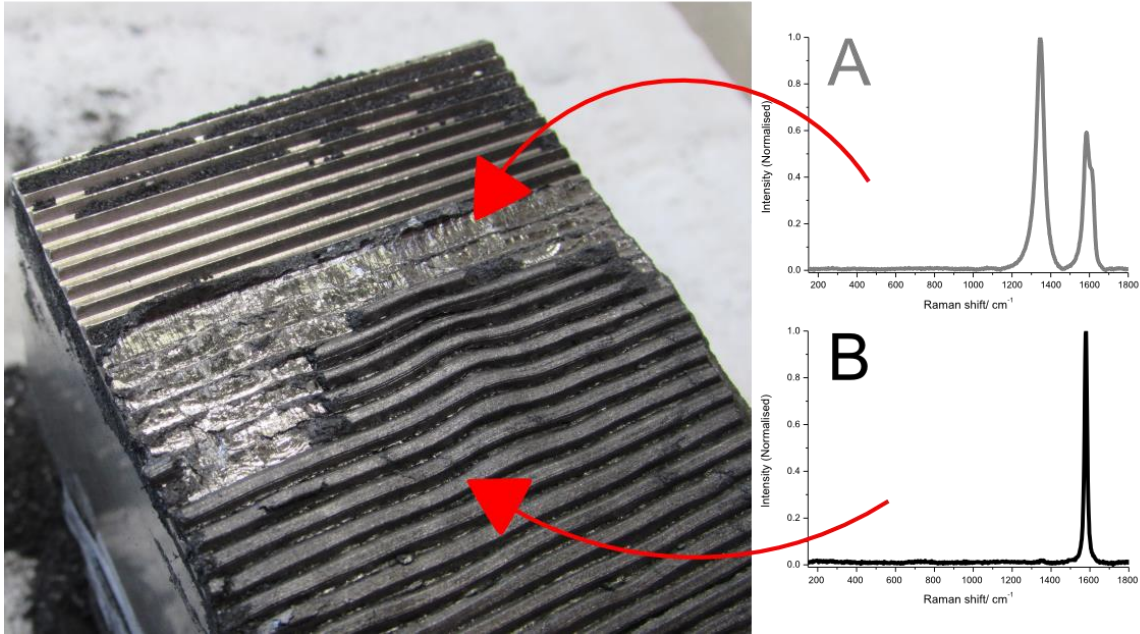


**Figure 1.** An image of the sheared graphite, a spectrum of the deformed graphite on the surface (A) and a spectrum of the highly crystalline graphite that was underneath (B).

- [1] Luque, F. J.; Barrenechea, J. F.; Rodas, M. *Geol. Mag.* **1993**, *130*, 501-511.
- [2] Barzoi, S. C. *Int. J. Coal. Geol.* **2015**, *146*, 179-187.
- [3] Beyssac, O.; Goffe, B.; Chopin, C.; Rouzaud, J. N. *J. Metamorph. Geol.* **2002**, *20*, 859-871.
- [4] Crespo, E.; Luque, J. F.; Barrenechea, J. F.; Rodas, M. *Mineral. Mag.* **2006**, *70*, 697-707.
- [5] Luensdorf, N. K.; Dunkl, I.; Schmidt, B. C.; Rantitsch, G.; Eynatten, H. *Geostand. Geoanal. Res.*, **2014**, *38*, 73-94.
- [6] Nakamura, Y.; Oohashi, K.; Toyoshima, T.; Satish-Kumar, M.; Akai, J. *J. Struct. Geol.*, **2015**, *72*, 142-161.
- [7] Kouketsu, Y.; Shimizu, I.; Wang, Y.; Yao, L.; Ma, S.; Shimamoto, T. *Tectonophysics* **2017**, *699*, 129-145.
- [8] Kiriloval, M.; Rooney, J. S.; *et al.* (submitted)

## Potential SINS at the Canadian Light Source

Scott M. Rosendahl<sup>1,\*</sup>

<sup>1</sup>*Canadian Light Source Inc., 44 Innovation Boulevard, Saskatoon, SK, Canada, S7N 2V3*

<sup>\*</sup>*scott.rosendahl@lightsource.ca*

Synchrotron Infrared Nano-Spectroscopy (SINS) enables the investigation of variety of nanoscale, mesoscale, and surface phenomena that were previously difficult to study due to the natural diffraction limit of infrared light. By combining atomic force microscopy (AFM), Fourier Transform Infrared (FTIR) and infrared synchrotron light, researchers are gaining the ability to investigate materials spatially and spectroscopically to the tens of nanometers in the mid-infrared (500-5000 cm<sup>-1</sup>).

SINS is one of the faster growing areas of research in the synchrotron infrared community worldwide with researchers at several synchrotron facilities, utilizing the broadband and brightness properties of the source, successfully demonstrating this technique in a variety of scientific fields with new applications constantly emerging. Extending these capabilities to the Canadian Light Source (CLS) is technically challenging but will offer Canadian researchers more access to this exciting area of sub-diffraction limited microscopy in the infrared.

The aim of this talk will be to provide an overview of the live demonstration of a NeaSpec neaSNOM system and the future direction of SINS at the CLS. This demonstration proved to be straightforward to setup and allowed for the first mid-infrared synchrotron near-field spectroscopic measurements to be made. A discussion on how to improve the optics of the beamline (improved brightness, collimation, etc...) will be presented leading into a discussion on continuing the efforts to move this technology to the CLS. In addition, a brief example of how nano-infrared spectromicroscopy is helping advance the Plant Imaging Program at the CLS by looking at the plant cell walls of important Canadian prairie crops in new light.

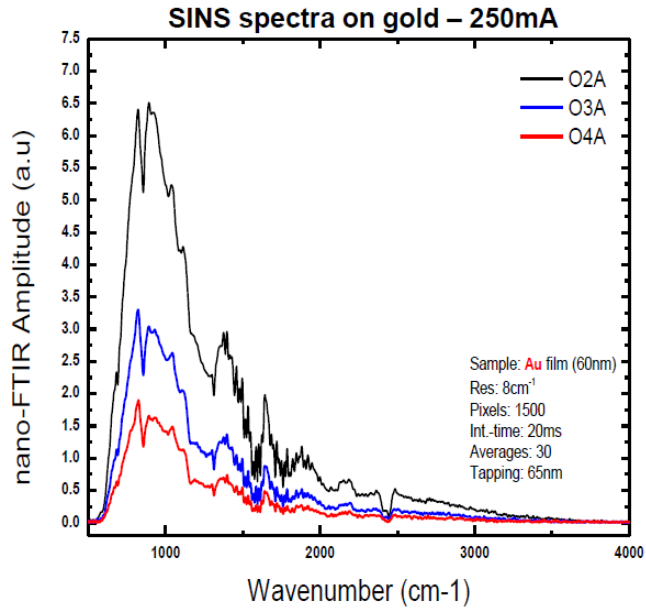


**Figure 1.** First Synchrotron Broadband Infrared Nano Spectra recorded at the Mid-Infrared Spectromicroscopy Beamline at the Canadian Light Source. Measurements were possible with the generous support of NeaSpec GmbH, utilizing a neaSNOM Nano-FTIR microscope.

# Simultaneous ATR-FTIR based determination of malaria parasitemia, glucose and urea in spiked whole blood dried onto a glass slide

Supti Roy<sup>1</sup>, David Perez-Guaita<sup>1</sup>, Dean W. Andrew<sup>1</sup>, Jack S. Richards<sup>2,3,4</sup>, Don McNaughton, Philip Heraud<sup>1</sup> and Bayden R. Wood<sup>1</sup>

<sup>1</sup> Centre for Biospectroscopy, Monash University, Clayton, 3800, Victoria, Australia

<sup>2</sup> Centre for Biomedical Research, Burnet Institute, Melbourne, Victoria, Australia

<sup>3</sup> Department of Medicine, University of Melbourne, Parkville, 3052, Victoria, Australia

<sup>4</sup> Infectious Disease Department, Monash University, Melbourne, 3004, Victoria, Australia

Literature evidences that ATR-FTIR spectroscopy of blood has demonstrated great potential in the diagnosis of several diseases<sup>1</sup> and the prediction of clinical parameters<sup>2</sup> which asses the metabolic state of the patient. From a theoretical point of view, the information contained in the IR spectra is not unlimited, and therefore metabolic changes produced by the illnesses could

interfere in the prediction of clinical compounds and vice versa. Our aim was to investigate the potential of this technique for diagnose different illnesses and conditions from a single spectrum of a drop of blood dried onto a glass microscope slide. It is a simple point of care test study but may be able to assist in the clinical management of malaria patient.

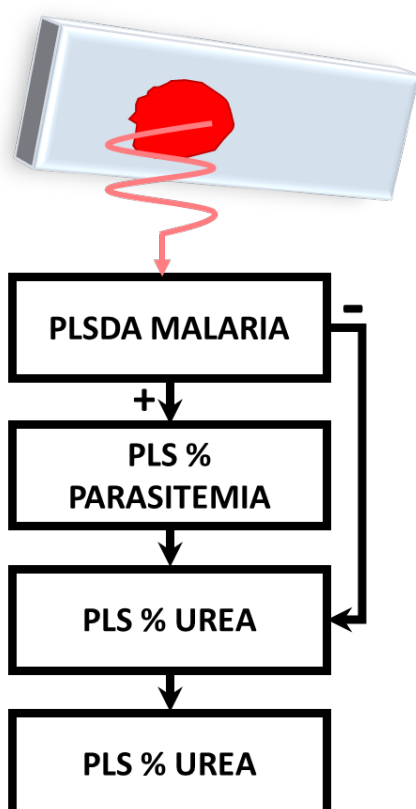


**Figure 1.** Graphic summary of the algorithm created for the investigation of the different conditions.

3 microliters of blood obtained from different patients (N=6) were spiked with different amounts *Plasmodium falciparum* (0-5%), glucose (0-400 mg/dL) and urea (0-300 mg/dl) and 132 samples were obtained. The database constructed from these spectra was used for constructing an algorithm which sequentially tested the spectrum (See Figure1) for: a) the presence of the malaria parasite; b) the amount of the parasite in the sample (if applicable); c) the glucose concentration; and d) the urea concentration. Partial Least Squares-Discriminant Analysis (PLS-DA) was used for the malaria diagnosis and PLS regression (PLSR) was used for the quantification of parasite percentage in the sample as well as glucose and urea concentrations.

According to cross validation, PLSDA was able to predict correctly more than the 90 % of the samples with parasitemia higher than 0.5%. The three models of PLSR (see Figure 2) showed the ability to predict the analytes under investigation.

The Root Mean Square Error of Cross Validation (RMSECV) are 0.58% for parasitemia, 22.73 mg/dL for glucose and 30.48 mg/dL for urea. The relative RMSECV for glucose is 16% and for urea is 15%. The RPD values for the predictions of parasitemia, glucose and Urea was 2.77, 4.07 and 4.51 respectively, showing very good modelling of all parameters. A deep investigation on the spectral interferences between each condition was also performed.

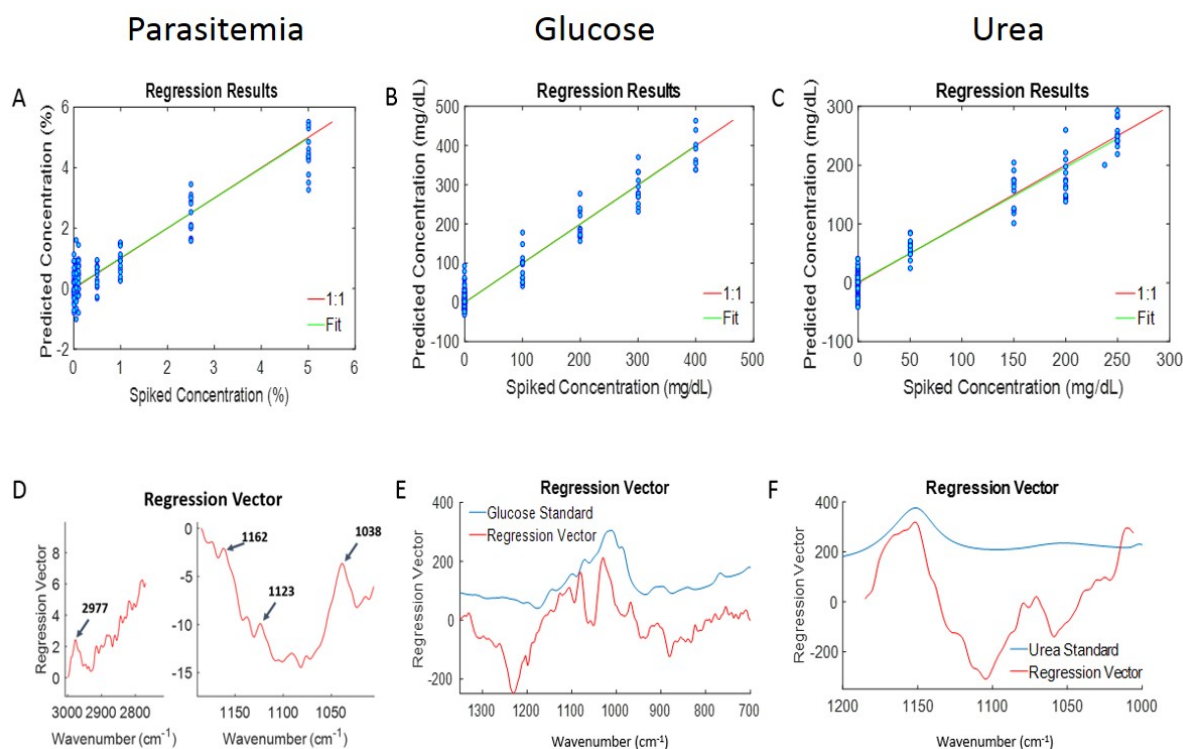


**Figure 2:** PLS-R results for modelling the spiked concentration of: (A) parasitemia (0-5%); (B) glucose (0-400 mg/dL); (C) urea (0-250 mg/dL). The upper panel indicates the spiked vs predicted concentration for each sample and the lower panels show the corresponding regression vectors. In the case of glucose and urea, the regression vectors are compared with spectra of glucose and urea standards acquired under the same conditions. The regression vectors have been integrated using the *cumsum* (cumulative summation) function in MATLAB.

## References

- <sup>1</sup> Baker MJ et al. *Nature*, 2014, **9**, 1771–1791.
- <sup>2</sup> Perez-Guaita D et al. *TrAC*, 2014, **62**, 93-105.
- 3 Roy S et al, Submitted to *Anal. Chem*, (in review; Minor Revision)

## Structural Changes on Russellite with Intercalation: IR Spectroscopic Studies

Y. Sakai<sup>1,\*</sup>, H. Okudera<sup>1</sup>, A. Arasuna<sup>1</sup>, H. Takeda<sup>2</sup>

<sup>1</sup>*Graduate School of Natural Science and Technology, Kanazawa University,  
Kakuma-machi, Kanazawa 920-1192, Japan.*

<sup>2</sup>*School of Materials and Chemical Technology, Tokyo Institute of Technology,  
2-12-1 Ookayama, Meguro, Tokyo 152-8552, Japan.*

\*sakaiyuka@stu.kanazawa-u.ac.jp

Russellite ( $\text{Bi}_2\text{WO}_6$ ) is one of Aurivillius phases in which perovskite-like  $\text{WO}_6$  layers were sandwiched by double  $\text{Bi}_2\text{O}_2$  layers and crystallizes in orthorhombic,  $Pca2_1$  [1] with  $a = 5.434(2)$  Å,  $b = 16.432(2)$  Å,  $c = 5.455(2)$  Å. Recently we found that the flux-grown russellite specimen changed its color in diluted hydrochloric acid from pale yellow to dark blue by pinching with tweezers. This change in color and shrinkage of the **b**-axis length (unpublished data) indicated intercalation of  $\text{H}^+$  and, possibly, even  $\text{Cl}^-$  and  $\text{H}_2\text{O}$  molecule in its structural framework and associated change in its stereochemistry. Because these changes occurred quite easily and quickly with faint structural changes, this compound can be a good example on exploration of binding state of intercalant in a host structure.

Here the authors present results of FT-IR spectroscopic measurements with KBr micro-pellet transmission and reflective micro-IR methods on flux-grown russellite specimen in powdery form before and after immersion in diluted hydrochloric acid. This study will give us potential insight on understanding interactions between minerals and water, such as sorption of water on rock-forming minerals at subduction zone and transport of water into the deep Earth.

### Micro-IR measurements

Gently ground, flux-grown russellite [2] was immersed in 1N HCl and extra solution was soaked up with a piece of paper, then dried on Au-plated mirror. Measurement was started just before and after the treatment and repeated at every 24 hours for nine days. Another powdery specimen, which was treated with 2N HCl and kept for 1 year with desiccant was also examined for comparison.

IR absorption spectra were compared with each other in detail over the range of  $\nu = 600 \sim 900 \text{ cm}^{-1}$  where five absorption bands assignable to bending and stretching modes of  $\text{WO}_6$  octahedra will be visible [3]. Two bands at  $\nu = 632$  and  $687 \text{ cm}^{-1}$  attributable to bending mode were shifted toward lower wavenumbers after HCl treatment. Three bands at  $\nu = 778$ ,  $819$  and  $840 \text{ cm}^{-1}$  were attributable to stretching modes, and one of those (at  $\nu = 840 \text{ cm}^{-1}$ ) became prominent after HCl treatment. No change occurred on absorption at  $\nu = 778 \text{ cm}^{-1}$  just after the treatment, while the absorption got weaker with time. This weakening was confirmed also on the 1 year-passed specimen. Water-related bands (mainly  $\text{H}_2\text{O}$ ) observed at high wavenumbers at  $\nu = 1632$ ,  $3255$ ,  $3430$  and  $3547 \text{ cm}^{-1}$  [4] were prominent over nine days and even after 1 year from the treatment.

### KBr micro-pellet measurements

Non-treated and 1 year-passed specimens were examined with KBr micro-pellet technique. Observed shifts and changes in absorbance of four absorption bands in the range of  $\nu = 600 \sim 900 \text{ cm}^{-1}$  are concordant with the results of micro-IR measurements. The band at  $\nu = 703 \text{ cm}^{-1}$  ( $\nu = 778 \text{ cm}^{-1}$  on micro-IR) was shifted toward lower wavenumber after treatment with broadening.

## Discussions

Shift of absorption bands assigned to  $\text{WO}_6$  bending mode suggests reduction in bend of O-W-O diagonal bond angles. In addition, change in relationship among absorbance due to  $\text{WO}_6$  stretching modes suggest not only shrinkage of the W-O bond distances but also reduction in variation among them. Therefore, these results indicate reduction in shift of W from the center of  $\text{WO}_6$  octahedron after the treatment and then relaxation of the structure from distorted orthorhombic one to tetragonal aristotype with presence of intercalant. Water-related bands (at  $\nu = 3255$  and  $3430 \text{ cm}^{-1}$ ) indicate physisorption of  $\text{H}_2\text{O}$  molecules at the surface. Since these bands were prominent even on 1 year-passed specimen, we can conclude that russellite can hold plenty water even under dry condition.

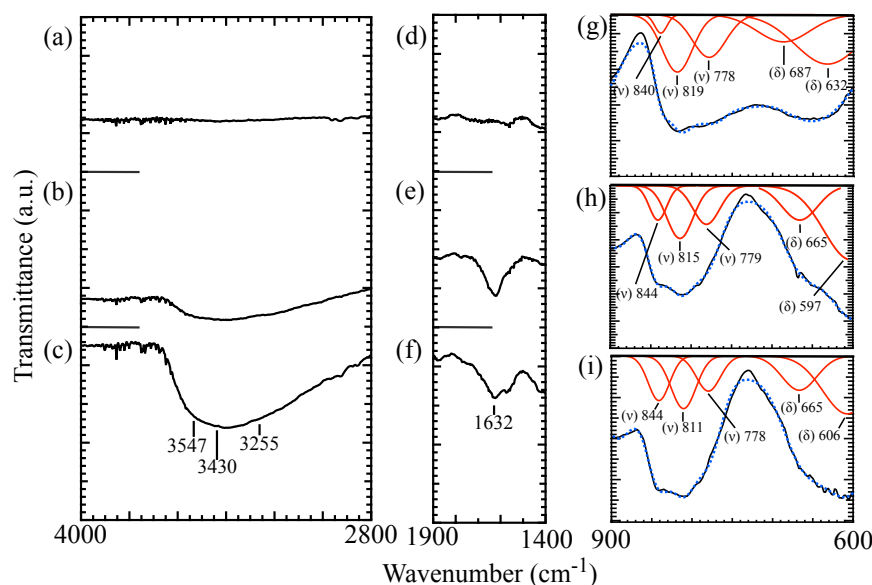


**Figure 1.** Micro-IR spectra collected before treatment (a, d, g), immediately after treatment (b, e, h), and 9 days after treatment (c, f, i). Black, blue, and red lines represent observations, fitting results, and split peaks, respectively. Different baselines for observations with fitting results and split peaks were employed for clarity.  $\delta$ : bending mode,  $\nu$ : stretching mode.

## References

- [1] Knight, K. S. *Min. Mag.* **1992**, *56*, 399-409.
- [2] Takeda, H.; Nishida, T.; Okumura, S.; Shiosaki, T. *J. Eur. Ceram. Soc.* **2005**, *25*, 2731-2734.
- [3] Maczka, M.; Macalik, L.; Hermanowicz, K.; Kepinski, L.; Tomaszewski, P. *J. Raman Spectrosc.* **2010**, *41*, 1059-1066.
- [4] Garcia-Baonza, V.; Rull, F.; Dubessy, J. *EMU Note in min.* **2012**, *12*, in Raman Spectroscopy applied to Earth Sciences and Cultural Heritage, chapter8, pp. 279-320.

## Paint Identification Using FT Spectroscopy from MIR to THz Spectral Range

Sergey Shilov

*Bruker Optics, 19 Fortune Dr., Billerica, MA 01821*

*Sergey.Shilov@bruker.com*

Identification of different paints is in high demand in the art conservation and forensic communities. In general paint is composed of several chemical compounds: inorganic pigments, polymer binder, and additives. A commonly used technique for paint identification involves the comparison of infrared spectra of an unknown paint against a spectral library. Inorganic pigments have characteristic bands in the Far IR (FIR) range below  $400\text{ cm}^{-1}$  ( $\sim 12\text{ THz}$ ) while polymer binders have distinctive spectral features in the Mid-IR spectral range ( $4000\text{--}400\text{ cm}^{-1}$ ). Measuring both ranges will allow accurate paint identification.

Since atmospheric water vapor contributes to the spectra in the FIR range, FIR spectroscopy requires a careful purge of the spectrometer with a moisture free gas. Switching of optical components is undesirable, because it could break the purge.

Library of different paint samples were acquired using Bruker Vertex FM spectrometer. This spectrometer uses a broadband beamsplitter and a room temperature broadband detector. In combination with a globar source, it allows measurements from  $6000\text{ to }50\text{ cm}^{-1}$  ( $1.5\text{ THz}$ ) in one step without exchanging optical components. Single bounce diamond ATR or  $30^\circ$  specular reflectance accessory was used in the sample compartment of the Vertex FM. Spectral resolution was set to  $4\text{ cm}^{-1}$ , sample acquisition time was 1 min per spectrum.

Example of reflectance and ATR spectrum of paint is shown in Fig. 1. A distinctive feature of reflectance spectra is its derivative shape below  $1900\text{ cm}^{-1}$ . Specular reflectance depends on the refractive index of the reflecting media. The refractive index within the absorption band increases initially before it decreases. Such rapid changes in the refractive index lead to a derivative shape of bands in the specular reflectance spectrum. Commercial spectral libraries consist of spectra collected by ATR or transmittance. For this reason reflectance spectra cannot be directly used for searching within such libraries. Specular reflectance spectra can be converted to absorbance units by performing a Kramers-Kronig Transform (KKT). This function is a part of the standard OPUS package. An example of applying the KKT to MIR-FIR spectrum is shown in Fig. 1. As can be seen from this figure, reflectance data after KKT is very similar to ATR data.

Reflectivity of a sample depends on its surface roughness and the wavelength of light. Specular reflectance will be observed if the sample roughness is small compared to the wavelength of incident light. Reflection will be diffused if the sample roughness is bigger than the light wavelength. Reflection from the same sample can be specular or diffused depending on its spectral range. For example (Fig. 2), reflectance from Prussian blue/lead white is specular in the  $2000\text{--}50\text{ cm}^{-1}$  ( $5\text{--}10\text{ microns}$ ) range and diffused above  $2500\text{ cm}^{-1}$  ( $4\text{ microns}$ ). In this case, a KKT needs to be performed in the  $2000\text{--}50\text{ cm}^{-1}$

range only. A spectrum of this sample above  $2500\text{ cm}^{-1}$  can be used for the library search without KKT.

Simultaneous identification of paint binder and pigment is possible using multicomponent spectra search with Bruker's OPUS software.

**Conclusion:** FTIR spectrometer which is capable to measure Mid to Fir IR spectral ranges without optical component exchange significantly improves the ability to analyze painted samples and objects of interest.

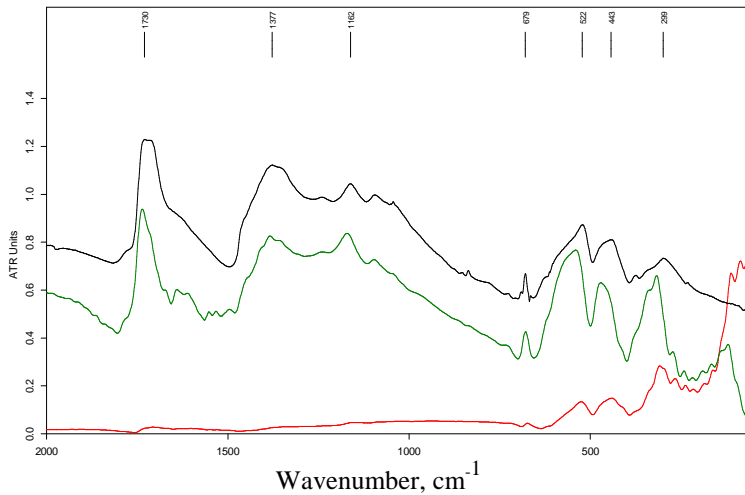


**Figure 1.** MIR-FIR spectrum of paint with venetian red/ white lead pigments: reflectance spectrum (bottom), resultant absorbance spectrum after KKT (middle), ATR after ATR correction (top). KKT corrected reflectance spectrum is very similar to the ATR spectrum.

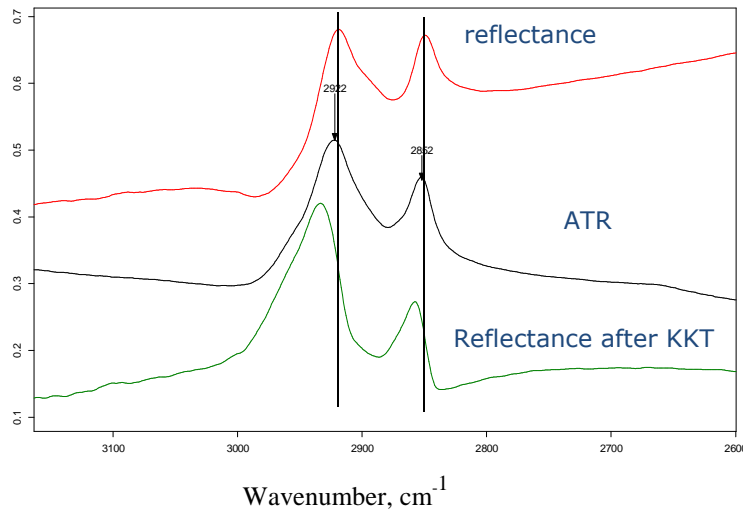


**Figure. 2** Spectrum of paint with prussian blue/lead white pigments in the  $2600\text{-}3200\text{ cm}^{-1}$  spectral range. Band position in reflectance spectrum is close to that found in the ATR spectrum. Because diffuse reflectance component prevails in this range, KKT of reflectance spectrum in this spectral region will lead to incorrect band positions

# Protein hydrations in living cell probed by Fourier transform infrared (FT-IR) spectroscopic imaging

Hideyuki Shinzawa<sup>1,2\*</sup>, Benjamin Turner<sup>1</sup>, Junji Mizukado<sup>2</sup>, Sergei G. Kazarian<sup>1</sup>

<sup>1</sup>*Department of Chemical Engineering, Imperial College London, United Kingdom, London SW7 2AZ*

<sup>2</sup>*National Institute of Advanced Industrial Science and Technology (AIST), Japan, Central 5-2, 1-1-1, Higashi, Tsukuba*

\**h-shinzawa@aist.go.jp*

The analysis of spectroscopic imaging datasets by disrelation mapping [1,2] is extended to the application of living cells for probing protein hydration. Disrelation mapping was developed recently to allow the use of 2D correlation analysis to identify subtle but pertinent spectral variations within spectroscopic images. A schematic illustration to demonstrate the basic concept of disrelation mapping is shown in Fig. 1.

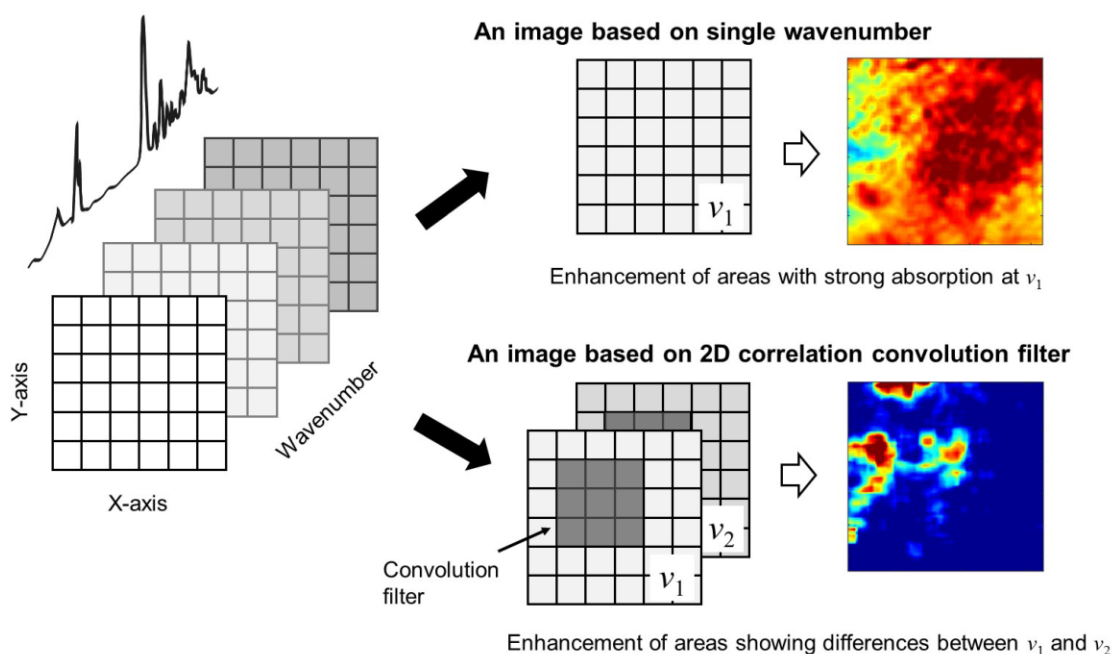


**Figure 1.** A schematic illustration of disrelation mapping based on 2D correlation convolution filter.

Fourier transform infrared (FT-IR) spectroscopic imaging using a focal plane array detector allows for the simultaneous acquisition of spatially resolved spectra, as each pixel provides an individual FT-IR spectrum. The data obtained is has a hypercube structure, consisting of two spatial and one spectral variable. Analysis of the spectroscopic imaging data can generally be achieved by univariate analysis such as band integration or multivariate methods like principle component analysis. Disrelation maps are generated using a convolution filter based on 2D correlation analysis of FT-IR images

measured at two different wavenumbers. For each pixel and its neighbours, as defined by the convolution window, 2D correlation analysis is carried out to derive the disrelation intensity. Disrelation intensity appears on the disrelation map only if spectral absorbance measured at the two different wavenumbers varies out of phase with each other. Thus, one can expect to see the development of a substantial level of disrelation intensity only in region where chemically or physically meaningful variations occur. This means disrelation maps can be utilized to identify the regions where specific interactions between components occur.

The application of disrelation mapping to FT-IR spectroscopic imaging data is present in this study where obtained FT-IR imaging data of a living cell were subjected to disrelation analysis. The 2D correlation analysis of HEK cell revealed the disrelation peaks at  $(3420\text{ cm}^{-1}, 3220\text{ cm}^{-1})$ , showing the existence of a particular water band around at  $3220\text{ cm}^{-1}$  whose variation of absorbance did not follow the trend of the coordinated bulk water molecules. Disrelation map constructed with the correlation intensities at  $(3420\text{ cm}^{-1}, 3220\text{ cm}^{-1})$  reveals that the disorder of the water network occurs especially around at the boundary between the cell and media, indicating that the water molecules in intracellular fluid are interacting with intracellular protein (Figure 2). This result is consistent with the view that the intracellular fluid and media have different compositions, generating different molecular environment of water. Interestingly, the development of the hydration also becomes obvious around the nucleus or its neighbouring structure, probably reflecting the fact that the synthesis of the protein mainly occurs in these regions.

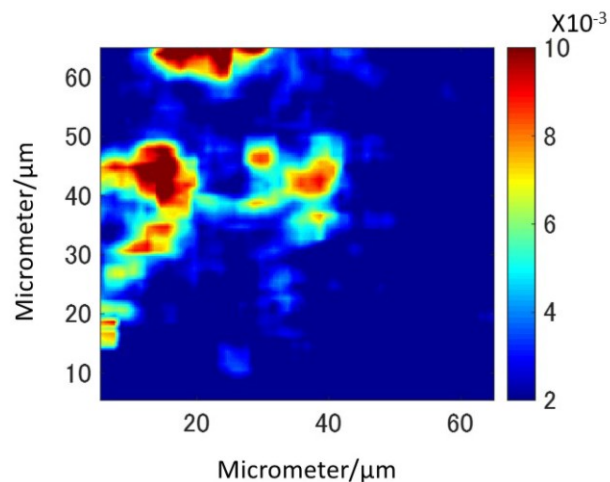


**Figure 2.** Disrelation map constructed with the IR bands at  $3420\text{ cm}^{-1}$ ,  $3220\text{ cm}^{-1}$ , each representing different water species.

[1] Shinzawa, H.; Mizukado, J.; Kazarian, S. G. Applied Spectroscopy **in press**.

[2] Shinzawa, H.; Mizukado, J. Spectrochimica Acta Part A **in press**.

## Infrared studies of antibiotic peptides in the bio-mimetic membranes supported at a gold electrode surface

Zhangfei Su, Muzaffar Shodiev, Adrian L. Schwan, and Jacek Lipkowski\*

*Department of Chemistry, University of Guelph, Guelph, Ontario N1G 2W1, Canada*

E-mail: [zhangfei@uoguelph.ca](mailto:zhangfei@uoguelph.ca)

Polarization modulation infrared reflection absorption spectroscopy (PM-IRRAS) is a powerful technique to study antibiotic peptides in the bio-mimetic membranes supported at a gold electrode surface. The amide I band (1600 ~ 1700 cm<sup>-1</sup>) of peptides does not overlap with the absorption bands of lipids and hence it provides molecular level information about the conformation and the orientation of peptides.

We will describe application of PM-IRRAS to study the conformation and orientation of two peptides, valinomycin and gramicidin, in a tethered lipid bilayer.<sup>1-3</sup> Valinomycin is a cyclic peptide, which can selectively transport potassium ions through both biological and synthetic membranes. The ability of valinomycin to carry ions across a membrane is primarily due to formation of a bracelet shaped molecular complex. The IR spectra can be used to confirm formation of the complex. The frequency of the carbonyl stretch of the complex is strongly dependent on the polarity of its environment. We used this property to demonstrate that the complex is inserted predominantly in the nonpolar fragment of the membrane. The amide band intensity provides information about the orientation of the complex. Our results indicate that the complex is inserted into the membrane with the bracelet being almost parallel to the membrane surface.

Gramicidin is a hydrophobic peptide forming  $\beta$ -helix which acts as a channel conducting monovalent cations across the biological membranes. PM-IRRAS technique was employed to study the conformation and orientation of gramicidin in tethered lipid bilayer. The IR results revealed that  $\beta$ -helix conformation is prevalent in the model membrane. In the open channel state, the helices assume an orientation of 29° tilt angle between the helix axis and the surface normal. In the channel closed state, the gramicidin molecules are oriented randomly in the model membrane.

[1]Leitch, J.; Kunze, J.; Goddard, J.D.; Schwan, A.L.; Faragher, R.J.; Naumann, R.; Knoll, W.; Dutcher, J.R.; Lipkowski, J. *Langmuir* **2009**, 25, 10354-10363.

[2]Laredo, T.; Dutcher, J.R.; Lipkowski J. *Langmuir* **2011**,27, 10072-10087.

[3]Fiche, J.B.; Laredo, T.; Tanchak, O.; Lipkowski, J.; Dutcher J.R.; Yada, R.Y. *Langmuir*, **2010**, 26, 1057-1066.

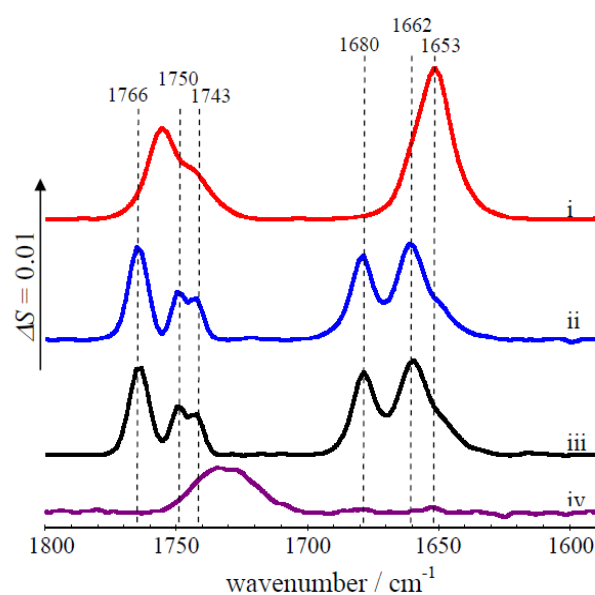


Figure 1 PM-IRRAS spectra of valinomycin-DPhPC(20:80)/DPTL tBLM in 0.1 M  $\text{KClO}_4/\text{D}_2\text{O}$  (i, red), 0.1 M  $\text{NaClO}_4/\text{D}_2\text{O}$  (ii, blue) and pure  $\text{D}_2\text{O}$  (iii, black); and DPhPC/DPTL tBLM in 0.1 M  $\text{KClO}_4/\text{D}_2\text{O}$  (iv, purple).

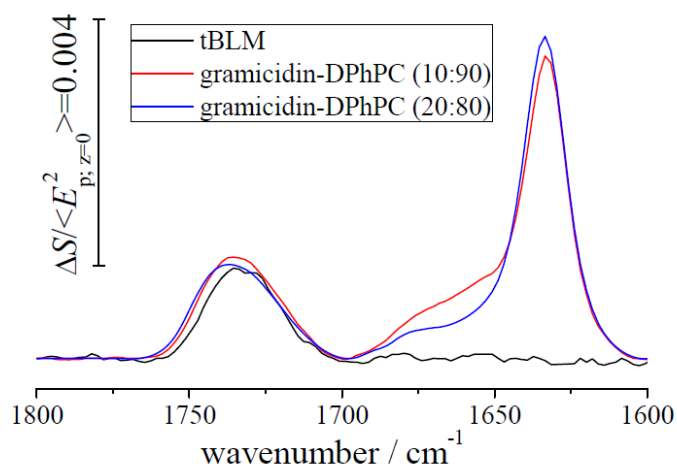


Figure 2 PM-IRRAS spectra of the DPhPC/DPTL tBLM (black), gramicidin-DPhPC(10:90)/DPTL tBLM (red) and gramicidin-DPhPC(20:80)/DPTL tBLM (blue) in the C=O stretching region in 0.1 M  $\text{KClO}_4/\text{D}_2\text{O}$ .

# Temperature dependence of *LOPC* mode on 4H-SiC by micro-Raman imaging in high temperature region

Jun Suda\*, Yuya Mastuo, Satoshi Suwa, Shugo Mizuno, Kouki Togo

101-2 Yagoto Honmachi, Showa-ku, Nagoya-shi, 466-8666, Japan  
Department of Electrical and Electronic Engineering, School of Engineering, Chukyo University

\*suda@sist.chukyo-u.ac.jp

Abstract Raman images ( $40\mu\text{m}\times 40\mu\text{m}$ ) of a bulk 4H-SiC wafers have been measured in Micro-Raman Spectroscopy at temperature from room temperature to 673K. As temperature increases, Raman linewidth of a *LOPC* (LO-phonon-plasmon-coupled) mode ( $970\text{cm}^{-1}$ ) show increasing both monotonously and slightly. We have obtained linewidth of *LOPC* mode using experimental Raman imaging at this temperature range. We have evaluated temperature dependence of the line broadening and the center frequency of *LOPC* mode in 4H-SiC in high temperature region.

4H-SiC, as one of the most promising wide band gap semiconductors, is a kind of ideal material for high voltage and high temperature applications. Seminal work of Raman scattering of SiC polytypes was reported by Nakashima and Harima [1]. They can obtain the electro density and electro mobility by fitting calculation to spectra of *LOPC* mode [1]. However, a few investigations with respect to temperature dependence of Raman shift in 4H-SiC by the only point Raman analysis have been reported up to now [2]. As an ideal material for high power and high temperature devices, properties of SiC at different temperatures, especially at high temperatures up to 573K [3], are significant to its practical application. Therefore, the variation of *LOPC* mode by Raman imaging in high temperatures would be important for these application. In this study, we perform Raman imaging measurements for *LOPC* mode over a series of temperature at 290-573 K on 4H-SiC bulk wafers.

A confocal micro-Raman spectroscopy system, NRS-4100 with a 2400 l/mm grating, was employed to study Raman mode shift of 4H-SiC samples with temperature varying from room temperature to 573 K (Fig.1(A)). Spectral resolution of the system is up to  $0.4\text{ cm}^{-1}$  and the accuracy of wavenumber is within  $\pm 0.1\text{cm}^{-1}$ . The 4H-SiC sample ( $5\text{mm}\times 5\text{mm}\times 0.33\text{mm}$  (c axis) ) with carrier concentration of  $2.3\times 10^{18}\text{cm}^{-3}$  and electric mobility  $115\text{cm}^2/\text{Vs}$  in Hall measurement was prepared by MOCVD method [4]. As temperature increases, Raman peaks of  $E_2(\text{TO})$  mode ( $778\text{cm}^{-1}$ ) show monotonously down (Fig. 1(B))and linewidth is broadened monotonously with increasing temperature (Fig.1(C)) [4]. We have obtained average values of linewidth and center frequency by Raman imaging of linewidth and center frequency for *LOPC* mode ( $970\text{cm}^{-1}$ ) over the imaging area of  $40\mu\text{m}\times 40\mu\text{m}$  on surface of 4H-SiC. *LOPC* mode in doped 4H-SiC shows asymmetric broadening as one mode [2]. As shown in Fig. 2(C), the average values of Raman linewidth of *LOPC* mode show interesting property *i. e.*, the large line broadenings with temperature. The average values of center frequency of *LOPC* mode

show a little change with increasing temperature. In impurities doping of this study, this ionization processes are sensitive to temperature. Free carrier concentration increases when temperature goes up to higher temperatures and remains almost constant in center frequency after impurities are totally ionized. The monotonous variation of linewidth with temperature for *LOPC* mode from doped 4H-SiC could be explained by effect due to ionization process of impurities on the process of Raman scattering.

The author is grateful to the Chukyo University Research Found (2016) for financial assistance with this research.

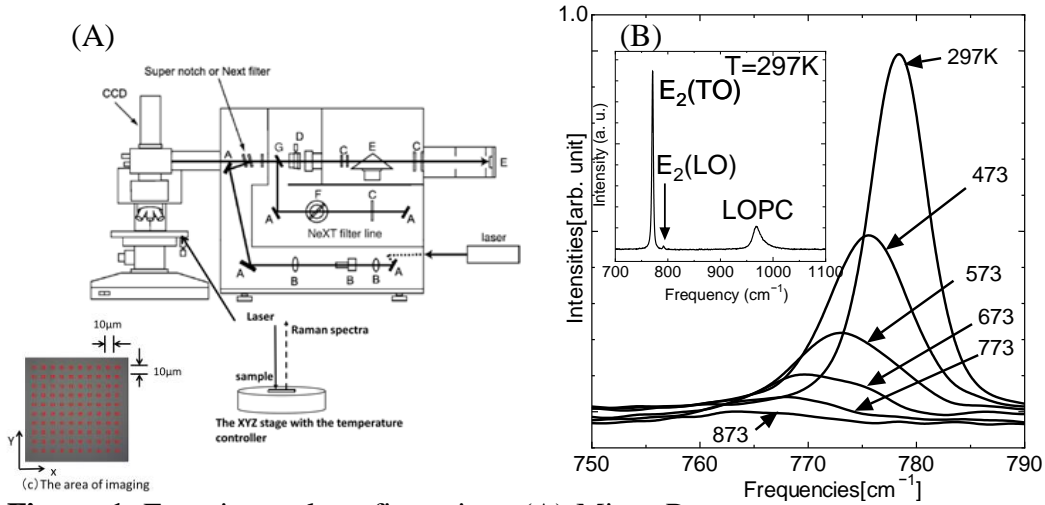


**Figure 1.** Experimental configurations (A) Micro-Raman spectroscopy system for high-temperature region, (B) Raman spectra of  $E_2(TO)$  of 4H-SiC with increasing temperature.

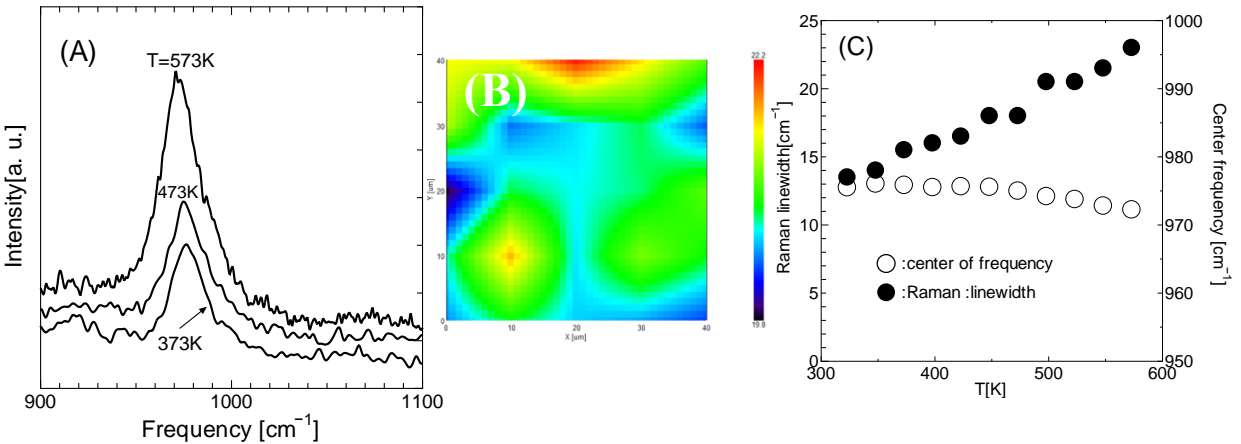


**Figure 2.** (A) Temperature dependence of Raman spectra of *LOPC* mode, (B) An example of the 2D-Raman imaging of *LOPC* mode ( $T=573K$ ), (C) The variation of average values of linewidth and center frequency over the imaging area with the temperature change.

[1] S. Nakashima, H. Harima, *Phys Status Solidi*. **1997**, 162 (1), 39-64.  
 [2] S. H. Yang, L: *Optics. Express*. **2013**, 21,26475-26482.  
 [3] T. Itoh *et al*, *R&D review of Toyota CRDL*.**1994**, 29 (4), 43-52.  
 [4] Y. Matsuo, D. Iyoda, J. Suda, *MES2016*, **2016**, 383-386.

# Investigation of mode Assignment on $\text{YVO}_4$ crystal in high temperature region by polarized Raman spectroscopy and first principles calculations

Jun Suda\*

101-2 Yagoto Honmachi, Showa-ku, Nagoya-shi, 466-8666, Japan  
Department of Electrical and Electronic Engineering, School of Engineering, Chukyo  
University

\*suda@sist.chukyo-u.ac.jp

Abstract Polarized Raman spectra for 11 modes in the  $\text{YVO}_4$  crystal were measured in the temperature range from room temperature to 473 K, and the mode assignment on Raman modes was analyzed using the first-principles calculations. We found that the calculated frequency values are in good agreement with the experimental ones. The large difference of the temperature line broadening between two peaks of  $A_{1g}$  mode was reported.

Recently, diode-pumped solid state lasers have attracted much attention and been widely applied to a number of fields such as military industry and so on. Among these solid states laser ceramics,  $\text{YVO}_4$  has been widely investigated for its high damage threshold, high conductivity good mechanical properties and chemical stability, which are important for solid states lasers [1]. However, the mode assignment in  $\text{YVO}_4$  has not been enough up to now. Recently, pressure-dependent Raman measurements were made by Manjón *et al* [2]. but still nine Raman-active modes were observed instead of the twelve predicted by the group theory. The mode assignment including twelve modes at only room temperature was made by Sanson *et al.* [3].

In the present work, we report on the results of a thorough vibrational dynamics study of  $\text{YVO}_4$  single crystal, consisting of highly symmetry-selective polarized Raman scattering measurements in the high temperature region and of first principles calculations. Polarized Raman-scattering spectra were measured from 290–473 K in all of the right-angle scattering geometry (Fig. 1) using a broadband polarization rotator (PR550, NEWPORT Company). The excitation source was the 532-nm line of a Diode laser at a power level of 100-200 mW. The scattered light was analyzed by a double monochromator (Spex-1403, Horiba-Jobin Company) with a spectral slit width of about  $1.0 \text{ cm}^{-1}$ . The sample was mounted inside a closed-cycle He-gas refrigerator (U102AW, DAIKIN Co.). Temperatures were measured with a gold-iron-Chromel thermocouple, and controlled by a temperature controller (DB1000, CHINO Co.). Accuracy of the wave number was within  $\pm 0.5 \text{ cm}^{-1}$ . The dimension of  $\text{YVO}_4$  single crystal with a purity of 99.99% is  $5 \text{ mm} \times 6 \text{ mm} \times 7 \text{ mm}$  (c axis). The polarized Raman spectra (Fig. 1(B)) in all alignments are obtained as the number of peaks of each mode ( $2A_{1g}+4B_{1g}+B_{2g}+5E_g$ ) without one  $E_g$  mode is predicted by the group theory. These center frequencies are in good agreement with calculated ones by first-principle calculations [4] within the deviation of 3.3%. Next, in the temperature dependence of higher and lower frequency peaks of the same  $A_{1g}$  mode in Figs. 2(A) and 2(B), the large difference of the temperature line broadening is thought to be due to band gap effect in PDOS [4]. In this

study, the vibrational properties of  $\text{YVO}_4$  have been investigated by means of both polarized Raman spectroscopy and first principles calculations. Symmetry selective measurements have been carried out using a micromanipulator to finely orient the crystal (the bottom of Fig. 1(A)). Through a proper polarization analysis, all the 11 Raman-active modes of  $\text{YVO}_4$  have been contrasted in turn and definitively assigned in symmetry.

The author is grateful to the Chukyo University Research Found (2014) for financial assistance with this research.

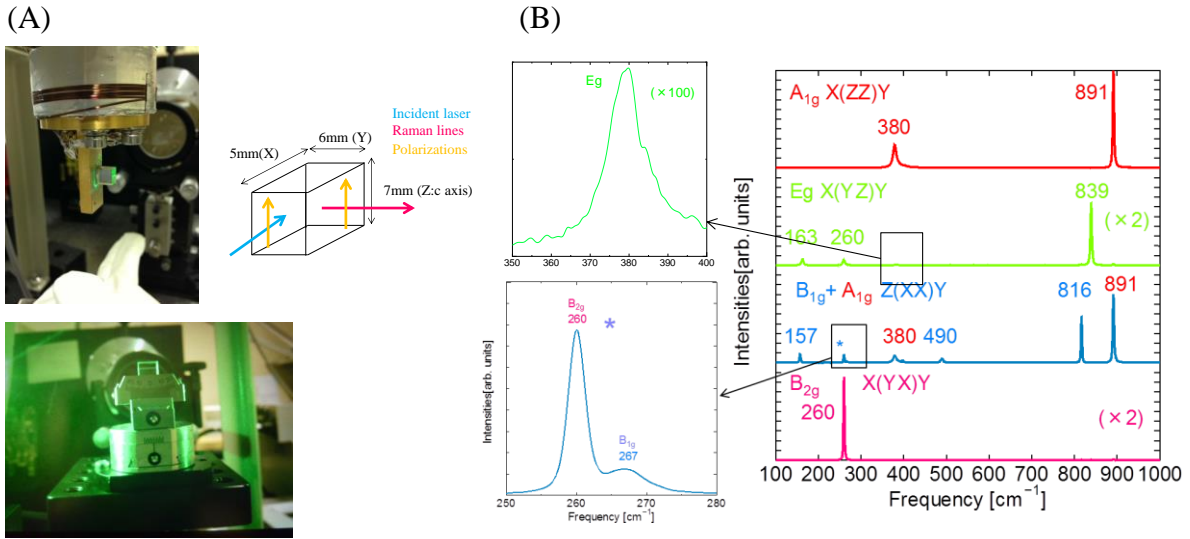


**Figure 1.** Experimental configuration illustrating (A) the alignments with two photographs of experiment, (B) polarized Raman spectra of all alignments in  $\text{YVO}_4$  at room temperature.

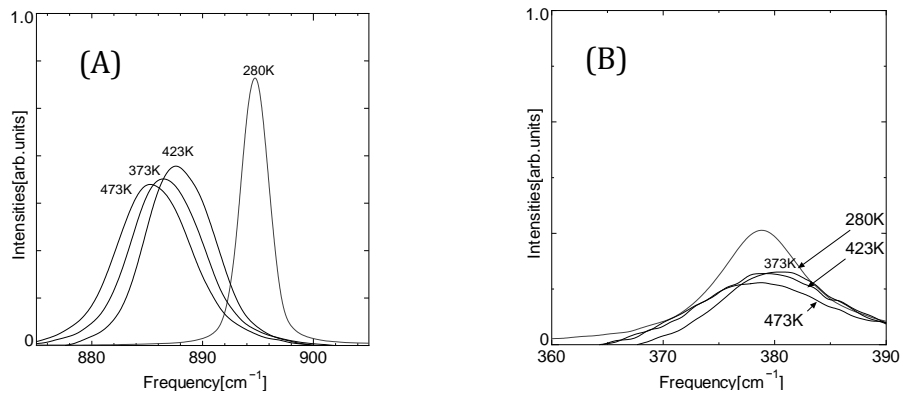


**Figure 2.** The Raman spectra for (A)  $A_{1g}$  mode ( $891\text{cm}^{-1}$ ) and (B)  $A_{1g}$  mode ( $380\text{cm}^{-1}$ ) with increasing temperature from room temperature up to 473K.

[1] P. G. Zverev, *J. Phys. Conf. Ser.*, **2007**, 92 012073  
 [2] F. J. Manjón *et al*, *Phys. Rev. B*, **2010**, 81, 075202.  
 [3] A. Sanson *et al*, *Phys. Rev. B*, **2012**, 86, 214305.  
 [4] J. Suda, submitted to *Solid State Commun.* **2017**.

# Investigation of Raman gain due to the line broadening for the highest $A_g$ mode in $PbWO_4$ in both low and high temperature regions by micro-Raman imaging

Jun Suda<sup>\*</sup>, Hirotaka Yamada

*101-2 Yagoto Honmachi, Showa-ku, Nagoya-shi, 466-8666, Japan  
Department of Electrical and Electronic Engineering, School of Engineering, Chukyo  
University*

*\*suda@sist.chukyo-u.ac.jp*

Abstract Raman images ( $24\mu\text{m}\times 24\mu\text{m}$ ) of  $PbWO_4$  crystal have been measured by micro-Raman Spectroscopy at temperature from 77K to 573K. The average values of Raman linewidth of the highest  $A_g$  mode ( $906\text{cm}^{-1}$ ) over the imaging area ( $100\mu\text{m}\times 100\mu\text{m}$ ) show broadening monotonously with increasing temperature. We have analyzed the relative Raman gain from the average values of Raman linewidth by Raman imaging in both high and low temperature ranges. We have evaluated temperature dependence of Raman gain of  $PbWO_4$  in comparison with the case of  $BaWO_4$ .

Recently,  $PbWO_4$  has been proposed as an excellent material for the implementation of Raman lasers due to the strong-scattering cross section of the highest  $A_g$  mode ( $906\text{cm}^{-1}$ ) of the scheelite structure [1]. It is interesting that the highest  $A_g$  mode in some scheelite crystals has different temperature dependence of linewidth in spite of a breathing mode [2-7]. Very recently, we reported that Raman linewidth of the  $72\text{cm}^{-1}$ , the  $191\text{cm}^{-1}$ , and the  $926\text{cm}^{-1}$  in the temperature range from 10 K to 295 K in the  $BaWO_4$  was analyzed using the lattice dynamical approach and found that different behaviors of these modes in the case of temperature broadening could be attributed to the large energy band gap resulting in different anharmonic interactions [5,6]. Furthermore it is interesting that the values of Raman gain for the highest frequency  $A_g$  mode would be dependent on the laser focus point of crystal due to the lattice defect of crystal. This leads to the significant lowering of Raman gain coefficient on the position of crystal and increasing SRS pump threshold intensity at even room temperature [5-7]. The aim of this study was to investigate the position of the surface of  $PbWO_4$  sample by using temperature dependence of Raman imaging measurements of phonon broadenings for the highest  $A_g$  mode at temperature from 77 to 573K. Also we report temperature dependence of calculated Raman gain in both low and high temperature regions by Raman imaging.

A confocal micro-Raman spectroscope system, NRS-4100 with a 2400 l/mm grating, was employed to study Raman linewidth of  $PbWO_4$  samples with temperature varying from 77K to 573 K. Spectral resolution of the system is up to  $0.4\text{cm}^{-1}$ . A Laser diode at 532 nm in wavelength was utilized for excitation. The accuracy of wavenumber is within  $\pm 0.1\text{cm}^{-1}$ . The transparent  $PbWO_4$  sample ( $10\text{mm}\times 10\text{mm}\times 0.5\text{mm}$  (c axis)) with double sides polished, it was prepared by Czochralski method. The Raman line broadening was proportional to temperature in the temperature range from 77K to 573 K (Fig. 1(a)). The position dependence of Raman imaging of linewidth in each temperature is within  $\pm 5\%$ . As shown in Fig. 2, in comparison with experimental data and the case of a  $BaWO_4$

Raman laser, we found the  $\text{PbWO}_4$  is heated due to Stokes losses, which results in lowering of the Raman gain due to the line broadening or the highest  $A_g$  mode during the operation of a Raman laser. The obtained results will allow us to predict the variation of Raman gain with temperature during the operation of a  $\text{PbWO}_4$  Raman laser.

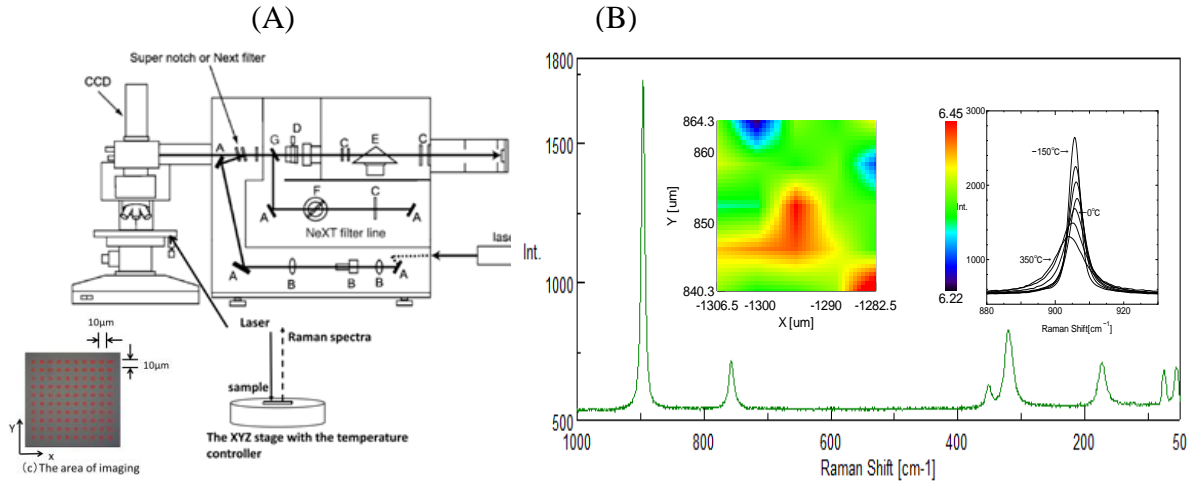


**Figure 1.** Experimental configurations (A) micro-Raman spectroscopy system for high-temperature region, (B) an example of 2D-Raman imaging of linewidth of the highest  $A_g$  mode of  $\text{PbWO}_4$  crystal at room temperature .

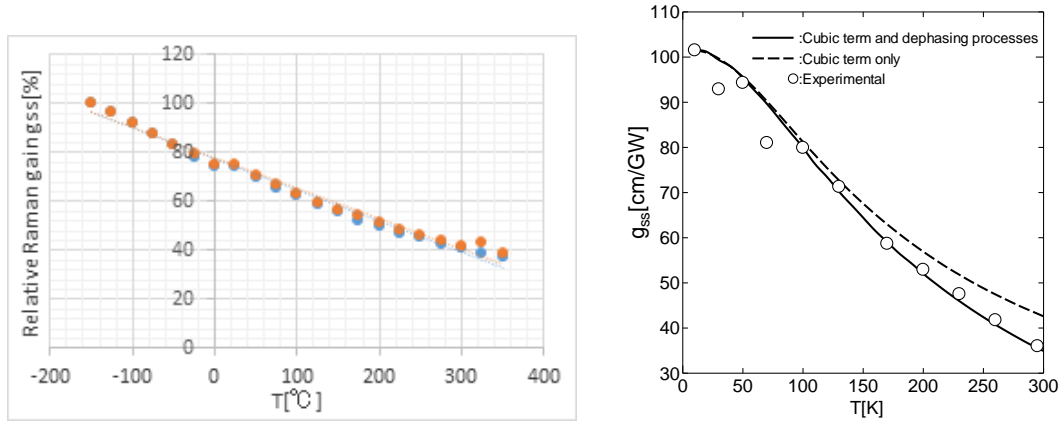


**Figure 2.** (A) temperature dependence of Raman gain of the highest  $A_g$  mode over the area of  $24\mu\text{m} \times 24\mu\text{m}$  on the surface of  $\text{PbWO}_4$  crystal in comparison with (B) the case of  $\text{BaWO}_4$  [8].

- [1] A.A Kaminskii *et al.*, *Opt. Commun.*, **2000**, 183, 277-287.
- [2] J. Suda, T. Sato, *J. Phys. Soc. Jpn*, **1997**, 66, 1707-1713.
- [3] J. Suda, P. G. Zverev, *Vib. Spectrosc.*, **2012**, 62, 85-91.
- [4] J. Suda, *Vib. Spectrosc.*, 2014, 72, 33-36.
- [5] J. Suda *et al.*, *Solid. State. Commun.*, **2014**, 192 36-41.
- [6] J. Suda, P. G. Zverev, *Vibrational Spectrosc.*, **2016**, 84, 127-132.
- [7] J. Suda, to be accepted to *Solid. State. Commun.*
- [8] J. Suda, P. G. Zverev, *31st Jap Laser Sensing symp. Abs of Papers* **2013**, 40-41

## HI 90 - Hyperspectral Imaging at a Long Distance

Thomas J Tague Jr.<sup>1,\*</sup>, and René Braun<sup>1</sup>

<sup>1</sup>*Bruker Corporation, 19 Fortune Drive, Billerica, MA 01821*

*\*tom.tague@bruker.com*

Stand-off hyperspectral infrared imaging allows the detection and mapping of both airborne and liquid compounds from long distances. It also provides information about the position, distribution, and propagation of a target compound. Gases can also be quantified and tracked from afar.<sup>1-2</sup>

The novel hyperspectral imager (HI90, Bruker Corporation) is based on the combination of a Michelson interferometer and a focal plane array detector, as shown in Figure 1. A spectrum is calculated for each pixel of the detector array. Each spectrum contains the infrared signature of the scene that can be used to analyze gases, liquids, and solids.

The interferometer of the imaging system has been designed specifically for highest throughput, maximum imaging performance, and excellent spectral quality. The moving mirror of the Michelson interferometer is aligned actively while changing the optical path difference at the same time. This interferometric system is highly efficient and results in hyperspectral image cubes that contain high quality spectra with outstanding signal-to-noise ratios.

In order to optimize the detection capabilities, spatial filtering may be applied. If a cloud fills the field of view of several adjacent pixels, this operation improves the signal-to-noise ratio. Various spatial filters such as Gaussian convolution filters or morphological filters are available. Furthermore adaptive identification thresholds are implemented using information from adjacent pixels.

The identification routines use massive parallelization to calculate the brightness temperature spectra and the identification routines quickly and efficiently. This allows identification and mapping in real time. The consecutive identification images of ammonia in Figure 2 show the dimension and the propagation of the ammonia cloud while two people pass by the release spot.

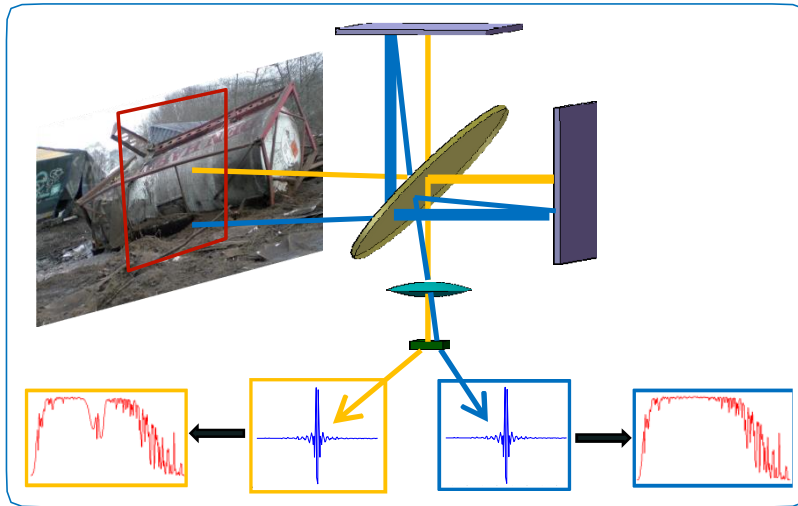


Figure 1 - Principle of an imaging Fourier transform spectrometer.

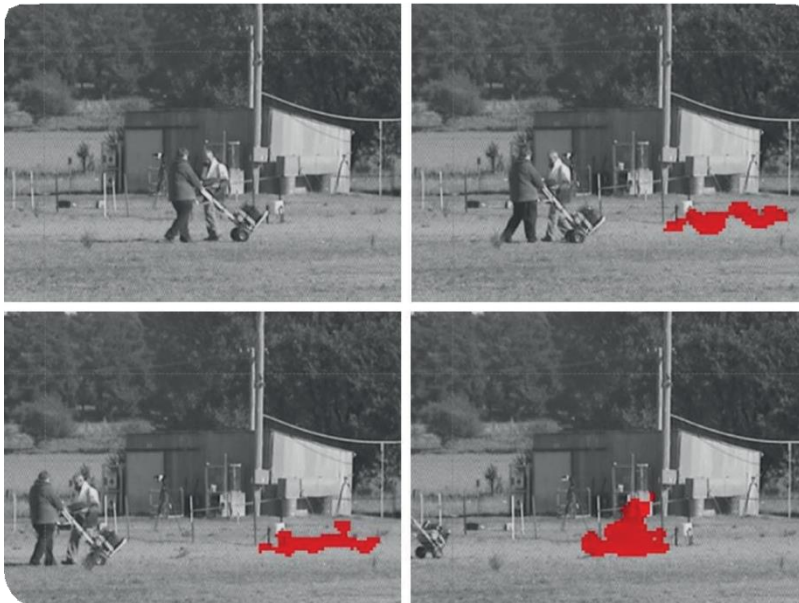


Figure 2 - Real time identification due to massive parallelization of the analysis routines.

#### References:

1. Sabbah, S., Harig, R., Rusch, P., Eichmann, J., Keens, A., Gerhard, J.-H.: "Remote sensing of gases by hyperspectral imaging: system performance and measurements", *Opt. Eng.* 51, 111717 (2012), DOI:10.1117/1. OE.51.11.111717".
2. Braun, R., Harig, R.: "Stand-off identification and mapping of liquid surface contaminations by passive hyperspectral imaging", *SPIE 871004* (2013)".

## Development of ATR Objectives for Wide-Area Micro-FTIR Imaging and Novel Micro-FTIR Imaging System

Kohei Tamura<sup>1\*</sup>, Miyuki Kanno<sup>1</sup>, Ken-ichi Akao<sup>1</sup>, Jun Koshoubu<sup>1</sup>, Hiroshi Sugiyama<sup>1</sup>,  
Keisuke Watanabe<sup>1</sup>, Koushi Nagamori<sup>1</sup>, Frank S. Weston<sup>2</sup>

<sup>1</sup>JASCO Corporation, 2967-5 Ishikawa-machi, Hachioji, Tokyo, 192-8537, JAPAN

<sup>2</sup>JASCO Incorporated, 28600 Mary's Court, Easton, MD, 21601, USA

\*kohei.tamura@jasco.co.jp

### Introduction

It has been over two decades since Fourier Transform Infrared Spectroscopy (FTIR) Imaging has come into common use due to the advancement of multichannel infrared microscopes. Over this period, in order to accommodate increasingly diverse sample shapes and measurement goals, products have been developed that focus on new and improved accessories and analysis algorithms.

JASCO has recently developed innovative IR imaging systems. First, we have developed the infrared light path scanning imaging system of Micro-FTIR; and, attenuated total reflectance (ATR) objectives have also been developed and redesigned. In this presentation, details of these systems are described and demonstrated with real world application results.

### Micro-FTIR Imaging System without Moving/Motorized Stage - IQ Mapping

The current JASCO Micro-FTIR has a proprietary function, 'IQ-mapping', which enables one to collect imaging data by scanning infrared light over a sample without moving a motorized sample stage (Fig. 1). In this system, we can obtain an imaging measurement over a large area without an automated XY stage which can add both method complexity and cost.

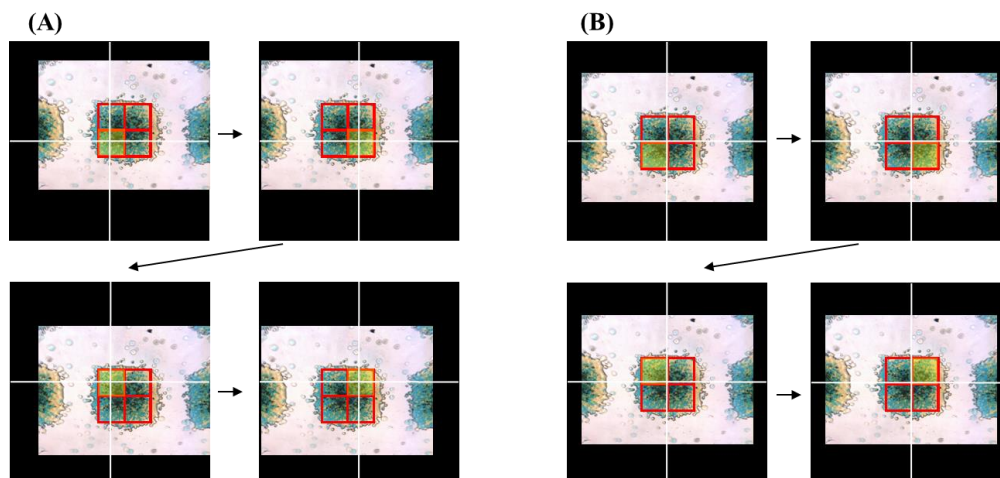


**Figure 1.** Comparison of imaging method (white crosshair: the center of a Cassegrain view, red frame: measurement area and aperture size, yellowed point: aperture and the point while measurement): (A) Conventional mapping, which a stage moves each time when a measurement point is changed, (B) IQ mapping, which a light beam is scanned.

### ATR Micro-FTIR Imaging System with ‘View-Through’ ATR Objective

In this system, in order to observe the sample through ATR prism when they are in intimate contact with one another, a Cassegrain objective is combined with an ATR prism made from zinc sulfide or diamond both of which are transparent the visible and infrared spectral regions. This proprietary JASCO design is referred to as a ‘View-Through’ ATR objective. Using this unique ATR objective enables visible-light and infrared chemical images be obtained simultaneously when it is in close contact with the sample. In addition, by coupling the ‘View-Through’ ATR objective and ‘IQ-Mapping’ techniques, we can obtain contact observation of the visible image and chemical imaging IR data in one contact and without moving a XY stage, so contamination does not occur. This saves time during sample measurements and minimizes the risk of a sample moving while exchanging objectives or the microscope light path.

Applications of this system include analysis of the particle distribution in oil samples and IR imaging of the interface between solids and liquids (Fig. 2).

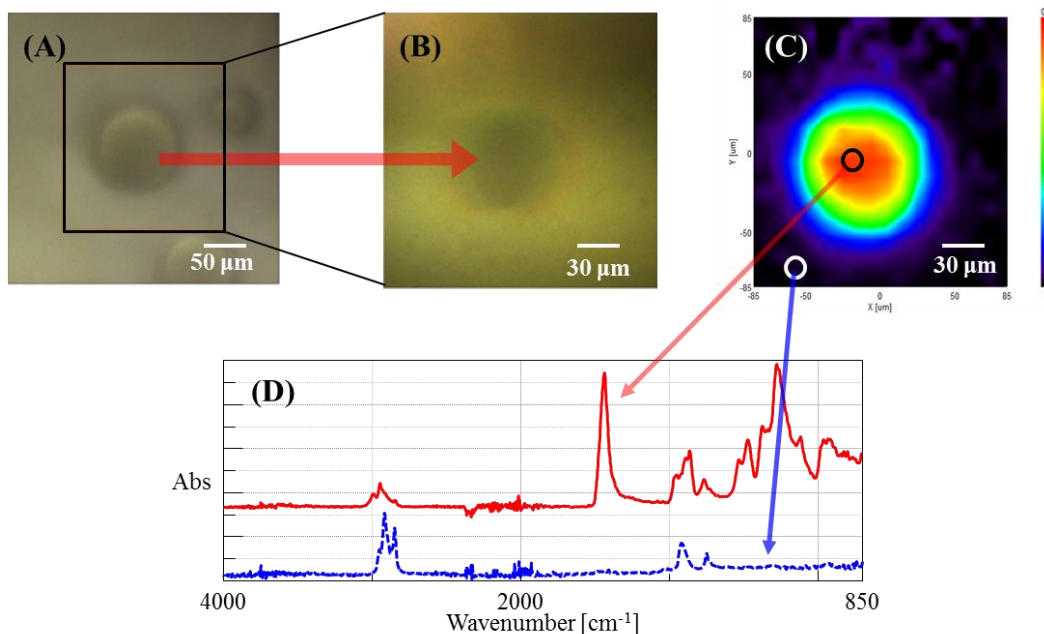


**Figure 2.** Overview of ATR Micro-FTIR imaging in one contact using ‘View-Through’ ATR objective and ‘IQ Mapping’: (A) visible image of the particle before contact, (B) visible image of the particle while contact, (C) distribution map of the particle, (D) spectra of each position

### ATR Micro-FTIR Imaging System for Wide-Area with High-Throughput

We have also developed another type ATR objective. This objective achieves high-throughput using a new design that enables wide-area imaging in one contact by combining with ‘IQ-mapping’ method.

Applications and details of this ATR objective will be reported in this presentation.

### Reference

- [1] Larsen, R. A.; Akao, K.; Koshoubu, J.; Tamura, K.; Sugiyama, H. *Spectroscopy* **2016**, *31*(8), 16-23.

**Raman geothermometer applied to low grade carbonaceous materials: case study from Culm Basin in the Nížký Jeseník Mts. (NE Bohemian Massif, Czech Republic–Poland).**

Aleksandra Weselucha-Birczyńska<sup>1\*</sup>, Dariusz Botor<sup>2</sup>, Tomasz Tobała<sup>2</sup>, Katarzyna Knobloch<sup>1</sup>

<sup>1</sup>*Faculty of Chemistry, Jagiellonian University, Ingardena 3, Krakow, Poland*

<sup>2</sup>*AGH- University of Science and Technology, Faculty of Geology, Geophysics and Environmental Protection, Mickiewicza 30, Kraków 30–059, Poland*

*\*birczyns@chemia.uj.edu.pl*

The irreversible process of coalification and graphitization of organic (carbonaceous) matter makes it possible to determine the degree of diagenesis and metamorphism in both sedimentary and very low– to low–grade metamorphic rocks [1,2]. The transformation of organic matter involves structural and compositional changes.

Besides estimated the maximum temperature from the mean random vitrinite reflectance (VRr) parameters, the Raman microspectroscopy of carbonaceous (organic) material has gained interest in the last decade, particularly for the low–grade metamorphic samples [3]. In this research Raman microspectroscopy was applied to investigate the thermal history of Lower Carboniferous Culm rocks of the Moravo–Silesian thrust–belt (Fig. 1). Because the detailed relations between tectonics and thermal evolution of this area is still poorly understood, the study of organic matter was undertaken. A total of 10 fine–grained rock (shale) samples from the Lower Carboniferous outcrops in the Nížký Jeseník Mts. were collected, Raman measurements were performed on polished rock slides (Fig 2). We have analyzed the first–order range 1000–1800 cm<sup>–1</sup> of Raman spectrum to estimate the thermal samples history.

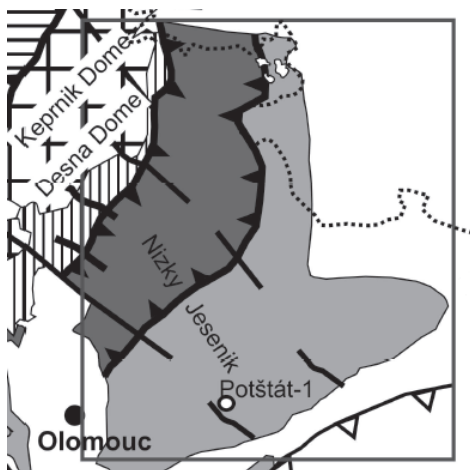


**Figure 1.** Simplified geological sketch map of the Moravo-Silesian Zone Location , Nížký Jeseník Mts.

There are at least five Raman bands in this range visible particularly well in the low-grade metamorphic rocks [4]. These bands are denominated as D1 ( $\sim 1350\text{ cm}^{-1}$ ), D2 ( $\sim 1620\text{ cm}^{-1}$ ), D3 ( $\sim 1500\text{ cm}^{-1}$ ), D4 ( $\sim 1250\text{ cm}^{-1}$ ) and G ( $\sim 1580\text{ cm}^{-1}$ ). The R2 area ratio ( $R2 = D1 / (G + D1 + D2)$ ) shows a linear correlation with the transformation temperature [3]. For the samples from Fig.2 temperature is estimated at  $196.4\text{ }^{\circ}\text{C}$ .

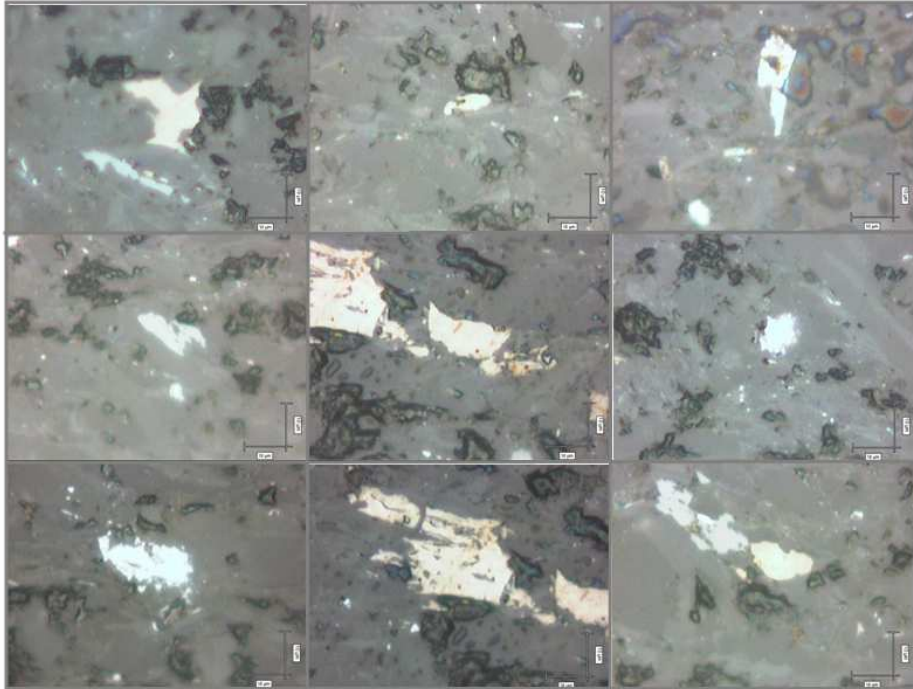


**Figure 2.** Exemplary samples from the the Moravo-Silesian Zone Location , Nízky Jeseník Mts.

- [1] Teichmüller, M., 1987. Organic material and very low-grade metamorphism. In: Frey M., (ed.) Low-temperature metamorphism. Chapman and Hall, New York: 114–161.
- [2] Hartkopf-Fröder, C.; Königshof, P.; Littke, R.; Schwarzbauer J. *Int. J. Coal Geol.*, **2015**, 150–151: 74–119.. *Nature Rev.* **2010**, 8, 623–633.
- [3] Beyssac, O.; Goffe, B.; Chopin, C.; Rouzaud, J. N. *J. Metamorph. Geol.*, **2002**, 20, 858–871.
- [4] Lünsdorf, N.K.; Dunkl, I.; Schmidt, B.C.; Rantitsch, G; von Eynatten, H. *Geostandards and Geoanalytical Research* **2014**, 38, 73–94.

## **Molecular Spectroscopic Troubleshooting of Stepwise Industrial Operation Efficiency via Quantitative Chemical Imaging.**

David L. Wetzel<sup>1\*</sup>, Mark D. Boatwright<sup>1</sup>

<sup>1</sup> *Microbeam Molecular Spectroscopy Laboratory, Kansas State University, Manhattan, KS, USA, 66506*

<sup>2</sup> *Department of Biochemistry & Molecular Biophysics, Kansas State University, Manhattan, KS, USA, 66506*

\**wetzellab@ksu.edu*

Efficient separation of high value products from byproducts on an industrial scale is an economic necessity. For low margin, high volume operations in particular, this is essential. The processing of plant material requires efficient separation of botanical parts. Each part has its own chemical identity. Employing quantitative vibrational spectroscopic imaging [1] enables direct determination of the high value, concentrated product at numerous stages of a typical complex, sequential industrial scale processing operation. The milling of wheat is a classical example and one of practical concern [2]. The current case for which operational efficiency and maximum yield are cited involves 44 product (flour) streams.

Quantitative chemical imaging with appropriate pixel size at wavelengths corresponding to the high value analyte and the vibrational spectrum background (Figure 1a) produce spatially resolved absorbance values for an x, y field of view. Absorbance weighted images reveal where and how much of a particular chemical species is present in a heterogeneous solid mixture. In the complex, sequential process cited; equipment settings imposed for the early separation processes influence successive operational steps downline. After each step, the various materials remaining that are sorted by particle size are subjected to rework by a successive operation. The material that is selectively refined and passes through the finest sieve is defined as flour.

Spectroscopic quantitative chemical imaging provides the basis for taking corrective action to achieve optimum operational efficiency and yield (Figure 1b). The weighted cumulative analyte purity plotted vs. the cumulative yield of flour product (example in Figure 1c) revealed multiple defects. In contrast, after corrective active, corresponding plots reveal an optimized result.

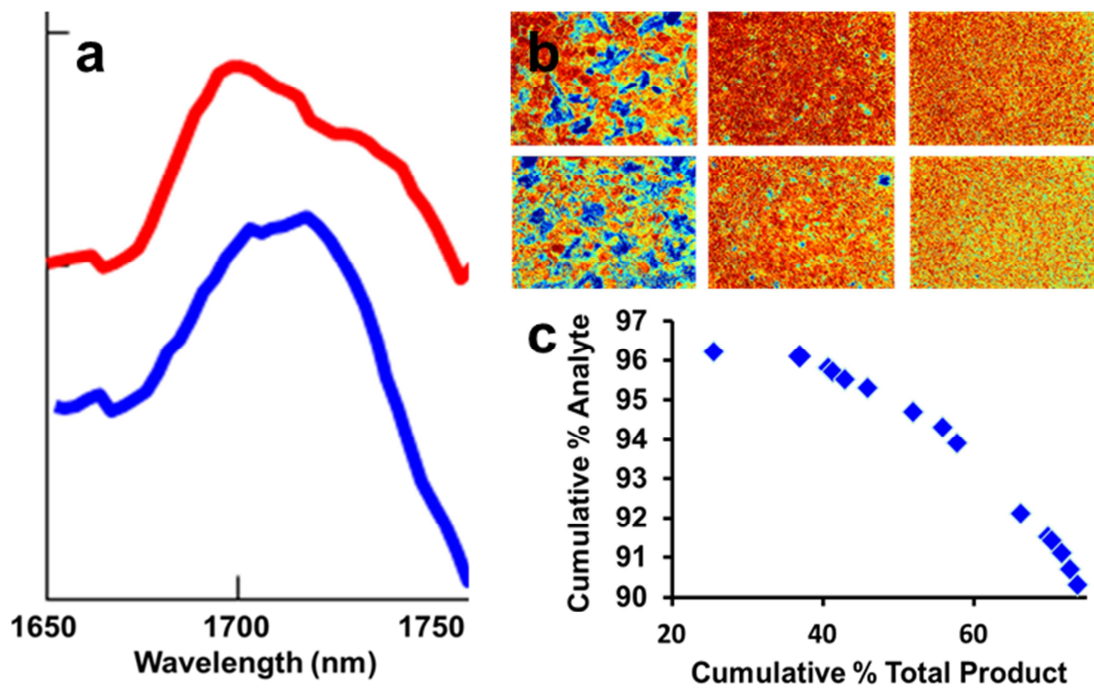


**Figure 1a.** Typical spectral band shapes of analyte (top) compared to offset spectra of the contaminant (bottom).

**Figure 1b.** Three product streams are shown for a unit process with optimized (top) and default (bottom) settings. Warm (red) false colors highlight the increased analyte concentrations in the optimized scheme.

**Figure 1c.** The weighted purity measurement after the addition of each individual product stream is plotted vs. the cumulative total amount of material to track the point at which product purity does not meet buyer specifications.

- [1] Lewis, E. N., Levin, I. W., and Treado, P. J. US Patent Application 5 528 368 (1996).  
 [2] Posner, E. S., and Hibbs, A. N. Wheat Flour Milling (AACC International, St. Paul, MN, 2004), 2nd ed.

## Design of new device for HPLC-FTIR Analysis

Shengnan Liu<sup>1,2</sup>, Lin Wang<sup>1,3</sup>, Ran Guo<sup>1,4</sup>, Anqi He<sup>1</sup>, Yanan Bao<sup>1,5</sup>, Yiwei Zeng<sup>1</sup>,  
Yongju Wei<sup>2\*</sup>, Yizhuang Xu<sup>1\*</sup>, Isao Noda<sup>1,6</sup>, Jinguang Wu<sup>1</sup>

<sup>1</sup> *Beijing National Laboratory for Molecular Sciences, State Key Laboratory for Rare Earth Materials Chemistry and Applications, College of Chemistry and Molecular Engineering, Peking University, Beijing 100871, P. R. China*

<sup>2</sup> *College of Chemistry and Material Science, Hebei Normal University, Shijiazhuang 050024, P. R. China*

<sup>3</sup> *Nanyang Institute of Technology, Nanyang, 473000, P. R. China*

<sup>4</sup> *College of Chemistry and Environmental Engineering, Shenzhen University, Shenzhen 518060, P. R. China*

<sup>5</sup> *Liaoning Technical University, Fuxin, 123000, P. R. China*

<sup>6</sup> *Department of Materials Science and Engineering, University of Delaware, Newark, Delaware 19716, United States*

In our previous work, we showed that CuO particles can be used as an ideal interface for HPLC/FTIR analysis<sup>1</sup>. Efforts have been devoted to develop a new technique to hyphenate HPLC and FTIR in our lab. A challenge for the hyphenation is as follows: The total concentration of analytes in an input sample for HPLC separation is below 0.1 wt%. After HPLC separation, different components in the mixed sample are further diluted. On the other hand, the absorptivity of an IR band in an FTIR spectrum is two to four magnitude lower than that of the transition band in a UV-Vis spectrum. Consequently, it becomes very difficult to obtain useful FTIR spectrum from the eluted samples after HPLC separation.

To address the problem, we developed a device containing CuO particles as an interface for accommodation of the elute that containing low concentration of analytes. The device is helpful for removing mobile phase and concentrate the dissolved analytes within a tiny sample spot, whose size is about 0.5 mm in diameter so that FTIR spectrum of analytes can be obtained.

We have tested the device by using a methanol solution containing 50 ppm benzamide. In experiment, we applied 100  $\mu$ l of methanol solution into the elution reservoir of the device. The solution is allowed to enter the capillary containing CuO particles.

Afterward, the device is put in a vacuum so that the mobile phase can be removed under vacuum and benzamide can deposit on exit of the capillary. Then FTIR spectrum of the CuO particles containing benzamide on the exit of the capillary was recorded under reflectance mode. The results is shown as trace a in Figure. 1. For comparison, FTIR spectrum of benzamide was also measured and shown as trace b in Figure 1. Characteristic peak of benzamide can be clearly observed in trace A of

Figure, indicating the device developed in this work is feasible for HPLC/FTIR analysis. Further work is still being performed.

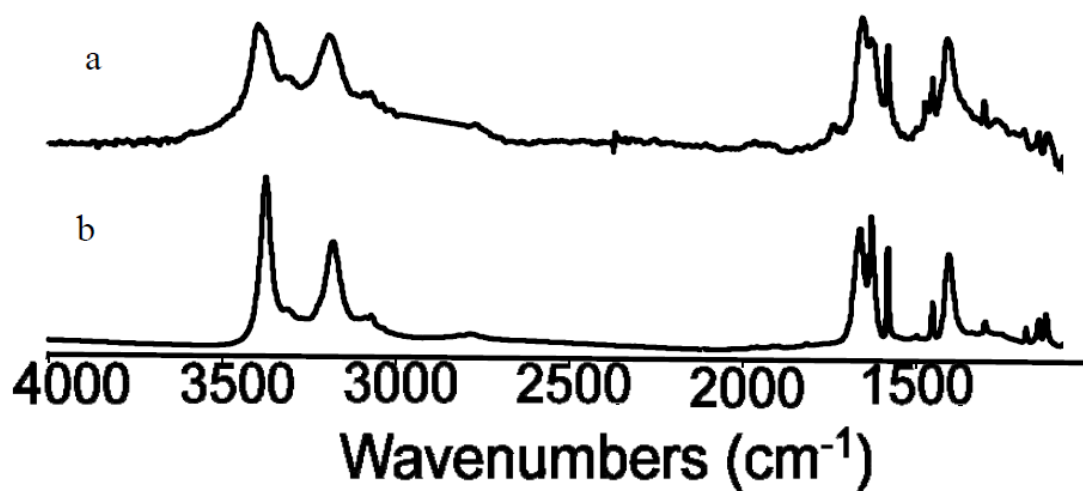


Figure 1 FTIR spectra of the benzamide. Trace a FTIR spectrum of benzamide deposit from 100 µl methanol solution containing 50 ppm of benzamide at the exit of the capillary of the device Trace b FTIR spectrum of standard benzamide sample.

[1] Li. Y. et al., *Anal. Sci.* **2017**, 323, 105

## **Raman Spectroscopy Method for Large Area and Through Barrier Measurements**

Jun Zhao, Jack Zhou

*B&W Tek*

*19 Shea Way, Newark, Delaware, USA, 19713*

*\*[junz@bwtek.com](mailto:junz@bwtek.com)*

A new Raman measurement method is developed that expands the applicability of Raman to See\_Through diffusely scattering media such as opaque packaging materials, biological tissues, as well as to thermolabile, photolabile, or heterogeneous samples.

Traditional Raman fiber optics probes employ a focused design similar to confocal microscopes. This confocal design has the advantage of maximum throughput. However, when the container diffuses the light strongly, light can no longer be focused inside the container, the confocal approach loses its effectiveness. Spatially Offset Raman Spectroscopy intentionally offsets the excitation beam and collection beam, and can be used effectively to collect Raman signal generated underneath diffusive top layers while largely avoiding their signature from overwhelming that of the sample. However, probes of such design cannot be easily used in a confocal arrangement and are generally inefficient for direct sample measurements.

The See\_Through Raman configuration illuminates and collects the Raman scattered light from a large sample area with enhanced throughput. This greatly increases the effective sampling depth, allowing the measurement of material inside visually opaque containers via a similar mechanism as SORS. The large area also has the additional advantage of preventing sample damage by reducing the power density, as well as improving accuracy by eliminating heterogeneous effect. With its high throughput design, the See\_Through analyzer provides identity of common chemicals through thick packaging material in seconds. For normal measurements, a range of accessories can be used in the confocal configuration for different applications including microscopy and stand-off Raman. This flexibility makes the See\_Through Raman a suitable technique for a variety of applications, from material ID to demanding research.

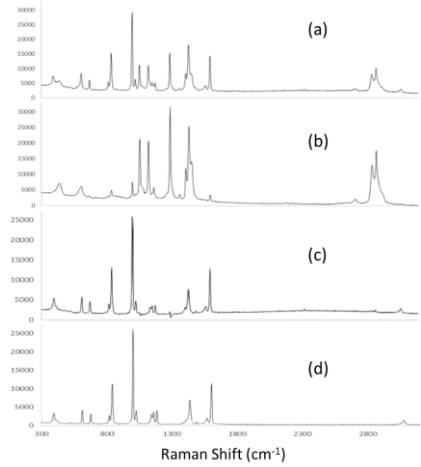


**Figure 1.** See\_Through Raman for identification of sodium benzoate through a white polyethylene plastic bottle: (a) Spectrum measured through the bottle using the See\_Through probe; (b) spectrum measured with a standard focus probe; (c) the result of scaled subtraction of (b) from (a); and (d) pure spectrum of sodium benzoate.

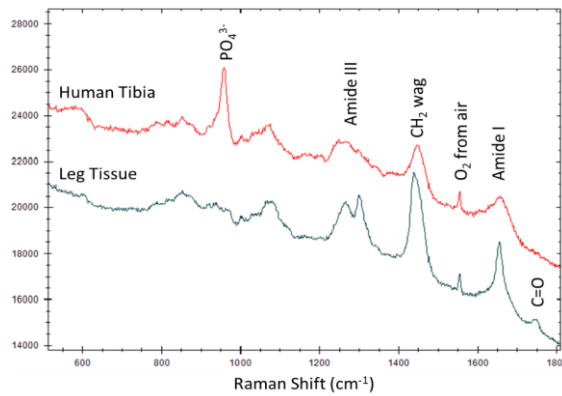


**Figure 2.** Transcutaneously collected Raman spectra of human tibia and leg tissue.

## Raman Spectroscopy in Medical and Health Science Application

Hidetoshi Sato<sup>1</sup>, Akinori Taketani<sup>1</sup>, Bibin B. Andriana<sup>1,\*</sup>, Hiroko Matsuyoshi<sup>1</sup>,  
Yasuhiro Maeda<sup>2</sup>, and Satoshi Wada<sup>2</sup>

<sup>1</sup>*School of Science and Technology, Kwansei Gakuin University  
2-1, Gakuen, Sanda, Hyogo, 669-1337 JAPAN*  
<sup>2</sup>*Photonics Control Technology Team, RIKEN  
2-1, Hirosawa, Wako, Saitama, 351-0198 JAPAN*  
*\*cyd56987@kwansei.ac.jp*

Raman spectroscopy is one of the most powerful tools to detect physiological activity of live cells and tissues. It does not require any labeling in the sample to observe molecular dynamics. We have developed instruments and techniques for medical Raman applications. Despite the high performance of Raman spectroscopy, there are very few applications practically used in medical and clinic. In the present study, we expand the application of the Raman techniques into health science as well as medical use and discuss about directions of biomedical Raman spectroscopy.

Miniaturized Raman probes were developed for endoscopic applications. Micro-Raman probe (MRP) consists of glass fibers.<sup>1</sup> Its working distance is able to select in the range from 200 to 1000  $\mu\text{m}$  by tuning focal length of a lens at the probe top. The other Raman probe is ball lens top hollow optical fiber Raman probe (BHRP).<sup>2</sup> A hollow optical fiber is made of glass tube in which inner surface is covered with very smooth silver mirror. Since it propagates light by reflection, there is no core material generating useless Raman signal. The excitation light and collected light is delivered bi-directionally with 1 fiber. The hollow fiber has so low aperture ( $\text{NA} \approx 0.07$ ) that the transferred light makes relatively small focal point by a lens at the distal end. In case of BHRP, a ball lens made of sapphire glass or quartz is used because they generate low fluorescence and Raman scattering light. The working distance of BHRP which is selected by changing diameter and material of the ball lens is within a range from 30 to 800  $\mu\text{m}$ . The total diameter of these Raman probes are about 600  $\mu\text{m}$ , which is enough narrow to put in vascular endoscope and injection needle.

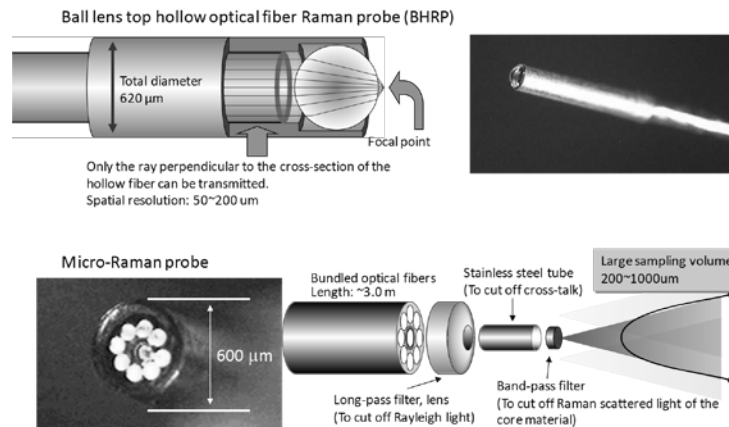


**Figure 1.** Schematic of BHRP and MRP

It is, however, difficult to apply for human because these applications are invasive to patients. Hence, we applied BHRP for noninvasive fat analysis. Accumulation rates of different fats were estimated in diet controlled hamsters based on Raman spectra of subcutaneous fat.<sup>3</sup>

**Table 1.** Accumulation rates of TL and TC in VAT, SAT and skin per two weeks.

Average accumulation rate (%) per 2weeks		
trilinolein in TL-treated group	visceral adipose tissue (VAT)	4.45±1.6
	subcutaneous adipose tissue (SAT)	4.37±2.4
	skin-subcutaneous (skin-SAT)	4.57±3.41
tricaprin in TC-treated group	visceral adipose tissue (VAT)	0.58±0.4
	subcutaneous adipose tissue (SAT)	0.52±0.38
	skin-subcutaneous (skin-SAT)	0.63±0.3

For practical application in medical field, Raman imaging is required for better understanding of medical doctors. The golden standard of diagnosis is histopathology, in which doctors interpret the pattern of the tissue structure. In a Raman mapping image, each pixel in the image has a spectrum. It is possible to draw an image based on the spectral analysis. We have succeeded in building a pseudo-HE stained picture. As it was possible to detect cancer tissue by analyzing Raman spectra with multivariate analysis, it was possible to identify cancerous area in a Raman image of human oral cancer tissue.<sup>4</sup> The most critical weakness of the conventional Raman imaging is long acquisition time. It sometimes takes more than 10 h to obtain a good quality image. To improve the situation, we undertake a development of stable and simple coherent antistokes Raman scattering (CARS) imaging technique. An electronically tuned Ti:sapphire laser (ETL) was improved to generate 2 wavelengths of laser light in a single resonator.<sup>5</sup> It was succeeded in measuring a full range CARS spectrum in 300 ms using the ETL. It will contribute to reduce acquisition time of Raman image.

Raman spectroscopy is opening a new era in biomedical field. Raman spectroscopy is very powerful and have a broad spectrum of application. Therefore, it is necessary to find out the really effective targets to apply. In the presentation, our developments of new Raman techniques and instruments will be introduced and discuss how it is useful and effective in which application for medical and health science.

- [1] Komachi, Y.; Sato, H.; Aizawa, K.; Tashiro, H., *Appl. Opt.*, **2005**, *44*, 4722-4732.
- [2] Katagiri, T.; Yamamoto, Y.S.; Ozaki, Y.; Matsuura Y.; Sato, H. *Appl. Spectrosc.*, **2009**, *63*, 103-107.
- [3] Meksiarun, P.; Andriana, B. B.; Matsuyoshi, H.; Sato, H. *Sci. Rep.*, **2016**, *6*, 37068.
- [4] Ishigaki, M.; Maeda, Y.; Taketani, A.; Andriana, B.B.; Ishihara, R.; Wongravee, K.; Ozaki, Y.; Sato, H. *Analyst*, **2016**, *141*, 1027-1033.
- [5] Sato, H.; Saito, N.; Akagawa, K.; Wada, S.; Tashiro, H. *J. Near Infrared Spectrosc.*, **2003**, *11*, 295-308.

# Analysis of carbamate pesticides on silica surface using sum-frequency generation spectroscopy

Jerry Cartagena-Brigantty, Leander Bromley III, Luis Velarde\*

Department of Chemistry, University at Buffalo, The State University of New York, Buffalo, New York 14260-3000, United States

*lvelarde@buffalo.edu*

According to the Environmental Protection Agency (EPA) over 1 billion pounds of pesticides are used in the United States (US) each year and approximately 5.6 billion pounds are used worldwide [1]. Carbamate insecticides are widely used in homes, gardens, and agriculture. There are some factors that affect the fate of a pesticide in the environment: Properties of the pesticide such as water solubility, soil adsorption, volatility, persistence; properties of the soil (texture, permeability, organic matter content); conditions of the site and management practices. Usually, a certain pesticide must move within the soil to reach the germinating seeds. Much movement can lead to reduced pest control, contamination of surface and groundwater and injury of other species, including humans. The ways pesticides can be transferred from one environment component to another are by adsorption/desorption, volatilization, runoff, leaching and uptake. The affinity between pesticide molecules and soil particles is dependent on soil properties, and properties of the pesticide. Therefore, it is important to study the adsorption and different molecular level interactions between the pesticide and soil particles. Silica is used as a model system of minerals found in the soil. To do so, Sum-Frequency Generation (SFG) spectroscopy will be performed.

SFG is a second-order coherent optical probe capable of providing a wealth of molecular-level information with high surface selectivity. SFG occurs when two pulsed laser beams, one of fixed visible frequency, ( $\omega_{\text{VIS}}$ ), and the other of tunable infrared frequency, ( $\omega_{\text{IR}}$ ), achieve spatial and temporal overlap at an interface [2]. Light is emitted at the sum of the two incident frequencies ( $\omega_{\text{SFG}} = \omega_{\text{IR}} + \omega_{\text{VIS}}$ ) as shown in figure 1. This surface selective vibrational spectroscopy is a powerful technique to obtain direct measurements of molecular interfaces with high sub-monolayer sensitivity. This technique has been successfully applied to various environmental interfaces such as air/water interfaces, mineral surfaces and organic aerosols.

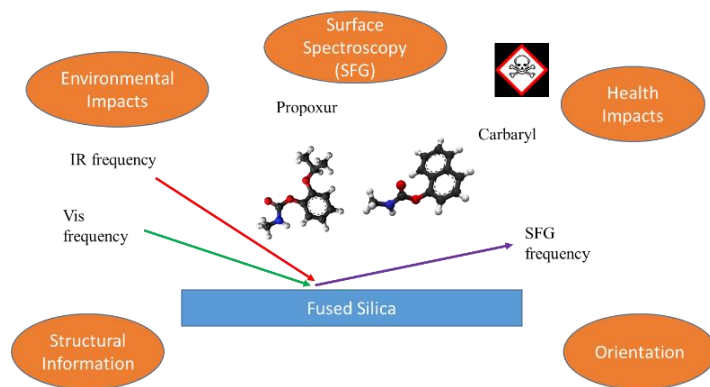


**Figure 1.** Schematic diagram showing SFG operation principle.

We want to collect spectroscopic measurements of Propoxur and Carbaryl at the air/silica interface. Also, we want to employ surface-selective non-linear vibrational spectroscopy to identify the vibrational signatures of the interfacial species. Different IR regions will be covered. Due to the molecular nature of these carbamate pesticides, special attention will be placed on C=O stretches ( $\sim 1730\text{cm}^{-1}$ ), N-H stretches in the  $3300\text{-}3400\text{ cm}^{-1}$  region as well as C-H stretches in the  $2800\text{-}3100\text{ cm}^{-1}$  region. The spectra of the data obtained in the C-H and C=O regions are shown in the figure 2. SFG will be used in multiple polarization combinations to identify the chemical structure, orientation and adsorption motifs of these pesticides on fused quartz.

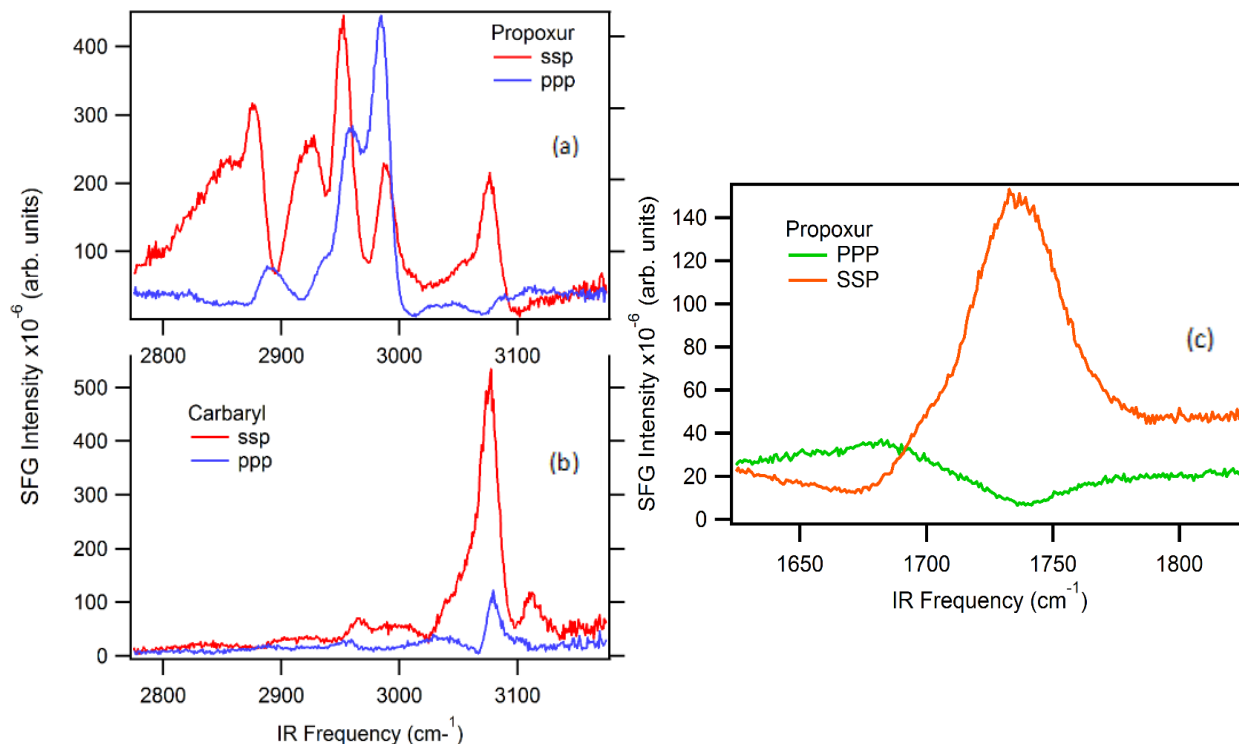


**Figure 2.** C-H stretching normalized SFG spectra at the air/silica interface: (a) propoxur and (b) carbaryl. (c) C=O stretching normalized SFG spectra of propoxur at the air/silica interface. SSP and PPP polarizations were recorded for each spectrum.

## References

- [1] Alavanja, M. *Rev Environ Health*. **2009**, *24*, 303–309.
- [2] Lambert, A. G.; Davies, P. B.; Neivandt, D. J. *Appl. Spectrosc. Rev.* **2005**, *40*, 103-145.
- [3] Wang, H. F.; Gan, W.; Lu, R.; Rao, Y.; Wu, B. H. *Int. Rev. Phys. Chem.* **2005**, *24*, 191-256.
- [4] Casillas-Ituarte, N. N.; Allen, H. C. *Chem. Phys. Lett.* **2009**, *483*, 84-89.
- [5] Covert, P. A.; Hore, D. K. *Annu. Rev. Phys. Chem.* **2016**, *67*, 233–57.

## Molecular structure in thin wetting films studied by linear and non-linear vibrational spectroscopy techniques.

Laetitia Dalstein\*, Jonathan F.D. Liljeblad and Eric Tyrode  
Department of Chemistry, KTH Royal Institute of Technology, SE-100 44,  
Stockholm, Sweden  
\* dalstein@kth.se

Thin wetting liquids films are of the utmost importance in a wide range of industrial applications such as froth flotation, surface cleaning processes and oil recovery operations [1]. The stability of these films, which typically range between a few to hundreds of nanometers, depends on the molecular interactions between the two interfaces that macroscopically manifest themselves as surface forces. For measurements, in particular those using the thin film pressure balance (TFPB), [2] has provided valuable insight in the identification of the different types of interactions. However, the link between the measured macroscopic forces and their molecular origin remains ambiguous, as force measurements provide no direct chemical, structural or conformation information, which are expected to change significantly in confined geometries.

Here we address this gap by making use of two surface sensitive and complementary vibrational spectroscopy techniques, TIR Raman (Figure 1, B) and Sum Frequency (Figure 1, C), to target *in situ*, structural changes in thin wetting films formed inside a TFPB apparatus (Figure 1, A). TIR Raman detects all molecules within the evanescent field while the coherent VSF is particularly sensitive to molecules located in the first few nanometers of the two interacting surfaces: solid/liquid and liquid/air.

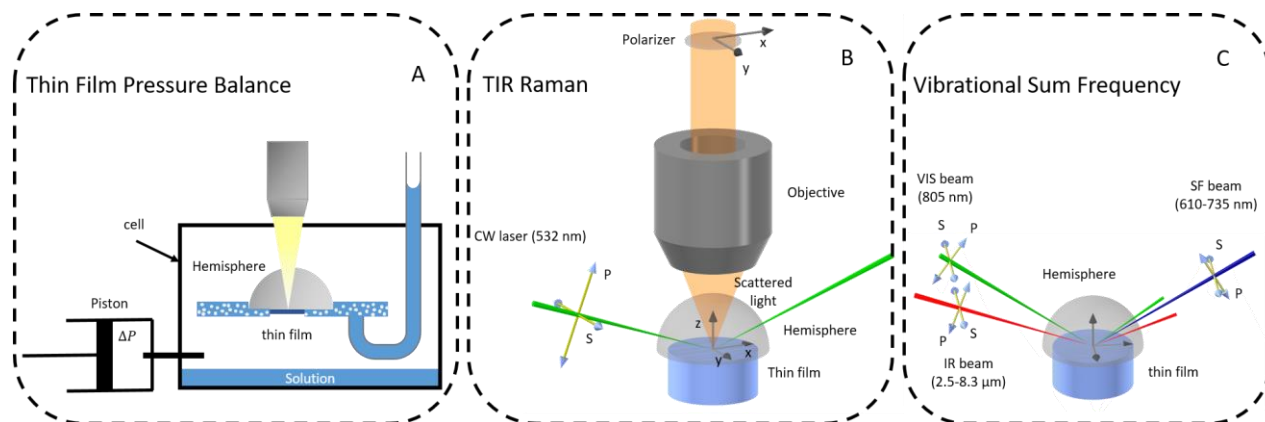


**Figure 1.** Illustrations of the different setups. (A) Thin Film Pressure Balance; (B) TIR Raman, (C) Vibrational Sum Frequency.

The asymmetric films studied consisted of surfactant aqueous solutions (SDS) confined between a solid support (fused silica) and air. The force curve (Figure 2, A) shows that the thickness is almost constant when the thin film is stable and homogeneous. The modeling of the measured TIR Raman response (Figure 2, B) provides a more precise value of the local thickness during the stabilization of the film. At equilibrium, we can

compare the Vibrational Sum Frequency signal from films of various thicknesses (Figure 2, C) and inferred contributions from the individual charged interfaces.

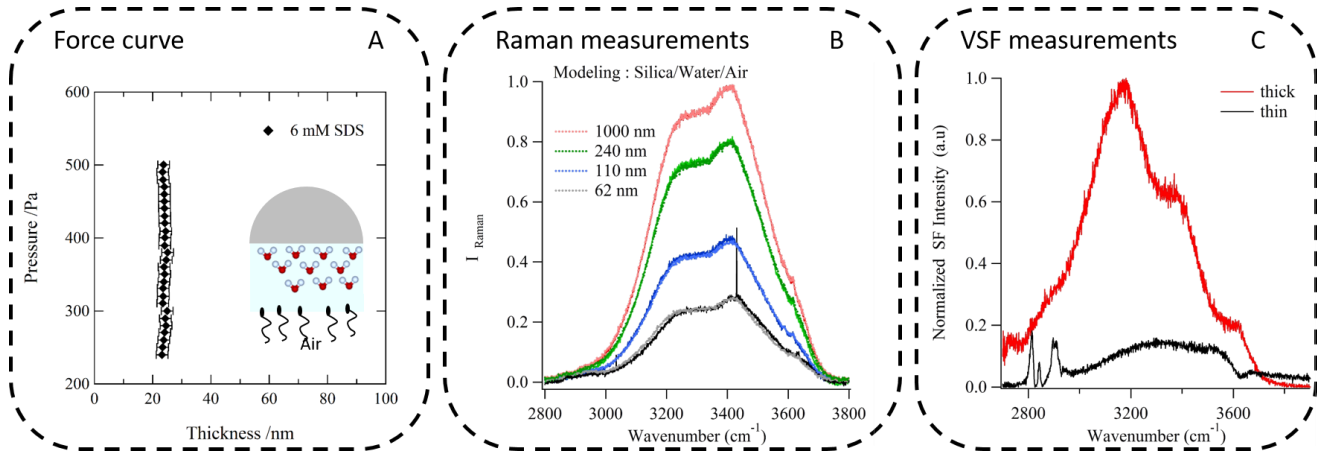


**Figure 2.** Results obtained with the three setups. (A) The force curve is showing the pressure versus film thickness for a silica/6mM SDS/Air system. (B) Evolution of the TIR Raman intensity for different thicknesses: the modeling's results are added for comparison and provide an estimate of the local thickness. (C) Vibrational Sum Frequency spectra for a thick (red) and a thin ( $\approx 22$  nm, black).

Results are discussed in terms of molecular structural changes observed in the surfactant monolayer and the interfacial water molecules at both interfaces as a function of the film thickness.

- [1] R. von Klitzing, *Advances in Colloids and Interface Science*, **2005**, 114-115, 253.
- [2] P.M. Claesson, T. Ederth, V. Bergeron and M.W. Rutland, *Advances in Colloids and Interface Science*, **1996**, 119-183, 67

## Self-Assembled Monolayer of Negatively Charged Surfactant at Air-Water Interface Influences the Interfacial Affinity of Cations

Sudipta Das<sup>\*</sup>, Mischa Bonn, Ellen H. G. Backus

*Max Planck Institute for Polymer Research, Ackermannweg 10, 55128 Mainz, Germany*

*<sup>\*</sup>das@mpip-mainz.mpg.de*

Owing to the ability to be adsorbed at various interfaces surfactants find applications in various industrial and biological processes. One particularly popular application is the use of surfactants as detergents in, for example, shampoos and soaps etc. Both to study surfactant action, and to understand the effect of surfactants released in the environment, much research has been aimed at understanding different aspects of its working properties. Of particular interest is the interaction of surfactants with water. A recent study has shown that water in contact with a self-assembled monolayer (SAM) of sodium dodecyl sulfate (SDS), a surfactant with negatively charged head group (R-O-SO<sub>3</sub><sup>-</sup>), forms two distinct sub-ensembles. One of these ensembles exhibits more delocalized O-H stretch vibrations than the other<sup>1</sup>. Although that particular study provides useful insights into the interaction between a SDS-SAM and pure water, information about the behavior of aqueous interfaces of ionic solutions in vicinity of such charged surfactant-SAMs have not been equally well studied, despite the ubiquity and importance of such systems. Particularly, specific cationic effects in solutions in contact with highly charged surfaces are known to influence the surface tension of electrolyte solution, phase transition of surfactants, etc.

Here, we elucidate the interfacial affinity of cations with a highly charged interface composed of a self-assembled SDS monolayer. We applied vibrational sum frequency generation (VSFG) spectroscopy to study the SDS-aqueous ionic solution interface and quantify the interfacial affinity of sodium and deuterium ions. In our VSFG experiment the sample is impinged by an infrared laser pulse and an 800 nm laser pulse up-converting the vibrational signal to a virtual state from which the sum-frequency light will be emitted. As this is a second-order process it is forbidden in centrosymmetric media like bulk water. At the interface the symmetry is broken, making the method surface specific. If the infrared pulse is in resonance with a molecular vibration, the signal is strongly enhanced. Here we focus on the O-D stretch vibration of heavy water (D<sub>2</sub>O) molecules. The intensity of the O-D stretch signal reflects the amount of aligned interfacial water molecules: the more the water molecules are aligned, the higher is the signal. Owing to the strong electric field exerted by the R-O-SO<sub>3</sub><sup>-</sup> groups, vicinal water molecules strongly orient themselves with their H-atoms towards the head groups ("O-H up orientation")<sup>1</sup>, resulting in a large VSFG signal. Due to ionic interactions between the R-O-SO<sub>3</sub><sup>-</sup> and cations, this electric field is expected to weaken, resulting in reduced alignment of interfacial water molecules and thus a reduction of the SFG signal. We compare SFG spectra at constant ionic strength but with different ratios of Na<sup>+</sup> and D<sup>+</sup> in the water sub-phase. From the change in SFG intensity, we conclude that in presence of SDS-SAM the interfacial affinities of the cations sodium and deuterium are reversed

compared to that at the bare air-water interface. The results indicate that specific ion effects are important to determine the interfacial electric charge of electrolyte solution at charged interfaces.

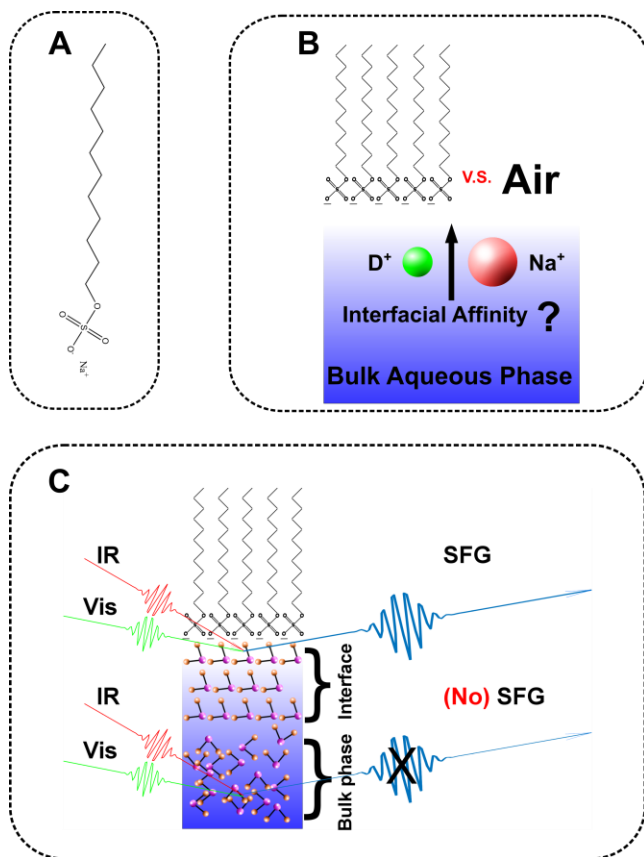


**Figure 1.** (A) Chemical structure of sodium dodecyl sulfate (SDS), (B) Schematics of the question of interest, and (C) Interfacial specificity of SFG.

[1] Livingstone, R. A.; Nagata, Y.; Bonn, M.; Backus, E. H. G., *J. Am. Chem Soc.* **2015**, *137* (47), 14912-14919.

# Compact broadband vibrational sum-frequency generation spectrometer at 100 kHz

Zsuzsanna Heiner<sup>1,2,\*</sup>, Freeda Yesudas<sup>1</sup>, Valentin Petrov<sup>3</sup>, Mark Mero<sup>3</sup>

<sup>1</sup>*School of Analytical Sciences Adlershof, Humboldt Universität zu Berlin, Albert-Einstein-Str. 5-11, 12489 Berlin, Germany*

<sup>2</sup>*Department of Chemistry, Humboldt Universität zu Berlin, Brook-Taylor-Str. 2, 12489 Berlin, Germany*

<sup>3</sup>*Max Born Institute for Nonlinear Optics and Short Pulse Spectroscopy, Max-Born-Str. 2a, 12489 Berlin, Germany*

\**heinerzs@hu-berlin.de*

Broadband sum frequency generation (BB-SFG) spectroscopy is a versatile technique that provides detailed information on the composition, orientation, conformation, interactions, and dynamics of molecules at surfaces and interfaces [1]. The study of organic molecules with the fundamental stretching modes of their O-H, N-H, C-H bonds in the 2.7-3.6- $\mu\text{m}$  spectral region can tremendously benefit from broadband, ultrafast, high-repetition-rate sources with pulse energies at the few- $\mu\text{J}$  level. The broad bandwidth is especially crucial, as it makes single-shot acquisition of entire vibrational regions possible without laboriously scanning the wavelength of a narrowband off-resonant source. Optical parametric amplifiers (OPAs) driven by diode-pumped ps and sub-ps Nd-/Yb-laser systems to generate radiation at the blue edge of the mid-infrared are gaining wide popularity due to their lower cost, greater simplicity, and more straightforward scalability towards high average powers [2] compared to systems based on traditional Ti:sapphire pump laser technology [3].

Here, we demonstrate a way for implementing a robust, 100-kHz light source for BB-SFG spectroscopy at a significantly reduced cost for the chemically important mid-infrared spectral range around 3  $\mu\text{m}$ . Utilizing a pump pulse energy of only 60  $\mu\text{J}$  from a compact, turn-key Yb:KGW master oscillator power amplifier system (Pharos-SP, Light Conversion Ltd.), the source delivers both the broadband infrared pulses and the narrowband visible pulses with ample energy for applications. The BB-SFG scheme is shown in Fig. 1a. A pulse energy of 20  $\mu\text{J}$  is used to create narrowband visible pulses, while the remaining 40- $\mu\text{J}$  portion is used for seeding and pumping a two-stage OPA. To generate the narrowband visible pulses from the femtosecond pump laser, we used a special chirped sum-frequency mixing scheme and obtained 5- $\mu\text{J}$ , 3- $\text{cm}^{-1}$ -bandwidth, transform-limited picosecond pulses around 515 nm with excellent beam quality. The pulses are slightly tunable between 511 and 519 nm. For seeding OPA#1, supercontinuum pulses were generated in the wavelength range of 1300 - 1700 nm, which (i) allows simple dispersion management based on bulk materials and (ii) provides a straightforward way for the synchronization between the narrowband visible and the infrared pulses. The pre-amplifier and the booster amplifier are based on anti-reflection (AR) coated, 5% MgO-doped, fan-out PPLN crystals. Despite using moderate pump peak intensities of only 45 and 40  $\text{GW}/\text{cm}^2$ , the conversion efficiencies reached 8 and 15% in the first and second stages, respectively, without deteriorating the output beam quality. Due to the collinear OPA geometry, nearly transform-limited, temporally and spatially clean pulses

are obtained in both the 1.52- $\mu\text{m}$  signal and the 3.2- $\mu\text{m}$  idler beamlines at average powers of 460 and 180 mW and at pulse durations of 32 and 63 fs, respectively. The center wavelength of the idler pulses is tunable by  $\pm 0.2 \mu\text{m}$  at a spectral full width of  $600 \text{ cm}^{-1}$ .

Figure 1b shows the spectra of the visible beam and the mid-infrared idler pulses up-converted to the blue spectral range obtained from an Au(111) surface in the *ppp* polarization configuration. In Figure 1c, the spectrally resolved intensity cross-correlation signal generated by the broadband MIR and the narrowband VIS pulses is shown. To demonstrate the applicability of our system in SFG spectroscopy, we present vibrational spectra of various organic molecules at different surfaces. The higher repetition rate of the source compared to typically employed laser systems offer great potential for providing the boost in sensitivity required for a broader range of applications including time-resolved experiments and scanning microscopy.

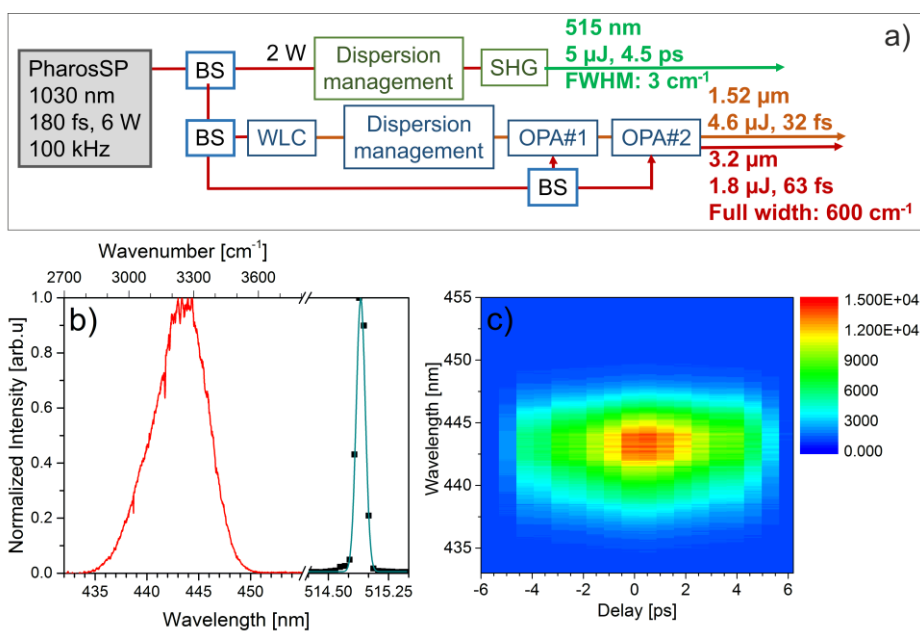


**Figure 1.** (a) BB-SFG source. BS: beam splitter, WLC: white light continuum, SHG: second harmonic generation, OPA#1 and OPA#2: PPLN based collinear amplifiers. (b) Spectrum of the visible pulse (blue) and SFG signal at zero delay (red) as well as (c) the spectrally resolved intensity cross-correlation signal generated on a Au(111) surface. The SFG spectra were collected using a spectrograph with a Peltier-cooled, deep-depletion CCD and a 2400-line/mm grating at an integration time of 1 s.

Financial Support by Leibniz-Gemeinschaft grant no. SAW-2012-MBI-2 to M.M. and DFG (GSC 1013 SALSA) to Z.H. and F.Y. is gratefully acknowledged.

- [1] Wang, H.F.; Velarde, L.; Gan, W.; Fu, L. *Annu. Rev. Phys. Chem.* **2015**, *66*, 189–216.
- [2] Mero, M.; Noack, F.; Bach, F.; Petrov, V.; Vrakking, M. J. *J. Opt. Express* **2015**, *23*, 33157-33163.
- [3] Rotermund, F.; Petrov, V.; Noack, F.; Wittmann, M.; Korn, G. *J. Opt. Soc. Am. B* **1999**, *16*, 1539-1545.

## **Polarization-sensitive stimulated Raman spectroscopy with a compact and versatile laser system**

Hugo Kerdoncuff<sup>1,\*</sup>, Mark R. Pollard<sup>1</sup>, Philip G. Westergaard<sup>1,2</sup>, Jan C. Petersen<sup>1</sup>, Mikael Lassen<sup>1</sup>

<sup>1</sup>*Danish Fundamental Metrology, Matematiktorvet 307, DK-2800 Kgs. Lyngby, Denmark*

<sup>2</sup>*Current address: OFS Fitel Denmark ApS, Priorparken 680, DK-2605 Brøndby, Denmark*

\**hk@dfm.dk*

The demand for novel compact systems for vibrational spectroscopy and microscopy tools is growing with the need for reducing size and cost while increasing reliability and sensitivity. One particular technique, Raman spectroscopy is a label-free and non-destructive method which has been extensively used for detecting and characterizing chemical and biological materials via inelastic Raman scattering of light by molecular vibrations. Large improvements in laser, detector and filter technologies over the past three decades have led to an increased use of Raman spectroscopy. Most applications of Raman spectroscopy are based on spontaneous Raman scattering, which is an inherently weak and incoherent scattering process, often requiring long acquisition times. In order to reach ever shorter acquisition time and higher sensitivity, efforts are now aimed at developing novel methods based on coherent Raman scattering, which generates signals several order of magnitude stronger [1].

In addition to the chemical composition of a sample, Raman spectroscopy may also provide structural information via the polarization variation of the Raman scattered light [2]. Such information is of particular interest in polymer science and structural biology. Unlike other common techniques such as X-ray diffraction or solid-state NMR, polarization-sensitive Raman spectroscopy is also a promising method for the development of compact analytical instruments and remote analysis.

We demonstrate a compact and versatile laser system for polarization-sensitive stimulated Raman spectroscopy (PS-SRS) based on a tunable continuous wave (CW) probe laser combined with a semi-monolithic nanosecond pulsed pump laser at 1064 nm. The laser system is employed in a stimulated Raman gain configuration where the Stokes scattering of an optical pulse from the pump to the probe is detected as an increase of the probe intensity (see experimental setup in Figure 1. (A)). The CW operation of the probe laser offers narrow linewidth, low noise and the advantage that temporal synchronization with the pump is not required. We developed a detection and normalization scheme which enables simultaneous, fast and high-resolution measurement and comparison of Raman spectra from orthogonal polarizations of the Stokes light. The pump and probe lasers have linear polarizations rotated by 45° with respect to each other in order to stimulate scattering in the parallel and orthogonal polarizations relative to the pump beam. The two polarization components are then detected on two photodetectors, filtered and amplified to generate the SRG signals shown in Figure 1. (B). Raman spectra are obtained by integrating the SRG signal while scanning the probe wavelength. The scan

ramp from the probe laser controller (Figure 1. (C)) is used to retrieve the wavelength of the probe laser during the scan and convert the time scale into a wavenumber scale. Simultaneous acquisition and comparison of the Raman spectra in orthogonal polarizations of the Stokes light is rendered possible by normalizing the spectra by the full transfer function of the system (optics and electronics). Lorentzian fits to the Raman bands were used to extract the energy and depolarization ratio of each band. The probe wavelength was tuned from 1520 nm to 1570 nm to observe the carbon-hydrogen (C-H) stretching modes in two polymer samples, polydimethylsiloxane (PDMS) and polymethylmethacrylate (PMMA). We report for the first time (to the best of our knowledge) the depolarization ratios of the C-H stretches in the methyl groups of PDMS and PMMA, in the region  $2825\text{-}3025\text{ cm}^{-1}$  [3].

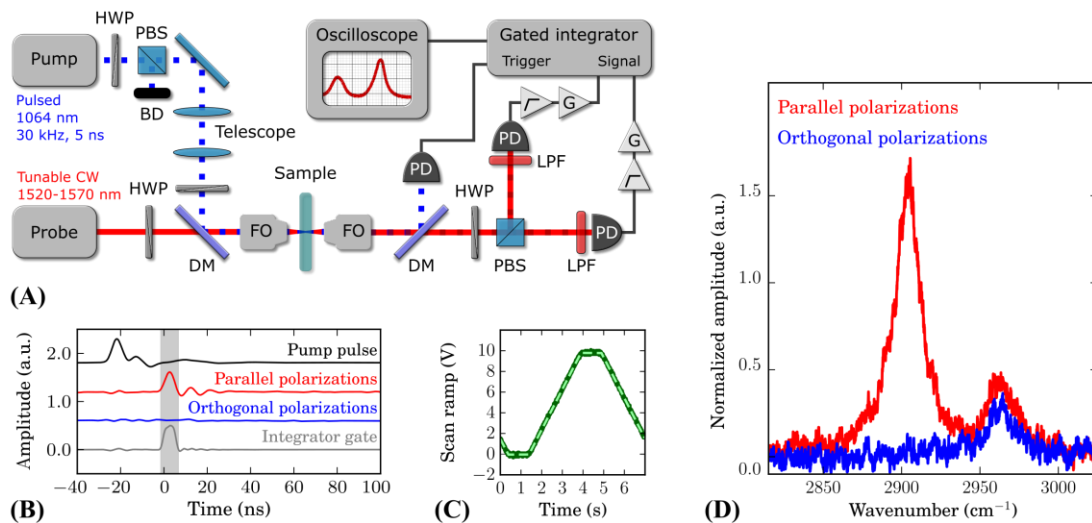


**Figure 1.** (A) PS-SRS setup. BD: Beam dump. PBS: Polarizing beamsplitter. HWP: Half-wave plate. DM: Dichroic mirror. FO: Focusing objective. PD: InGaAS PIN photodetector. LPF: Longpass filter. (B) Time traces showing the detected pump pulse intensity, Raman scattering intensity in the parallel and orthogonal polarization components, and integrator gate, for a PDMS sheet sample probed at 1541 nm ( $2909\text{ cm}^{-1}$ ). (C) Probe laser scan ramp with fit (dashed line) for time-to-wavelength conversion. (D) Raman spectra acquired in 2.5s by PS-SRS, showing the symmetric and antisymmetric C-H stretches of a PDMS sample, for parallel and orthogonal polarizations of the pump and probe beams. The typical peak pump power is 700 W and CW probe power 4 mW. The spectra are normalized to the transfer function of the system for comparison.

- [1] Cheng, J.-X.; Xie, X. S. “Coherent Raman Scattering Microscopy” *CRC Press* **2012**.  
 [2] Tanaka, M.; Young, R. J. *J. Mater. Sci.* **2006**, *41*, 936–991.  
 [3] Kerdoncuff, H.; Pollard, M. R.; Westergaard, P. G.; Petersen, J. C.; Lassen, M. *Opt. Express* **2017**, *25*, 5618–5625.

# Imaging 3D Molecular Orientation by Rotating Polarization Hyperspectral Raman Microscopy

Young Jong Lee\*, Ying Jin, Ian S. Ryu

*Biosystems & Biomaterials Division, National Institute of Standards and Technology,  
Gaithersburg, MD 20899, USA*

\* [youngjong.lee@nist.gov](mailto:youngjong.lee@nist.gov)

A new optical measurement technique is discussed on how to determine three-dimensional (3D) molecular orientation by concurrently analyzing multiple Raman polarization profiles [1]. Conventional approaches to polarization Raman spectroscopy [2] are based on single peaks, and their 2D-projected polarization profiles are limited in providing 3D orientational information. This new method analyzes polarization profiles of multiple Raman modes acquired simultaneously during in a single polarization scanning measurement. This analysis uses only dimensionless quantities (intensity ratios and phase difference between multiple profiles). Therefore, the determined results are not affected by sample concentration and the system response function, which obscure conventional orientation measurement results determined from single 2D-projected polarization profiles. I describe how to determine the 3D molecular orientation with those dimensionless observables for two simplified model cases: (1) a primary mode and an orthogonal secondary mode; and (2) a parallel primary mode and a uniformly distributed secondary mode. In addition, I discuss the effect of orientational broadening on the polarization profiles in the two model cases. In the presence of broadening the mean 3D orientation angles can be determined, as well as the degree of orientational broadening.

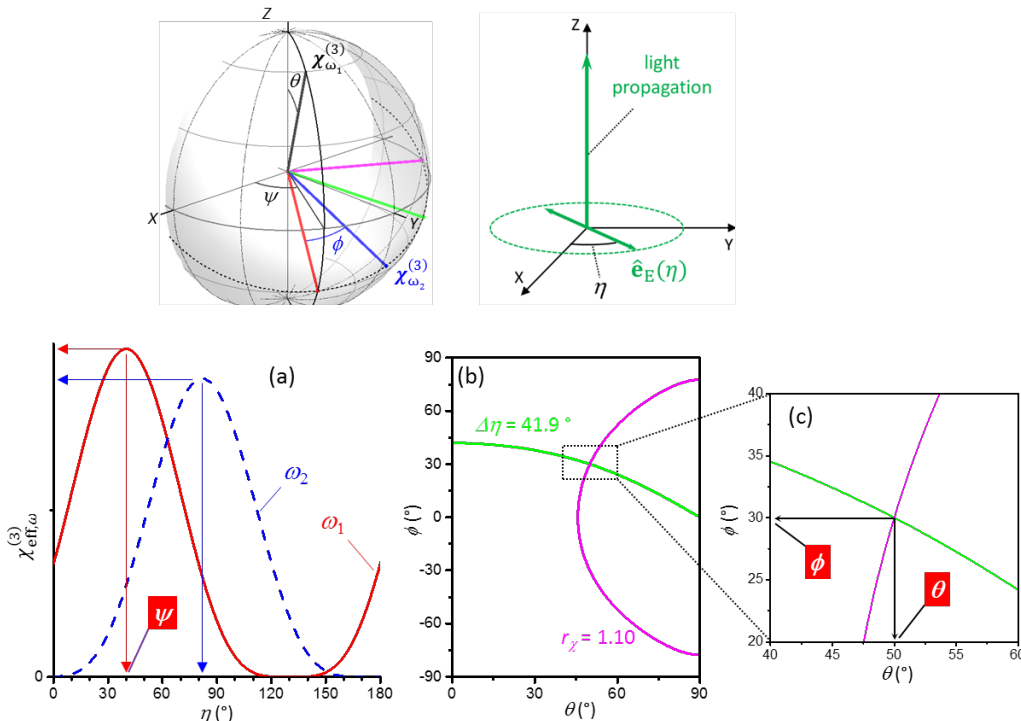


**Figure 1.** Schematic diagram of a nonlinear susceptibility  $\chi^{(3)}$ , is described with Euler angles  $\theta$ ,  $\psi$ , and  $\phi$ . (a) Raman intensity profiles of the primary mode and the secondary mode are  $\chi_{\text{eff},\omega_1}^{(3)}$  and  $\chi_{\text{eff},\omega_2}^{(3)}$ , respectively. The azimuthal angle  $\psi$  is easily determined from  $\eta_{\omega_1}^{\text{max}}$ . The angle difference  $\Delta\eta$  and the maximum intensity ratio  $r_\chi$  values are determined from the two polarization profiles. (b) Contour lines of  $\Delta\eta$  and the maximum intensity ratio  $r_\chi$  are plotted as a function of  $\theta$  and  $\phi$ . (c) Finally, the  $\theta$  and  $\phi$  values are determined from the crossing point of the two contour lines.

As an example, a spherulite of high density polyethylene is imaged by broadband coherent anti-Stokes Raman scattering (BCARS) microscopy while the excitation and collection polarizations are rotating in parallel. Figure 2 shows a part of four dimensional BCARS hyperspectral image data (x–y–frequency–angle). I will discuss how to compute the 3D chain orientation at each image pixel and show the results.

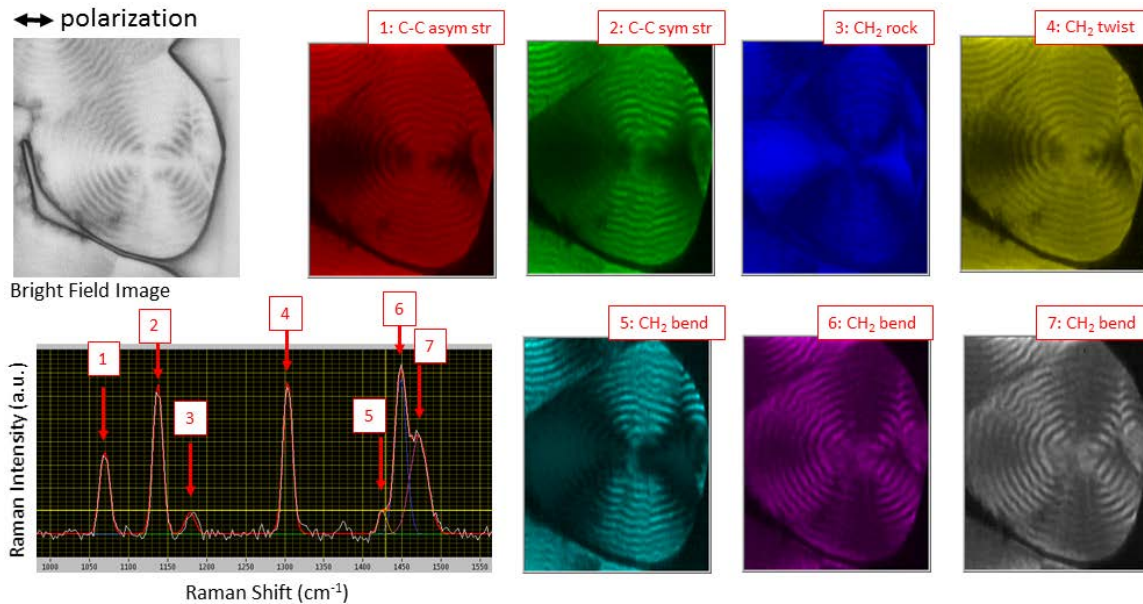


**Figure 2.** A bright field image of spherulite and its CARS images constructed by seven Raman modes in the fingerprint region.

[1] Lee, Y. J. *Opt. Express* **2015**, *23*, 29279–29295.

[2] Lee, Y. J.; Snyder, C. R.; Forster, A. M.; Cicerone, M. T.; Wu, W. *ACS Macro Letters* **2012**, *1*, 1347–1351.

# Structure of water at buried polymer/water interfaces revealed by heterodyne-detected vibrational sum frequency generation spectroscopy

Anton Myalitsin<sup>1</sup>, Satoshi Nihonyanagi<sup>1,2</sup>, Shoichi Yamaguchi<sup>1,3</sup>, Junji Yanagisawa<sup>4</sup>,  
Takashi Aoki<sup>4</sup>, Tahei Tahara<sup>1,2</sup>

<sup>1</sup>*Molecular Spectroscopy Lab, RIKEN. 2-1 Hirosawa, Wako, Saitama 351-0198, JAPAN*

<sup>2</sup>*Ultrafast Spectroscopy Research Team, RIKEN Center for Advanced Photonics (RAP),  
RIKEN. 2-1 Hirosawa, Wako, Saitama 351-0198, JAPAN*

<sup>3</sup>*Department of Applied Chemistry, Graduate School of Science and Engineering,  
Saitama University. 255 Shimo-Okubo, Sakura, Saitama 338-8570 JAPAN*

<sup>4</sup>*Department of Biobased Materials Science, Graduate School of Science and  
Technology, Kyoto Institute of Technology. Hashigami, Matsugasaki, Sakyo,  
Kyoto 606-8585, Japan*

Solid/liquid interfaces are important for many natural and industrial sciences. However, it is difficult to characterize molecular structure at solid/liquid interfaces by conventional spectroscopic methods because it requires interface-selectivity, as well as accessibility to the buried interface. Vibrational sum frequency generation (VSFG) is one of a few spectroscopic methods which fulfill these requirements: It is forbidden in centrosymmetric media under the dipole approximation and hence it is interface-selective. Moreover, it is versatile as long as one side of the interface is transparent for infrared and visible lights. Although conventional VSFG has been utilized for characterization of various liquid interfaces, including solid/liquid interfaces, it is known that conventional VSFG has serious drawbacks, such as spectral deformation and loss of sign. Previously, we have developed multiplex heterodyne-detected VSFG (HD-VSFG) that can directly measure the complex  $\chi^{(2)}$  ( $\chi^{(2)}$ : second-order nonlinear susceptibility) spectrum over a wide frequency range at once with a very high phase stability [1]. The imaginary part of the  $\chi^{(2)}$  ( $\text{Im}\chi^{(2)}$ ) spectrum directly represents the absorptive spectrum at the interface and the sign of  $\text{Im}\chi^{(2)}$  is related to up/down orientation of interfacial molecules. However, it is not easy to determine the phase of the complex  $\chi^{(2)}$  spectrum at the solid/liquid interface. Very recently, we have developed the phase calibration method in which the nonresonant signal of a solid/air interface is used as a phase reference [2].

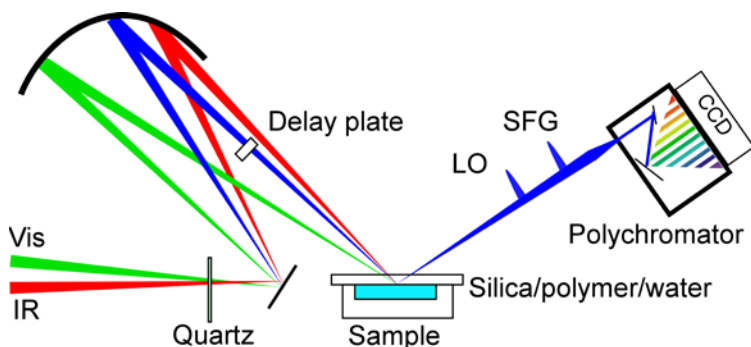


**Figure 1.** Optical layout of the HD-VSFG spectrometer.

In the present study, we applied this new technique to investigate the water structure at polymer/water interfaces, namely, poly(methyl methacrylate) (PMMA) and poly(2-methoxyethyl acrylate) (PMEA) interfaces. These polymers are important for biomedical applications as they are good candidates for coating materials of artificial organs.

Figure 2 shows the  $\text{Im}\chi^{(2)}$  spectra of the PMMA/isotopically diluted water (HOD-D<sub>2</sub>O) interface in the CH and OH stretch frequency regions [3]. In the CH stretch region, a very strong positive band is observed and is assignable to the symmetric stretch of OCH<sub>3</sub> group in the PMMA side chain. This indicates that the OCH<sub>3</sub> group is pointing down toward the water phase. The  $\text{Im}\chi^{(2)}$  spectrum in the OH stretch region shows two positive OH bands, peaked around 3400 cm<sup>-1</sup> and 3550 cm<sup>-1</sup>. This indicates that there are two distinct water species that are pointing toward the polymer phase with a different degree of interaction with the polymer. One of the water species can be attributed to the water forming hydrogen bonds with the hydrophilic carbonyl group and the other to the water weakly interacting with hydrophobic OCH<sub>3</sub> group. Such a simple, but precise modelling of the polymer/water interface was not achieved by former conventional VSFG studies, demonstrating the powerfulness of HD-VSFG.

The water structure at the PMMA/water interface is compared with that of the PMEA interface and the structure-function relationship will be discussed.

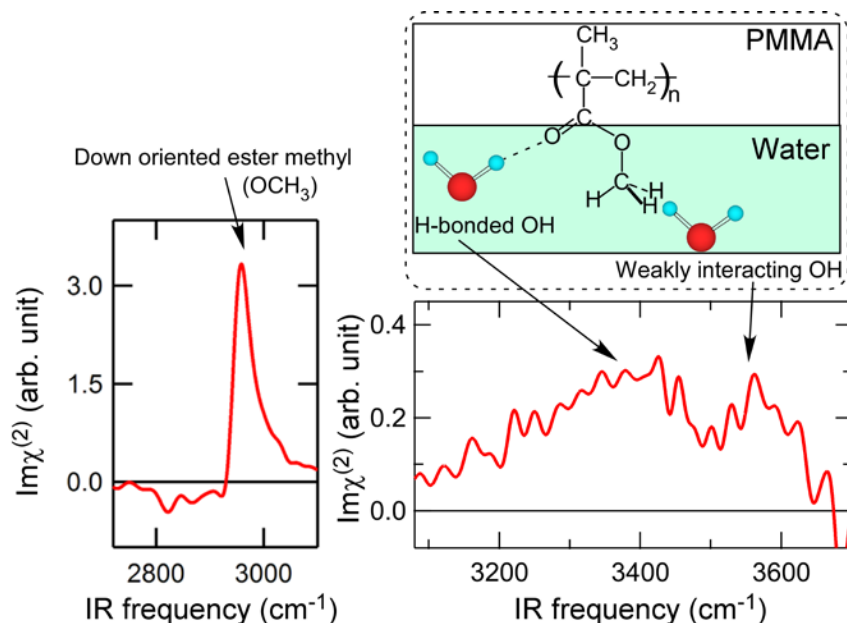


**Figure 2.**  $\text{Im}\chi^{(2)}$  spectra of the PMMA/HOD-D<sub>2</sub>O interface in the CH and OH stretch frequency regions. The structure of the PMMA/water interface is depicted.

[1] Nihonyanagi, S.; Yamaguchi, S.; Tahara, T. *J. Chem. Phys.* **2009**, 130, 204704.

[2] Myalitsin, A.; Urashima, S.; Nihonyanagi, S.; Yamaguchi, S.; Tahara, T. *J. Phys. Chem. C* **2016**, 120, 9357.

[3] Myalitsin, A.; Nihonyanagi, S.; Yamaguchi, Yanagisawa, J.; Aoki, T.; S.; Tahara, T. *to be submitted*.

## Study of Azo-Phenyl-Carbazole Dyes on Au Surface by Non-Collinear Phase-Sensitive Sum Frequency Generation Spectroscopy

Regimantas Januškevičius<sup>1\*</sup>, Darius Urbonas<sup>2</sup>, Armandas Balčytis<sup>2,3</sup>, Gintautas Bagdžiūnas<sup>4</sup>, Martynas Gabalis<sup>2</sup>, Vitalij Kod<sup>1</sup>, Robertas Kananavičius<sup>1</sup>, Rolandas Tomašiūnas<sup>5</sup>, Vytautas Getautis<sup>4</sup>, Raimondas Petruškevičius<sup>2</sup>

<sup>1\*</sup> *EKSPLA Ltd., Savanorių pr. 237, LT-02300 Vilnius, Lithuania*

<sup>2</sup> *Center for Physical Sciences and Technology, Savanorių pr. 231, LT-02300 Vilnius, Lithuania*

<sup>3</sup> *Swinburne University of Technology, Hawthorn, Victoria, 3122 Australia*

<sup>4</sup> *University of Technology, Radvilenų hwy. 19, LT-50270 Kaunas, Lithuania*

<sup>5</sup> *Institute of Applied Research, Vilnius University, Sauletekio pr. 10, LT-10223 Vilnius, Lithuania*

\* [r.januskevicius@ekspla.com](mailto:r.januskevicius@ekspla.com)

We report an investigation of dipole moment orientation of azo-phenyl-carbazole (V-728 AZO) dyes using ps-scanning non-collinear Phase-Sensitive Sum Frequency Generation (PS-SFG) spectrometer which was developed exploiting the nonlinear second order surface susceptibility of Au substrate [1]. For this kind of samples as AZO dyes high spectral resolution is required- about  $4\text{ cm}^{-1}$ . We describe also another kind of laser source for SFG spectroscopy- OPCPA (Optical Parametrical Chirped Pulse Amplifier) [2]. Au substrate local oscillator was used as a sum frequency source for PS-SFG measurements. The system was tested using self-assembled monolayer of V-728 AZO dyes on Au substrate and the orientation of the dye dipoles with respect to the surface of the substrate was shown.

Measured and theoretically fitted interferograms [3] for V-728 AZO dyes are presented on Figure 1. Retrieved imaginary part indicates that the molecule orientation is dependent on the molecule state (Trans or Cis). Introduction of UV exposure allowed control of the orientation of the molecules and allows to decrease disorder in the system. We have shown that our ps-scanning PS-SFG system has resolution  $2\text{ cm}^{-1}$  using Au local oscillator and Au reference. System proved to be capable to differentiate dipole orientations of attached molecules and useful for broadband ( $1000\text{-}4200\text{ cm}^{-1}$ ) vibrational measurements.

Typical resolution obtained with fs-broadband SFG is  $\sim 10\text{-}20\text{ cm}^{-1}$ , which limits ability to analyze vibrational line-shapes [4]. Finally a hybrid system was demonstrated where two separate laser sources – femtosecond and picosecond – were synchronized to achieve both very high spectral resolution ( $<1\text{ cm}^{-1}$ ) and simultaneous spectral recording [4]. However the system required two complex independent synchronised laser systems which would be difficult to implement in most laboratories.

We also presented initial results on developed novel OPCPA based laser source which provided both narrowband  $\sim 11.2\text{ ps}$  duration VIS channel (532 nm) and broadband

(>700 $\text{cm}^{-1}$ ) femtosecond mid-IR channel. The OPCPA system was described recently [2] Resolution of ps-scanning and fs-broadband spectrometer was similar. This demonstrates the possibility of the OPCPA based broadband-SFG for investigation samples like V-728 AZO dyes with high resolution in future.

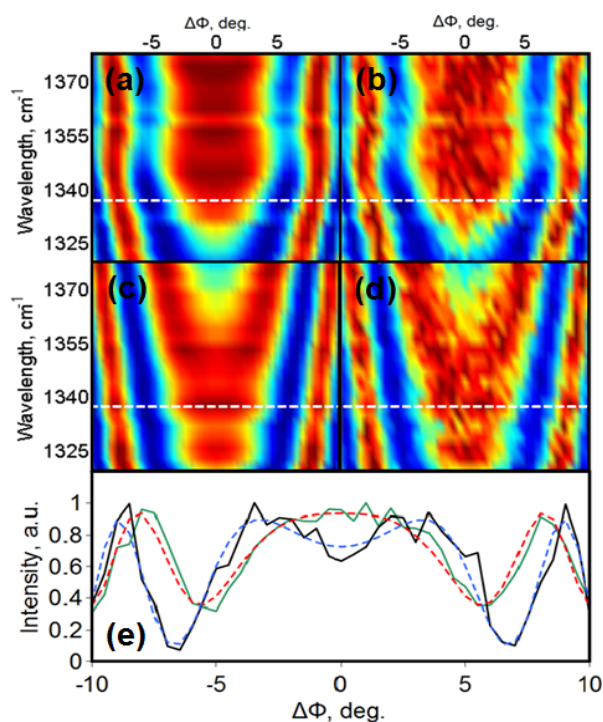


**Figure 1.** Interferograms of V-728 AZO dyes are presented (*a, c* – theoretical data, *b, d* – measured data). White dashed line denotes the *e* figure. In figure *e* red dashed line depicts the fitted reference theoretical data, and blue dashed line – fitted AZO theoretical data. Green and black lines denote reference and AZO measurements.

[1] [www.ekspla.com/product/narrow-linewidth-picosecond-opg-pgx11](http://www.ekspla.com/product/narrow-linewidth-picosecond-opg-pgx11).

[2] R. Danilevičius, A. Zaukevičius, R. Budriūnas, A. Michailovas, and N. Rusteika, "Femtosecond wavelength-tunable OPCPA system based on picosecond fiber laser seed and picosecond DPSS laser pump," *Opt. Express* **24**, 17532 (2016).

[3] P.A. Covert, W.R. FitzGerald, D.K. Hore, "Simultaneous measurement of magnitude and phase in interferometric sum-frequency vibrational spectroscopy", *J. Chem. Phys.* **137**, 014201 (2012).

[4] L. Velarde *et al.*, "Communication: Spectroscopic phase and lineshapes in high-resolution broadband sum frequency vibrational spectroscopy: Resolving interfacial inhomogeneities of "identical" molecular groups", *J. Chem. Phys.* **135**, 241102 (2011).

## Interplay Between Surface Concentration and Surface Orientation of Complex Adhesives through Linear and Nonlinear Vibrational Spectroscopy

Sandra Roy<sup>1</sup>, Stephan Freiberg<sup>2</sup>, Claude Leblanc<sup>2</sup>, Dennis K. Hore<sup>1,\*</sup>

<sup>1</sup>Department of Chemistry, University of Victoria, Victoria BC, Canada, V8W 3V6

<sup>2</sup>Mapei Inc., 2900 Avenue Francis-Hughes, Laval Qc, Canada, H7L 3J5

\*dkhore@uvic.ca

Adhesion is an important process to understand as it has a wide variety of applications. The adhesion of two surfaces is governed by their interactions at the molecular level. It is reasonable to believe that stronger interactions would lead to greater ordering at the interface. This is where sum frequency generation is useful as its intensity is strongly dependent on the orientation of functional groups present at the interface, as well as their concentration at the surface.

Vibrational sum frequency generation is a powerful technique to study interfaces. The extreme surface specificity of SFG is due to signal arising only when there is a break in symmetry. This is important when studying solid-liquid interfaces or thick films where the bulk to surface ratio is relatively large.

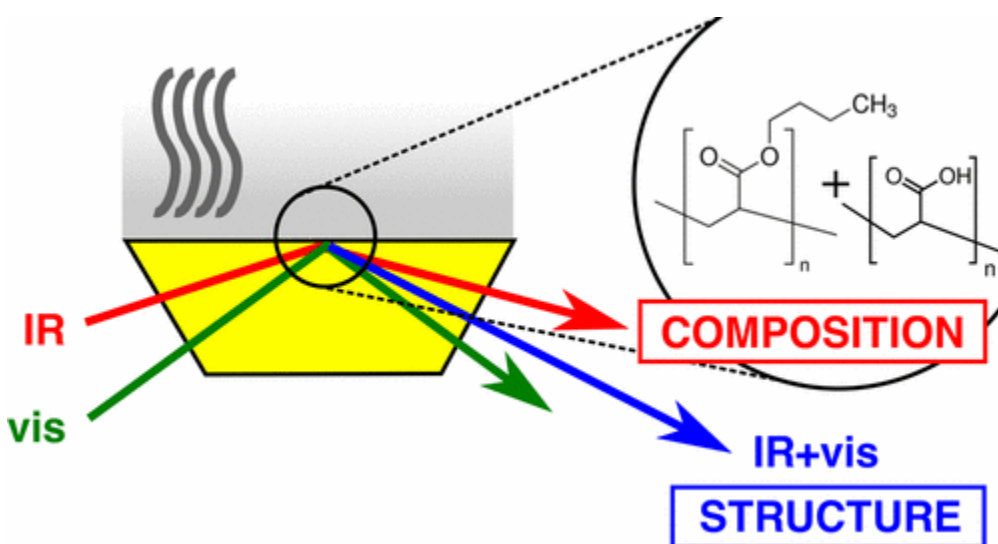


**Figure 1.** Graphical abstract [1] showing the analysis of the structure of pressure sensitive adhesives by SFG (blue) and analysis of its composition by IR (red).

It can sometimes prove difficult to separate the relative contribution of surface concentration and surface structure to the SFG intensity. For relatively large and complex molecules, such as polymers, it is reasonable to assume that the composition near the surface (within a few microns) is not significantly different than directly at the surface

(within tens of nanometers). This allow us to use TIR-IR as a probe of the surface composition.

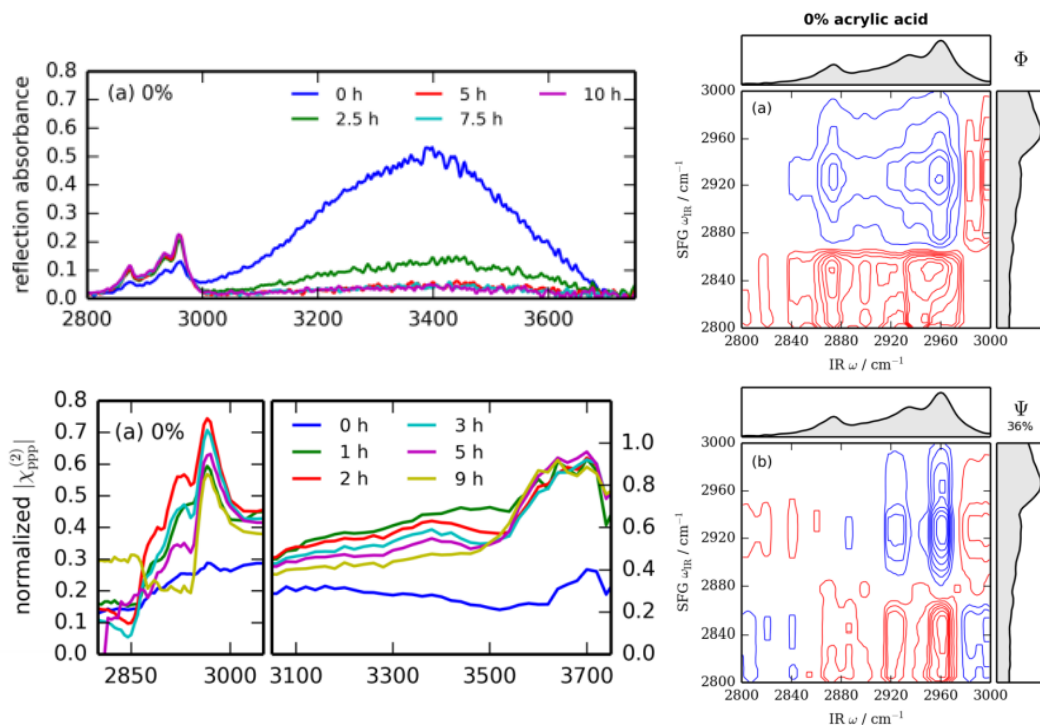


**Figure 2.** IR spectra (top left) and SFG spectra (bottom left) of PSA without acrylic acid collected throughout the drying process. Maps on the right correspond to the heterospectral (SFG-IR) 2D correlation analysis.

In this study, we used SFG and TIR-IR to study the drying process of a pressure sensitive adhesive (PSA) aqueous latex solution mainly composed of butyl acrylate with varying concentrations of acrylic acid. Heterospectral 2D correlation analysis revealed interesting features for different concentrations of acrylic acid. In the absence of acrylic acid, results led us to conclude that reordering near the interface is governed by the increase in packing during water evaporation. This reordering is relatively slow. On the other hand, the PSAs with acrylic acid present reorder faster and this reordering is driven by strong hydrogen bonding to the surface.

[1] Roy, S.; Freiberg, S.; Leblanc, C.; Hore, D.K. *Langmuir* **2017**, 33, 1763–1768.

# High-Resolution Coherent Anti-Stokes Raman Spectroscopy (CARS) of Tritiated Hydrogen Molecules

M. Schlösser<sup>1\*</sup>, X. Zhao<sup>1</sup>, M.T. Trivikram<sup>2</sup>, E. J. Salumbides<sup>2</sup>, W. Ubachs<sup>2</sup>

<sup>1</sup>*Tritium Laboratory Karlsruhe, Institute for Technical Physics, Karlsruhe Institute of Technology, P. O. Box 3640, 76021 Karlsruhe, Germany*

<sup>2</sup>*Department of Physics and Astronomy, LaserLaB, VU University, De Boelelaan 1081, NL-1081 HV Amsterdam, the Netherlands*

\**magnus.schloesser@kit.edu*

The hydrogen molecule has been the benchmark system of molecular spectroscopy throughout decades. In particular, since the system has become amenable for very precise full-fledged quantum-electrodynamical (QED) calculations (by Pachucki and coworkers) [1] measurements on the level structure of the hydrogen molecule have become a test ground for molecular QED. Since effects of the strong, weak and gravitational force do not play a role in the level structure of hydrogen a test of QED is in fact also a test of the Standard Model in a molecular system. Such tests can be interpreted in terms of possible fifth forces acting in molecules [2] or in terms of bounds on extra dimensions [3].

In the last decade the spectroscopy on H<sub>2</sub>, HD, D<sub>2</sub> and HD<sup>+</sup> ions has been strongly advanced by the laser spectroscopy group at the Vrije Universiteit Amsterdam [4] while constantly pushing the accuracy to a level, which is now challenging the theoretical prediction. Until now this ultra-high-resolution spectroscopy has only been applied on aforementioned non-radioactive isotopologues.

We therefore now want to expand the field of investigation and double the amount of species under investigation by adding the tritium containing molecules T<sub>2</sub>, DT and HT. That allows testing the quantum chemical theory in a much wider mass range (m(H):m(D):m(T) = 1:2:3), allowing access to evaluate mass-dependent Born-Oppenheimer corrections.

The use of radioactive tritium restricts the spectroscopy performed due to legal and technical limitations. Therefore, a pure optical technique is chosen to perform first high resolution experiments on the ro-vibrational splitting of the electronic ground state of the tritiated hydrogen isotopologues, T<sub>2</sub>, DT and HT.

Previous measurements of these levels were performed by linear Raman spectroscopy by Veirs and Rosenblatt in 1987 [5] with an accuracy of about 0.1 cm<sup>-1</sup>, which is mainly limited by the resolution and accuracy of the spectrometer used.

We are therefore setting up a Coherent Anti-stokes Raman Spectroscopy (CARS) experiment, in which the achievable spectral resolution is related to the accurate wavelength determination of the narrow linewidth of pump and probe lasers and not to the finite size of a spectrometer slit, grating and detector.

The projection for the measurement uncertainty shows that using the CARS technique we will be 100 times more accurate as compared to the latest data obtained by linear Raman spectroscopy in 1987.

In this poster we will present the prospects of the high-resolution study on tritiated hydrogen molecules. We put the measurements in the context of the current high-resolution measurement of tritiated and non-tritiated hydrogen isotopologues. Further, we

will present the CARS setup (See Fig. 1). The optical system comprises two narrow band pulsed lasers from the LaserLab Amsterdam. The pump laser pulse (532 nm) is delivered by an injection seeded and Q-switched Nd:YAG laser, which is overlapped with a probe laser pulse ( $\sim 612$  nm for the Q-branch of  $T_2$ ) of a narrowband, tunable traveling-wave pulsed dye amplifier. The wavelengths of pump and probe beam are measured highly accurate by wavemeter and a molecular iodine standard, respectively. A photo multiplier is employed to detect the Anti-Stokes light pulse. The optical cell and the tritium gas ( $T_2$ , DT or HT) are produced at the Tritium Laboratory Karlsruhe, the largest tritium handling laboratory in Europe, according to the safety requirements and based on experience of previous Raman measurements of tritiated gases [6]. Finally, we present the current status of the measurements and discuss the experimental sources of uncertainty.

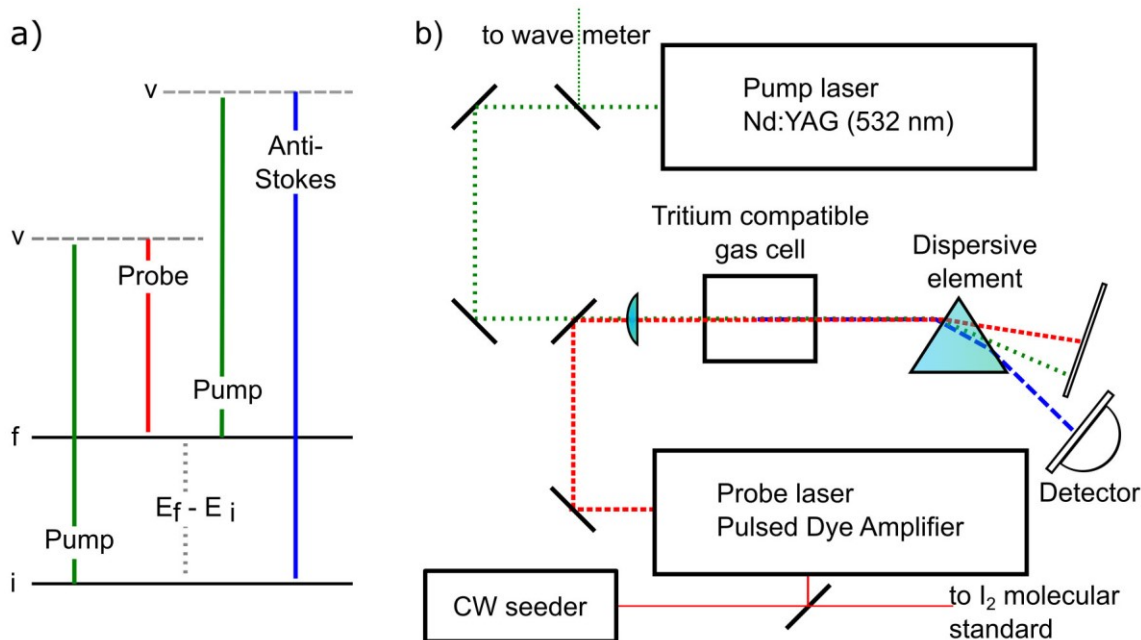


**Figure 1.** a) Principle of CARS spectroscopy. When blue-shifted Anti-Stokes light is detected, then the measured quantity - the energy for the excitation of molecular transition - is given by the difference of the high accurately known pump and probe photon energies. b) Sketch of the experimental setup of the high-resolution CARS experiment.

[1] Pachucki, K.; Komasa, J. *J. Chem. Phys.* **2014**, *141*, 224103

[2] Salumbides, E. J., Koelemeij, J. C. J.; Komasa, J.; Pachucki, K.; Eikema, K. S. E.; Ubachs W. *Phys. Rev. D* **2013**, *87*, 112008

[3] Salumbides, E. J.; Schellekens A. N.; Gato-Rivera B.; Ubachs W. *New. J. Phys.* **2015**, *17*, 033015

[4] Ubachs, W.; Koelemeij, J.C.J.; Eikema, K.S.E.; Salumbides E.J.; *J. Mol. Spectr.* **2016**, *216*, 1

[5] Veirs, D. K.; Rosenblatt, G. M.; *J. Mol. Spectr.* **1987**, *121*, 401

[6] Schlösser, M.; Fischer, S.; Sturm, M.; Bornschein, B.; Lewis, R.J.; Telle, H.H. *Fusion Sci. Technol.* **2011**, *60*, 976-981

# Nonlinear Vibrational Spectroscopy of the Oil-Metal Interface

Wei Chen (Sean) Yang<sup>1</sup>, Bryce McGarvey<sup>2</sup>, Dennis K. Hore<sup>1\*</sup>

<sup>1</sup>*Department of Chemistry, University of Victoria, Victoria BC, Canada, V8W 3V6  
dkhore@uvic.ca*

<sup>2</sup>*Imperial Oil, Sarnia Technology Applications & Research, Sarnia, ON*

Corrosion under acidic conditions has been a persistent problem in the petroleum refining industry. This complication has a tremendous impact on profit as well as the environment [1]. In order to address and minimize the corrosion problems in refinery infrastructure, the molecular structure of the adsorbed species must be well understood at the interface. Corrosion inhibitor injection has been widely recognized as the most cost-effective method for prevention and treatment [2]. However, selecting a suitable surfactant as inhibitor is yet another difficult task in and of itself. In recent years, alkyl phosphate ester has emerged to as a promising choice for the steel-oil interface. However, the interfacial competitive adsorption at the interface between the oil and the surfactant on steel has been insufficiently studied and is not well understood.

Visible-IR sum frequency generation spectroscopy (SFG) is a nonlinear vibrational technique that is suitable for probing interfacial species due to its nature of surface specificity. SFG spectra provide valuable information on molecular orientation and structure of the adsorbed species.

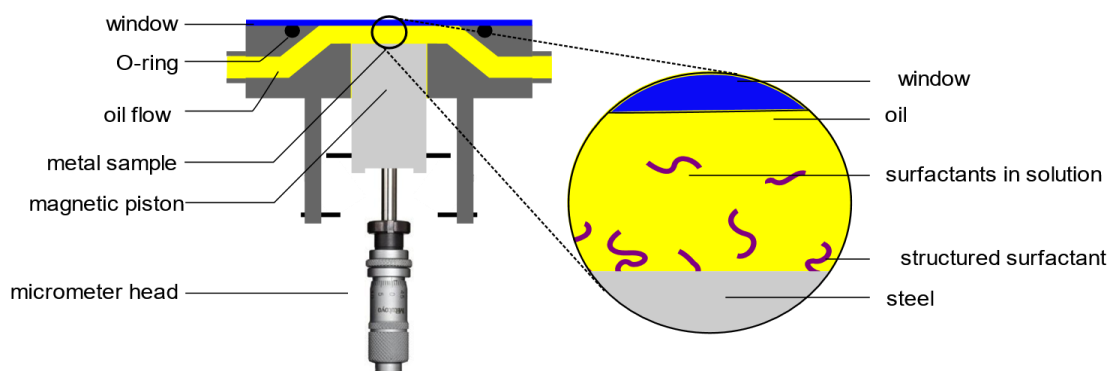


**Figure 1.** Experimental configuration of the sample flow cell

In this work, the study of oil on steel utilizing SFG spectroscopy is carried out. Ultra-smooth A516 carbon steel samples and 99% reagent grade *n*-heptane are used for the experiment. Dibutyl phosphate ester and a commercial corrosion inhibitor are examined under the heptane-steel system. Spectra obtained from heptane on high polished steel at the exposed interface is also examined and compared with a spectra obtained from heptane on silica at the exposed interface.

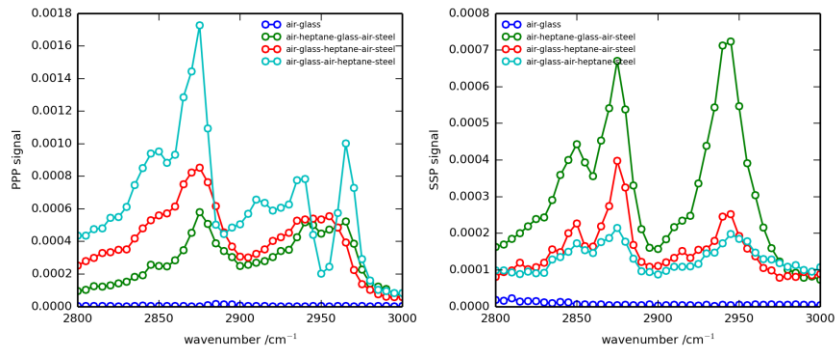


**Figure 2.** Comparison of SFG signals from all heptane-glass, glass-heptane, heptane-steel interface in both PPP (SFG, visible, IR) and SSP polarization experiments.

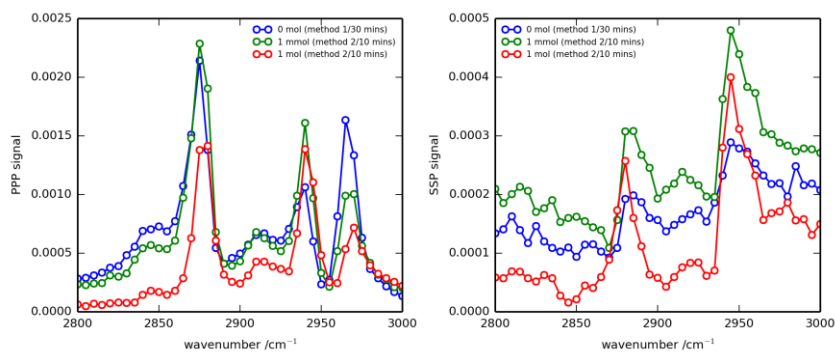


**Figure 3.** SFG spectra of dibutyl phosphate ester in heptane adsorbed on steel at 2 concentrations. Experimental spectra were taken at the exposed surface when the sample was dried. Method 1 refers to a sample preparation which the steel sample was immersed into solution for 30 minutes then dried under  $N_2$ . Method 2 refers to a sample preparation in which the surface of steel was covered with solution for 10 minutes then dried under  $N_2$ .

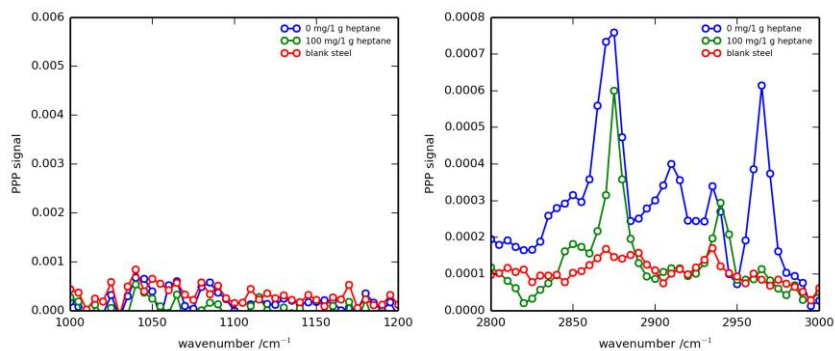


**Figure 4.** SFG spectra of the commercial inhibitor in heptane adsorbed on steel.

[1] Coletti, F.; Hewitt, G. *Crude Oil Fouling Deposit Characterization, Measurements, and Modeling*; Elsevier, 2015.

[2] Malik, M. A.; Hashim, M. A.; Nabi, F.; AL-Thabaiti, S. A.; Khan, Z. *Int. J. Electrochem.* **2011**, 6, 1927–1948.

# Linear Programming to Determine Molecular Orientation at Surfaces through Vibrational Spectroscopy

Fei Chen<sup>1</sup>, Kuo Kai Hung<sup>1</sup>, Ulrike Stege<sup>1,\*</sup>, Dennis Hore<sup>2,\*</sup>,

<sup>1</sup>*Department of Computer Science, University of Victoria,  
Victoria BC, Canada, V8W 3V6 , \*ustege@uvic.com*

<sup>2</sup>*Department of Chemistry, University of Victoria,  
Victoria BC, Canada, V8W 3V6 , \*dkhore@vuic.com*

Applying linear programming to spectroscopy techniques, such as IR, Raman and nonlinear vibrational (SFG) spectroscopy, is a new approach to extract the molecular orientation information at surfaces. Previous research has shown that linear programming approach increased the computation from  $O(n!)$  to  $O(n)$ . However, when the spectral information is used to build the instance of the linear programming model, the linear programming solver does not always returns the target molecular orientation distribution information. Therefore, we need to study the nature of our linear programming model, and find out the cause for the failure of some instances. Following that, we aim to study whether the linear programming be applicable for different test cases. what's more, for each test case, what spectral information is needed to build the linear programming instances in order to obtain the target candidate composition. With the help of a simplified molecular model, we learned that from the spectral information, the inability to extract a sufficient data set to build the linear programming instances is the cause for the failed cases. To further explore, we study some realistic molecular models at surfaces. We learn that even combining all three spectral information of IR, Raman and SFG to build the linear programming instances, it is not sufficient to obtain the target composition for most test cases when the candidates coming from same molecular model. However, when studying different types of realistic molecular models at surfaces, Raman or SFG spectral information alone is sufficient to obtain the target composition when candidates of each molecular model expanded in  $[0, 90)$  on  $\theta$ . When candidates of each molecular model expanded in  $[0, 180]$  on  $\theta$ , excluding 90, SFG spectral information needs to be combined with IR or Raman to obtain the target composition. When a slack variable is introduced to each spectral technique, the case of different types of realistic molecular models at surfaces is considered. When each molecular model's candidates expanded in  $[0, 90)$  on  $\theta$ , Raman spectral information alone is sufficient to obtain the target composition. When each molecular model's candidates expanded in  $[0, 180]$  on  $\theta$ , excluding 90, the return compositions, of the linear programming instances using only Raman spectral information and using Raman and SFG spectral information, are both needed to obtain the target composition.

**A**

$$\underset{p_c}{\text{minimize}} \sum_{n=1}^{N_p} \left| \text{Target} - \sum_{c=1}^{N_c} p_c f_{\theta}(x) \right|$$

$$\sum_{c=1}^{N_c} p_c = 1$$

**B**

$$X = \left| \text{Target} - \sum_{c=1}^{N_c} p_c f_{\theta}(x) \right|$$

$$X \geq \text{Target} - \sum_{c=1}^{N_c} p_c f_{\theta}(x)$$

$$X \geq -\text{Target} + \sum_{c=1}^{N_c} p_c f_{\theta}(x)$$

**C**

$$\underset{p_c}{\text{minimize}} \sum_{n=1}^{N_p} X_p$$

$$X_1 - \text{Target}_1 + \sum_{c=1}^{N_c} p_c f_{\theta}(x_1) \geq 0$$

$$X_1 + \text{Target}_1 - \sum_{c=1}^{N_c} p_c f_{\theta}(x_1) \geq 0$$

$$\vdots$$

$$X_n - \text{Target}_n + \sum_{c=1}^{N_c} p_c f_{\theta}(x_n) \geq 0$$

$$X_n + \text{Target}_n - \sum_{c=1}^{N_c} p_c f_{\theta}(x_n) \geq 0$$

$$\sum_{c=1}^{N_c} p_c = 1$$

**Figure 1.** (A) initial linear programming model, (B) convert condition, (C) final linear programming model.

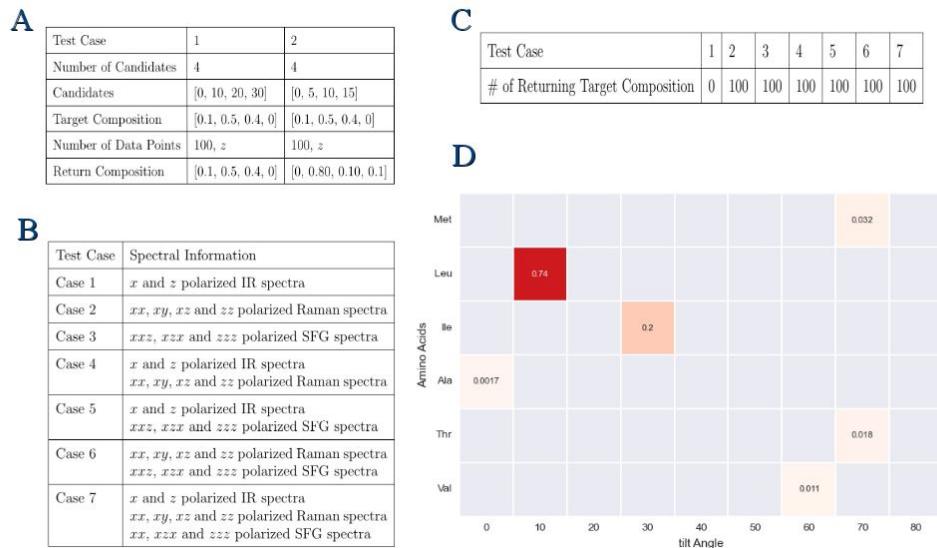


**Figure 2.** Experimental configuration illustrating (A) Test cases of simplified molecular model, (B) Test cases of realistic molecular model, (C) Result of test cases of one type of realistic molecular model, (D) Result of one test case of multiple types of realistic molecular model.

[1] Kuo Kai. Hung, U. Stege, D. Hore. "IR absorption, Raman scattering, and IR-vis sum-frequency generation spectroscopy as quantitative probes of surface structure". *Appl. Spec-trosc. Rev.* **2015**, 50, 351.

[2] Kuo Kai. Hung. "Extracting Surface Structural Information from Vibrational Spectra with Linear Programming". *MSC thesis*, University of Victoria. **2015**

[3] S. Hall, K. Jena, P. Covert, S. Roy, T. Trudeau, D. Hore. "Molecular level surface structure from nonlinear vibrational spectroscopy combined with simulations" *J. Phys. Chem.* **2014**, B 118, 5617

9th International Conference on  
Advanced Vibrational Spectroscopy

# THANKS TO OUR SPONSORS

## Platinum



## Gold



## Silver



Agilent Technologies



DELTA PHOTONICS  
LIGHTYEARS AHEAD



Centre for  
Advanced Materials  
& Related Technology



## Logo

